Copyright

by

Vikas Reddy Voggu

2017

**The Dissertation Committee for Vikas Reddy Voggu Certifies that this is the approved version of the following dissertation:**

# Development of Solution Processed, Flexible, $CuInSe_2$ Nanocrystal Solar Cells

**Committee:**

Brian A. Korgel, Supervisor

John G. Ekerdt

Delia Milliron

Thomas Truskett

David A. Vanden Bout

# Development of Solution Processed, Flexible, $CuInSe_2$ Nanocrystal Solar Cells

**by**

**Vikas Reddy Voggu**

**Dissertation**

Presented to the Faculty of the Graduate School of

The University of Texas at Austin

in Partial Fulfillment

of the Requirements

for the Degree of

**Doctor of Philosophy**

**The University of Texas at Austin**

**December 2017**

# Dedication

For my loving parents, Prabhakar Reddy Voggu and Mallika Voggu. For all those who are working towards the development of clean energy technologies.

# Acknowledgements

Graduate study at UT Austin has been a time where I learnt the most in my life. I have grown as a scientist, leader, and effective communicator while pursuing my PhD. I am thankful for all the mentors and peers who helped me to gain this knowledge and become a better person.

First of all, I would like to thank my adviser Dr. Brian Korgel, who always kept his trust in me while guiding me with tough projects. Right from the moment he called me the "(photovoltaic) device guru," I have been inspired, and in times when the experiments do not go as planned, it is his belief in me and motivation that I received from him that kept me going. Apart from learning how to approach scientific problems, I have also developed collaboration and mentorship skills from him. The wisdom that he passed on to me is something that will help me for the rest of my life. He is truly an inspiration and the guru of my life. Further, I would like to thank my committee members Dr. Delia Milliron, Dr. John Ekerdt, Dr. David Vandenbout, and Dr. Tom Truskett for their support.

I would like to thank all members of Dr. Korgel's lab: I have learnt something from each one of them. Dr. Taylor Harvey, Dr. Jackson Stolle, and Dr. Christian Bosoy mentored me when I joined the group. I cannot recollect a single time when they were unwilling to help me or when they did not have advice for my research problems. They taught me many lab techniques and skills which cannot be acquired from reading literature. I still take advice from Taylor and Jackson, and they continued to be my mentors even after their

graduation. My sincere thanks to the other senior graduate students Dr. Doug Pernik, Dr. Yixuan Yu, Dr. Xiaotang Lu, Dr. Vahid Akhavan, Dr. Julian Villarreal, Dr. Timothy Bogart and Dr. Aaron Chockla who have given me their guidance in their respective areas of expertise. Dorothy Silbaugh, Emily Adkins, Adrien Guillaussier, Cherrelle Thomas, and I started graduate school in the same year. We have supported each other through the hardships in graduate school. Younger generations of graduate students in my lab, Taizhi Jiang (TJ), Dan Houck, Tim Siegler, Hyun Gyung Kim, Tushti Shah, Yangning Zhang and Michael Abney have been great colleagues. The last few days I have worked with our newest Korgelite, Wen Liu, who has picked up my device making skills rapidly. I am sure she will achieve great advancements in the field of photovoltaics

Friends are an essential part of graduate life and I thank Dorothy for all the interesting talks and going to lunch with me every day, TJ for all the activities we have done together including badminton, swimming, grocery shopping, etc., Emily for her opinions on presentations, dragging me to all the UT events with her, and going to haunted house with me (the biggest mistake of her life), Tushti for her advice on life, Adrien and Cherrelle for making me laugh everyday with their sense of humor, and Bobi and Leslie for working alongside me and making research more fun. Those lunch break chit chats, sport activities, and social events have made my life here more enjoyable at graduate school.

My research wouldn't have been successful without help from all the undergraduate researchers and visiting scholars who worked with me. Thanks to Bobi Simonsen, Leslie Fillip, Drew Heilman, Travis Dinh, Kyle Dalal, Adi Shetkar, Saatviki Gupta, Omar Ali,

Cao Meng, Kanta Yamaguchi, and Sam Morehead. I am grateful to all my collaborators for the useful partnerships in projects, without them it would have been impossible to finish some of them. Thanks to my collaborators Dr. James Sham, Dr. Malcolm Brown, Sarah Pfeffer, and Jennifer Pate for working with me to fabricate the highest efficiency paper solar cells. Thanks to collaborators Dr. Nanshu Lu, Siyi Liu, and Stephan Dottermusch for other projects relating to solar cells. I would like to specially thank Detlef Smilgies and Vanessa Pool for helping with in-Situ XRD measurements at CHESS and SLAC, respectively. Thanks to all the equipment managers who provided me with excellent training to use various characterization equipment. I would like to thank Raluca Gearba, Damon Smith, Mark Andrews, and Kristofer Ohlinger for their help while working with equipment in the clean room, Hugo Celio for his help with TGA and FTIR, Dwight Romanovicz for his help with TEM and SEM, and Vincent Lynch for help with XRD. I am grateful to our administrative assistant, Jon Peck and graduate coordinator, Kate Baird for dealing with the administrative tasks. Their knowledge and prompt responses saved me a lot of time.

I would like to thank all my friends and family for their support. Even though I didn't have my family here in Austin, my friends Pranav, Vatsal, Deepak, Lakshmi and Abhinav always made me feel included. I would like to thank Pooja for all the love, affection and support. She has always been there for me. Most importantly, I want to thank my parents, Prabhakar and Mallika who have sacrificed a lot for me to succeed in life. They taught me the value of education and worked hard to provide me the same. I thank them

for believing in me, motivating me, and for always being there for me. They are the reason for providing me the opportunity to earn my Ph.D.

# Development of Solution Processed, Flexible, $CuInSe_2$ Nanocrystal Solar Cells

Vikas Reddy Voggu, Ph.D.

The University of Texas at Austin, 2017

Supervisor: Brian A. Korgel

Clean sources of energy, especially photovoltaics (PVs), are urgently needed to cope with global energy shortage and environmental pollution. For PVs to play a significant role in energy production, the current prices must be brought down. Thin film PVs made using layered Mo or Au/$CuInGaSe_2$(CIGS)/CdS/ZnO/ITO have already shown high efficiencies. Traditionally, most layers in CIGS solar cells are deposited using high-cost techniques requiring high temperatures and ultra-low pressures. By replacing the traditionally processed CIGS with a nanocrystal layer that can be deposited at mild processing conditions, the fabrication cost can be reduced. In this study, a high yielding synthesis method for $CuInSe_2$ nanocrystals has been developed which gives the best efficiency (3.1%), so far, for low-temperature processed $CuInSe_2$ nanocrystal PVs.

An important challenge that nanocrystal solar cells currently face is low device efficiency, resulting in higher operating cost. $CuInSe_2$ nanocrystals can remain suspended in solution because of the long chain organic ligands attached to the surface. However, these ligands hinder charge transfer between nanocrystals causing low device efficiency. These ligands have been successfully replaced with smaller sulfide ions thereby improving

the best efficiency of low-temperature processed $CuInSe_2$ nanocrystal solar cells from 3.1 % to 3.5%.

Another approach to reducing the cost of $CuInSe_2$ PVs is by replacing the glass support medium with cheaper alternatives like paper. Flexible $CuInSe_2$ nanocrystal solar cells are successfully fabricated on paper with efficiencies reaching up to 2.25%. This is the first time a nanocrystal solar cell has been fabricated on paper. There is no significant loss in PV device performance after more than 100 flexes to 5 mm radius, and the devices continue to perform when folded into a crease.

Apart from the absorber layer, the replacement of other high-temperature and vacuum processed device layers with ambient solution-processed layers lowers the manufacturing cost. This has been achieved by spin coating suitable nanomaterials as device layers.

Lastly, for commercialization of $CuInSe_2$ nanocrystal solar cells, multiple devices need to be connected to achieve the desired current and voltage. A fabrication process has been developed for building multiple nanocrystal PVs on a single substrate using 3D printed masks.

# Table of Contents

# List of Tables

# List of Figures

# Chapter 1: Introduction

## 1.1 Introduction to Photovoltaics

Solar cells, also referred to as photovoltaics (PVs), are devices that convert light into electricity. Since solar energy is available in abundant and is a renewable resource, there are economic and environmental benefits associated with the use of photovoltaics. Even though the cost of grid-parity solar is very competitive to fossil fuels, the main challenge is the high cost of module and installation leading to long payback periods.[1] Additionally, rooftop solar electricity costs higher than electricity generated from conventional energy sources, and it has difficulty in competing with electricity generated from fossil fuels.[2] Thus, reducing the cost of PV modules will lead to a greater penetration of solar energy into the energy sector.

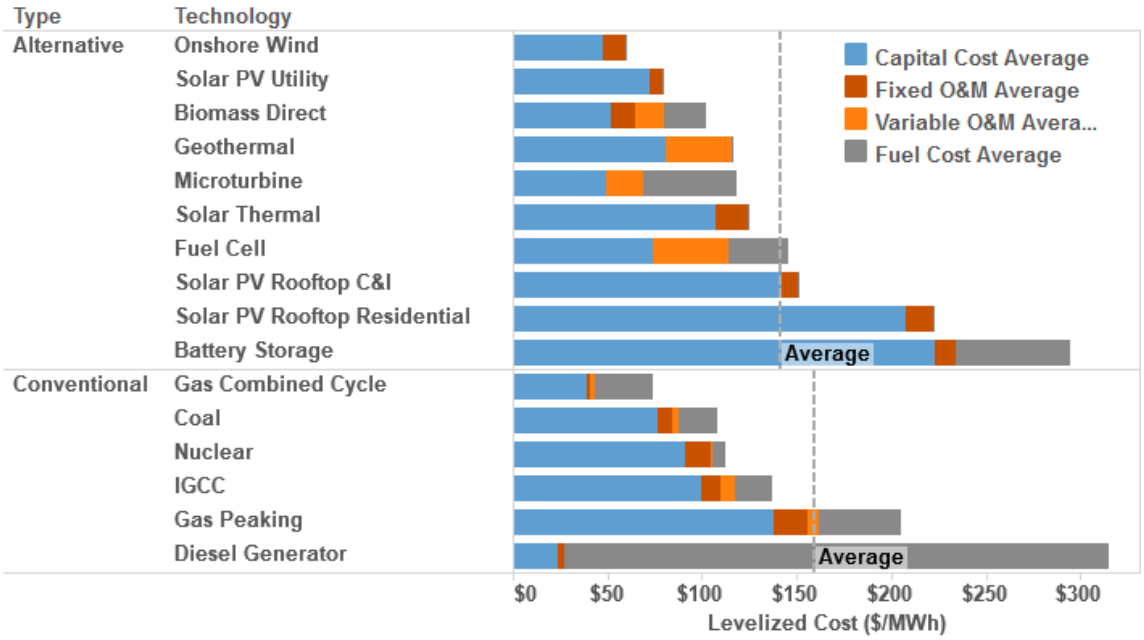


**Figure 1.1:** Levelized cost of electricity for various types of energy sources. [2]

## 1.2 SOLAR CELL TECHNOLOGIES

Various types of solar cells have been invented and they can broadly be categorized as silicon solar cells, thin film solar cells and solution processable solar cells.

### 1.2.1 Silicon Solar Cells

Silicon solar cells are the first kind of solar cells discovered. They were discovered in 1954 at Bell labs. These solar cells are the most efficient and widely used, serving 90% of the solar energy market.[3] Even though silicon is very abundant and inexpensive, the processing costs are higher because of the high temperature and ultralow vacuum needed during the deposition of silicon. Also, with silicon being an indirect band gap semiconductor, thick (≈ 100 μm) silicon layer is needed to absorb the light incident on the solar cell. Thick layers of high purity crystalline silicon significantly add to the cost of the solar device. Another disadvantage with thick absorber layers is that these solar cells cannot be flexed. Hence, they need to be fabricated on heavy rigid substrates like glass and are not a solution for portable power supply needs.

### 1.2.2 Thin Film Solar Cells

These solar cells typically employ amorphous-silicon, chalcogenide compounds (CdTe, Cu(In,Ga)(S,Se)). These materials are direct bandgap semiconductors and are capable of absorbing most of the incident light with thicknesses as low as 3-4 microns. [4–6] Such low thickness reduces the processing cost and makes the devices light-weight. Light-weight devices reduce the transportation and installation costs. GaAs is another material

used in thin film solar cells. Efficiencies as high as 27.5% have been obtained for these solar cells, but the cost of making the GaAs solar cells is higher than other thin film materials due to high processing costs.

### 1.2.3 Solution Processable Solar Cells

Even though thin film materials reduce the processing cost because of thinner absorber layers. Ultra-low vacuum and high temperature is still required for depositing those layers and leads to increased module costs. Solution processable solar cells eliminate this need for vacuum and in some cases don't even require temperatures above 200 ºC.[7,8] There are various kinds of solution processable solar cells including organic photovoltaics, dye sensitized solar cells, perovskites and nanocrystal solar cells.

In organic solar cells, the absorber material has a delocalized π electron cloud system that can absorb the sunlight and generate charge carriers. The advantage of organic solar cells is that they are flexible and light-weight but the materials used in organic solar cells have stability concerns and degrade in the air due to water and oxygen.[9,10] Also, the materials used in organic photovoltaics suffer from photochemical stability.[11]

Dye sensitized solar cells (DSSC) have similar advantages and disadvantages as an organic solar cell. At the heart of the device is a mesoporous oxide layer composed of a network of $TiO_2$ nanoparticles that are sintered together. A layer of charge-transfer dye is deposited over the surface of the mesoporous oxide layer. Photoexcitation of this layer results in injection of the electron into the conduction band of the oxide layer and this causes the oxidation of the dye. The dye is restored to the ground state by transfer of

electrons from electrolyte, usually an organic solvent containing the iodide/triiodide redox system.[12]

Perovskite solar cells have lately gained lot of popularity because of the high efficiencies achieved (up to 21%).[13] Compared to traditional silicon solar cells, these devices have an upper hand because of the ease of fabrication, strong light absorption and low non-radiative recombination losses.[14] Perovskites are the materials described by the formula $ABX_3$, where X is an anion, and A and B are cations of different sizes. The photogenerated electrons and holes coexist in the perovskite material which are separated and travel to their respective electrodes.[15] Just like OPVs and DSSCs, even perovskite suffer from stability concerns.[16]

Nanocrystal solar cells are devices where the absorber material is made up of nanocrystals. These devices have the benefits of solution processability, multi-excitation generation, band-gap tuning, flexibility, ambient temperature and pressure processing, and high absorption coefficient.[17,18] Quiet a few nanocrystals have been explored for use in solar cells including CdTe,[19] PbS,[20,21] PbSe,[22,23] $CuInS_2$, $CuInSe_2$,[24,25] $Cu_2ZnSnS_4$,[26,27]and perovskites.[28,29] In comparison with other solution processable solar cells, these devices have the added benefit of the materials being inherently stable.[18] The challenge for these devices is the hindrance to charge transfer caused by the long chain organic ligand surrounding the inorganic nanocrystal core, but a great deal of research has been done in replacing these long chain insulating ligands with small chain ligands which lead to an increase in device efficiency. [30–32] Complete removal of ligand has also been exploited in techniques such as selenization, which is used in Cu(InGa)(S,Se) solar cells where the

nanocrystals are sintered at high temperature (≈550 ºC) under selenium vapor. In this process, the ligands are removed and nanocrystals are sintered forming a polycrystalline film. Even though there is an improvement in efficiency, the high processing temperature defeats one of the processing advantages that nanocrystal solar cells could otherwise possess.[33]

## 1.3 DEVICE PHYSICS

Solar cells typically involve two kinds of semiconductors – p type and n type. Holes are the majority carriers in a p-type semiconductor, which are mainly responsible for the charge flow and hence can be termed as free holes. Whereas, in an n-type semiconductor, electrons are the majority charge carriers and are responsible for charge flow. Hence, these electrons are termed as free electrons. These two kinds of semiconductors are placed next to each other in a solar cell leading to the creation of a depletion region at the junction. When brought together, the free electrons and holes at the junction drift towards each other and recombine leaving no free electrons and holes at the junction. This region is called depletion region. This leads to the creation of an electric field from n-type to the p-type which prevent further recombination of free electrons and holes. If either both or one of the semiconductors have the right bandgap to absorb the photons and create electron hole pairs in the depletion region, the in-built electric field drives the electrons and holes causing current to flow in the circuit. The current flowing in the circuit when no opposing voltage is applied is termed as short circuit current of the solar cell ($I_{sc}$). The opposing voltage that is required to nullify the photocurrent generated in the circuit is termed as open circuit

voltage ($V_{oc}$). These two points are shown in the figure 1.2c on the IV curve. IV characteristics of a solar cell is a plot between the device current for a voltage sweep. A solar cell is operated in the fourth quadrant to get a power output. The maximum power point shown in the IV curve is where the product of current and voltage is maximum. It is desirable to operate the solar cell at the maximum power point ($P_{max}$). At either side of the junction there are electrodes for collecting these electrons or holes. One of the electrodes must be a transparent conducting oxide (TCO) so light can reach the junction.

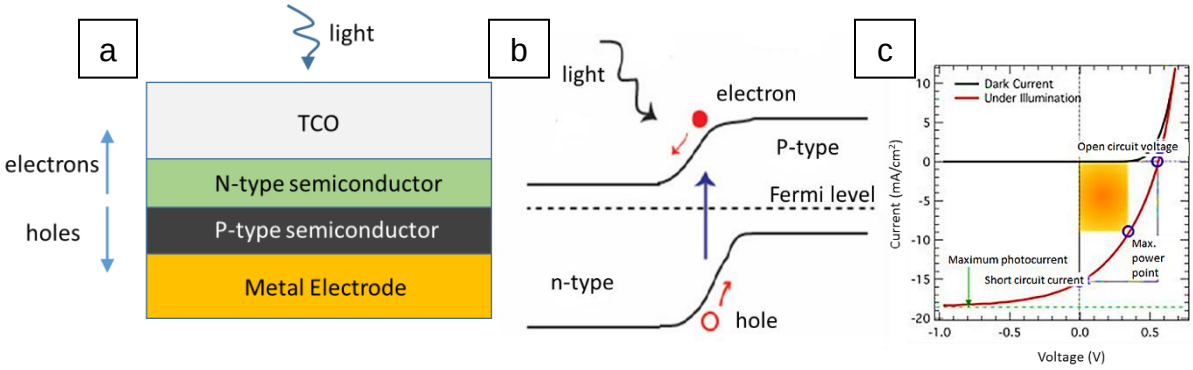


**Figure 1.2:** (a) Schematic shows different layers in a typical solar cell. (b) Band diagram of a p-n junction indicating the photo-generated carriers. (c) IV characteristics of a solar cell.

The power conversion efficiency (PCE) of a solar cell is defined as $P_{max}/P_{in}$. $P_{in}$ is the intensity of light falling on the solar cell. Hence, PCE depends on the intensity of light being used. For terrestrial applications, PCE is usually measured under simulated Air Mass 1.5 Global (AM1.5) full-sun illumination with 1 sun intensity ($P_{in}$ =100 mW/cm$^2$).[34] Hence with A.M. 1.5, the PCE is ($J_{sc}$* $V_{oc}$* FF / 100 mW/cm$^2$) where $J_{sc}$ is the short circuit current density, $V_{oc}$ is the open circuit voltage and FF is the fill factor. The other important efficiency measurement that can be done on solar cells is quantum efficiency. There are two kinds of

quantum efficiency measurements, external quantum efficiency (EQE) and internal quantum efficiency (IQE). EQE gives a measure of number of charge carriers extracted relative to the number of photons incident on the solar cell and IQE gives a measure of number of charge carriers extracted relative to the photons absorbed by the solar cell, at specific wavelengths. For a single junction solar cell that cannot extract hot electrons and holes, EQE and IQE values can be equal to 100% at certain wavelengths; whereas PCE is fundamentally limited to 34%.[35]

## 1.4 FLEXIBLE SOLAR CELLS

Flexible solar cells help the transition from fossil fuels to clean energy. Light-weight, flexible solar will require lower maintenance and can be easily integrated into already existing buildings, textiles, and any kind of surface. Compact solar power generators are needed for portable electronics and emergency situations. Conformal PV coverage of vehicles is needed in the transportation industry. Printed electronics and the packaging industry has the need of an on-board power generation that matches the form factor of consumer product labels and reduces reliance on batteries with finite lifetimes. Flexible, light-weight, low-cost solar cells would meet these needs and open entirely new applications for solar cells, leading to truly a universal use of photovoltaics. Typically, the light absorbing material in flexible solar cells is printed on a roll to roll conducting substrate which makes the fabrication process very effective. There are a few different types of flexible solar cells developed till date, and amorphous silicon solar cells are the most successful flexible PVs developed so far.[36,37] In comparison with crystalline silicon they have advantages of reduced processing temperature and material consumption.[38,39] Even though, the deposition of a-Si is done at low temperatures, vacuum is still needed for deposition which adds to the cost of manufacturing. Cu(In,Ga)Se thin film solar cells are the other kind of flexible solar cells that could be produced by roll-to-roll manufacturing,

but these solar cells are fabricated at higher temperatures and ultra-low vacuums resulting in high production costs.[40]

There has been a lot of hope in developing cheaper flexible solar cells after the emergence of organic and dye sensitized solar cells.[12,41] The main hurdle with these types of flexible solar cells is the encapsulation needed due to the instability of the solar cells. These solar cells are stable only when encapsulated in tightly sealed glass and would therefore make them inflexible.[42]$CuInSe_2$ nanocrystal solar cells are stable in the air and hence do not need tightly sealed glass packaging. The production costs are very low because of the ambient temperature and pressure fabrication process making $CuInSe_2$ nanocrystal solar cells the ideal choice for flexible PV applications. Shown in figure 1.3 are $CuInSe_2$ nanocrystal solar cells on paper. The portability and low weight make it possible for them to be used as a wearable power supply source.

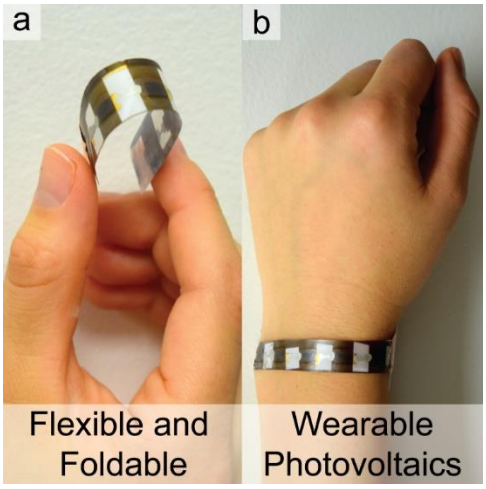


**Figure 1.3:** (a) Flexed $CuInSe_2$ nanocrystal solar cells on paper being bent. (b) $CuInSe_2$ nanocrystal solar cell on paper being used as a wearable.

## 1.5 $CuInSe_2$ Nanocrystal Solar Cells

The advantages of nanocrystal solar cells are discussed in section in 1.2.3. My research focuses on the development of $CuInSe_2$ nanocrystal solar cells. Compared to other materials, $CuInSe_2$ has benefits of longer stability and less toxicity. Bulk $Cu(In,Ga)Se_2$ devices have demonstrated efficiencies above 20%.[4] Nanocrystal $Cu(In,Ga)Se_2$ solar cells processed at high temperature (550 ºC) have demonstrated efficiencies above 7%.[33] The combination of lower toxicity and high efficiency exhibited by bulk and high temperature processed nanocrystal solar cells make $Cu(In,Ga)Se_2$ the ideal material to explore as nanocrystals. These nanocrystal solar cells could be fabricated on cheap substrates like paper and plastic thus enabling low cost fabrication. Such low-cost fabrication can enable the use of solar into new market areas where conventional solar panels cannot reach.

Figure 1.4 shows the different layers in a $CuInSe_2$ nanocrystal solar cell. The $CuInSe_2$ nanocrystal layer is deposited by techniques such as spray coating or spin coating. Typically, 4 to 8 solar cells having an area of 0.1 $cm^2$ are fabricated on a single substrate in order to have statistical data for a single set of experiments. The photograph of one such lab scale device on flexible substrate is provided in figure 1.4b.

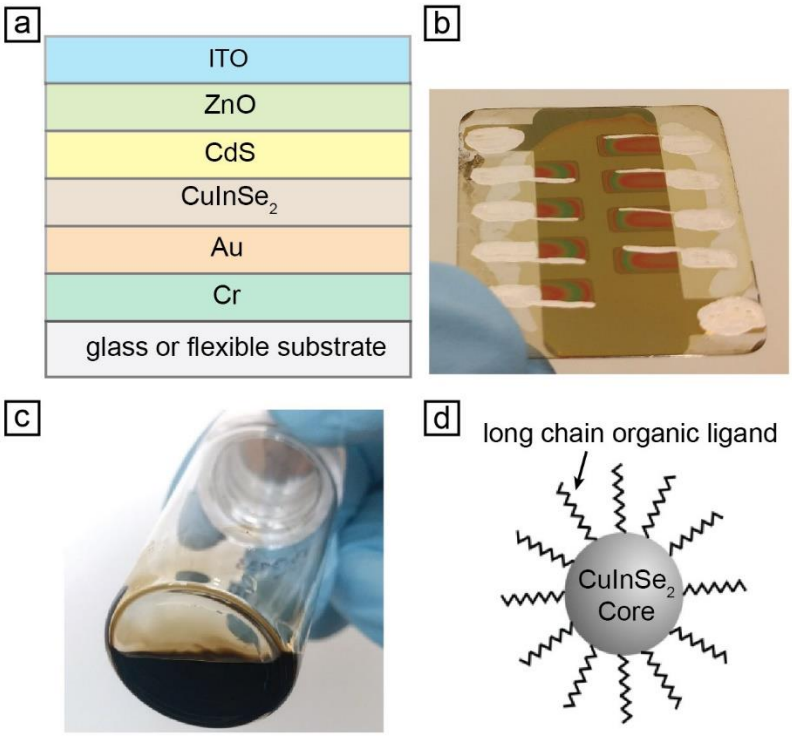


**Figure 1.4:** (a) Device layers in a $CuInSe_2$ solar cell. (b) Lab-scale $CuInSe_2$ nanocrystal solar cell showing 8 solar cells on Corning glass substrate. (c) Photograph of $CuInSe_2$ nanocrystal ink. (d) Illustration showing a $CuInSe_2$ nanocrystal core capped with long chain organic ligand.

Despite low-cost processing, $CuInSe_2$ nanocrystal solar cells are still at the development stage in the lab. This is primarily due to the low efficiency (3%) of $CuInSe_2$ nanocrystal solar cells and low product yield for $CuInSe_2$ nanocrystal synthesis.[43] However, their low-cost fabrication makes $CuInSe_2$ nanocrystal devices fit for commercialization at PCEs lower than that of the required PCE for other commercially available solar cells. Thus, efforts to bridge the gap between the PCEs of lab-scale prototypes and commercially available panels will enable cost-effective commercialization.

## 1.6 CONCLUSIONS AND DISSERTATION OVERVIEW

Herein, this gap is bridged by not only improving the device PCE, but also by further reducing the processing and material costs. To decrease nanocrystal device cost, studies have focused on finding suitable novel nanomaterials, increasing nanocrystal synthesis yields,[44–46] scaling up nanocrystal synthesis,[47] developing device fabrication on inexpensive, flexible substrates,[48,49] and engineering ligand exchanges.[8,30–32,50,51] In this work, a few of these objectives have been applied to $CuInSe_2$ nanocrystal devices by improving reaction yield, device efficiency, and processing methods.

Chapter 2 discusses about a new method developed for synthesizing $CuInSe_2$ nanocrystals that results in an improvement in the product yield without compromising on device efficiency. Chapter 3 focuses on improvement in the solar cell efficiency by ligand engineering. Ammonium sulfide has been used to replace the long chain organic ligands with sulfide ions, thus improving the charge transfer between nanocrystals. In chapter 4, processing methods for fabricating all-solution processed $CuInSe_2$ nanocrystal solar cells have been explained. Along with the already solution processed $CuInSe_2$ nanocrystal absorber layer, the thermally evaporated gold layer, sputtered zinc oxide and sputtered indium tin oxide layers have been replaced by solution processed layers of gold nanocrystals, zinc oxide nanocrystals and silver nanowires respectively. Chapter 5 focuses on $CuInSe_2$ nanocrystal solar cells fabricated on paper. Very flexible solar cells have been fabricated on bacterial cellulose paper. Chapter 6 discusses the development of large area $CuInSe_2$ nanocrystal solar cells. This includes development of prototypes that deliver the

required amount of voltage and current depending on the application. Finally, chapter 7 provides the overall conclusions and future directions for this research.

## 1.7 REFERENCES


(1) Solar Energy vs Fossil Fuels: How Do They Compare? | EnergySage http://news.energysage.com/solar-energy-vs-fossil-fuels/ (accessed Sep 13, 2017).

(2) Comparing the levelized cost of energy technologies http://energyinnovation.org/2015/02/07/levelized-cost-of-energy/ (accessed Sep 13, 2017).

(3) Solar Cell Market Size, Share | Industry Report, 2022 http://www.grandviewresearch.com/industry-analysis/solar-cell-market (accessed Sep 13, 2017).

(4) Jackson, P.; Hariskos, D.; Lotter, E.; Paetel, S.; Wuerz, R.; Menner, R.; Wischmann, W.; Powalla, M. New World Record Efficiency for Cu(In,Ga)Se2 Thin-Film Solar Cells beyond 20%. *Prog. Photovolt. Res. Appl.* **2011**, *19*, 894–897.

(5) Repins, I.; Contreras, M. A.; Egaas, B.; DeHart, C.; Scharf, J.; Perkins, C. L.; To, B.; Noufi, R. 19·9%-Efficient ZnO/CdS/$CuInGaSe_2$ Solar Cell with 81·2% Fill Factor. *Prog. Photovolt. Res. Appl.* **2008**, *16*, 235–239.

(6) Poplawsky, J. D. Cadmium Telluride Solar Cells: Record-Breaking Voltages. *Nat. Energy* **2016**, *1*, nenergy201621.

(7) Sun, S.; Salim, T.; Mathews, N.; Duchamp, M.; Boothroyd, C.; Xing, G.; Chien Sum, T.; Ming Lam, Y. The Origin of High Efficiency in Low-Temperature Solution-Processable Bilayer Organometal Halide Hybrid Solar Cells. *Energy Environ. Sci.* **2014**, *7*, 399–407.

(8) Tang, J.; Kemp, K. W.; Hoogland, S.; Jeong, K. S.; Liu, H.; Levina, L.; Furukawa, M.; Wang, X.; Debnath, R.; Cha, D.; *et al.* Colloidal-Quantum-Dot Photovoltaics Using Atomic-Ligand Passivation. *Nat. Mater.* **2011**, *10*, 765–771.

(9) Kawano, K.; Pacios, R.; Poplavskyy, D.; Nelson, J.; Bradley, D. D. C.; Durrant, J. R. Degradation of Organic Solar Cells due to Air Exposure. *Sol. Energy Mater. Sol. Cells* **2006**, *90*, 3520–3530.

(10) Janssen, R. A. J.; Hummelen, J. C.; Saricifici, N. S. Polymer–Fullerene Bulk Heterojunction Solar Cells. *MRS Bull.* **2005**, *30*, 33–36.

(11) Manceau, M.; Bundgaard, E.; E. Carlé, J.; Hagemann, O.; Helgesen, M.; Søndergaard, R.; Jørgensen, M.; C. Krebs, F. Photochemical Stability of π-

Conjugated Polymers for Polymer Solar Cells: A Rule of Thumb. *J. Mater. Chem.* **2011**, *21*, 4132–4141.

(12) Hagfeldt, A.; Boschloo, G.; Sun, L.; Kloo, L.; Pettersson, H. Dye-Sensitized Solar Cells. *Chem. Rev.* **2010**, *110*, 6595–6663.

(13) Assadi, M. K.; Bakhoda, S.; Saidur, R.; Hanaei, H. Recent Progress in Perovskite Solar Cells. *Renew. Sustain. Energy Rev.*

(14) Green, M. A.; Ho-Baillie, A.; Snaith, H. J. The Emergence of Perovskite Solar Cells. *Nat. Photonics* **2014**, *8*, 506–514.

(15) Gonzalez-Pedro, V.; Juarez-Perez, E. J.; Arsyad, W.-S.; Barea, E. M.; Fabregat-Santiago, F.; Mora-Sero, I.; Bisquert, J. General Working Principles of $CH_3NH_3PbX_3$ Perovskite Solar Cells. *Nano Lett.* **2014**, *14*, 888–893.

(16) Niu, G.; Guo, X.; Wang, L. Review of Recent Progress in Chemical Stability of Perovskite Solar Cells. *J. Mater. Chem. A* **2015**, *3*, 8970–8980.

(17) Kamat, P. V. Quantum Dot Solar Cells. Semiconductor Nanocrystals as Light Harvesters. *J. Phys. Chem. C* **2008**, *112*, 18737–18753.

(18) Gur, I.; Fromer, N. A.; Geier, M. L.; Alivisatos, A. P. Air-Stable All-Inorganic Nanocrystal Solar Cells Processed from Solution. *Science* **2005**, *310*, 462–465.

(19) Panthani, M. G.; Kurley, J. M.; Crisp, R. W.; Dietz, T. C.; Ezzyat, T.; Luther, J. M.; Talapin, D. V. High Efficiency Solution Processed Sintered CdTe Nanocrystal Solar Cells: The Role of Interfaces. *Nano Lett.* **2014**, *14*, 670–675.

(20) Yoon, W.; Boercker, J. E.; Lumb, M. P.; Placencia, D.; Foos, E. E.; Tischler, J. G. Enhanced Open-Circuit Voltage of PbS Nanocrystal Quantum Dot Solar Cells. *Sci. Rep.* **2013**, *3*, srep02225.

(21) Zhao, N.; Osedach, T. P.; Chang, L.-Y.; Geyer, S. M.; Wanger, D.; Binda, M. T.; Arango, A. C.; Bawendi, M. G.; Bulovic, V. Colloidal PbS Quantum Dot Solar Cells with High Fill Factor. *ACS Nano* **2010**, *4*, 3743–3752.

(22) Schaller, R. D. High Efficiency Carrier Multiplication in PbSe Nanocrystals: Implications for Solar Energy Conversion. *Phys. Rev. Lett.* **2004**, *92*.

(23) Choi, J. J.; Lim, Y.-F.; Santiago-Berrios, M. B.; Oh, M.; Hyun, B.-R.; Sun, L.; Bartnik, A. C.; Goedhart, A.; Malliaras, G. G.; Abruña, H. D.; *et al.* PbSe Nanocrystal Excitonic Solar Cells. *Nano Lett.* **2009**, *9*, 3749–3755.

(24) Guo, Q.; Kim, S. J.; Kar, M.; Shafarman, W. N.; Birkmire, R. W.; Stach, E. A.; Agrawal, R.; Hillhouse, H. W. Development of CuInSe2 Nanocrystal and Nanoring Inks for Low-Cost Solar Cells. *Nano Lett.* **2008**, *8*, 2982–2987.

(25) Voggu, V. R.; Sham, J.; Pfeffer, S.; Pate, J.; Fillip, L.; Harvey, T. B.; Brown, R. M.; Korgel, B. A. Flexible $CuInSe_2$ Nanocrystal Solar Cells on Paper. *ACS Energy Lett.* **2017**, *2*, 574–581.

(26) Guo, Q.; Hillhouse, H. W.; Agrawal, R. Synthesis of $Cu_2ZnSnS_4$ Nanocrystal Ink and Its Use for Solar Cells. *J. Am. Chem. Soc.* **2009**, *131*, 11672–11673.

(27) Guo, Q.; Ford, G. M.; Yang, W.-C.; Walker, B. C.; Stach, E. A.; Hillhouse, H. W.; Agrawal, R. Fabrication of 7.2% Efficient CZTSSe Solar Cells Using CZTS Nanocrystals. *J. Am. Chem. Soc.* **2010**, *132*, 17384–17386.

(28) Kojima, A.; Teshima, K.; Shirai, Y.; Miyasaka, T. Organometal Halide Perovskites as Visible-Light Sensitizers for Photovoltaic Cells. *J. Am. Chem. Soc.* **2009**, *131*, 6050–6051.

(29) Kazim, S.; Nazeeruddin, M. K.; Grätzel, M.; Ahmad, S. Perovskite as Light Harvester: A Game Changer in Photovoltaics. *Angew. Chem. Int. Ed.* **2014**, *53*, 2812–2824.

(30) Barkhouse, D. A. R.; Pattantyus-Abraham, A. G.; Levina, L.; Sargent, E. H. Thiols Passivate Recombination Centers in Colloidal Quantum Dots Leading to Enhanced Photovoltaic Device Efficiency. *ACS Nano* **2008**, *2*, 2356–2362.

(31) Koleilat, G. I.; Levina, L.; Shukla, H.; Myrskog, S. H.; Hinds, S.; Pattantyus-Abraham, A. G.; Sargent, E. H. Efficient, Stable Infrared Photovoltaics Based on Solution-Cast Colloidal Quantum Dots. *ACS Nano* **2008**, *2*, 833–840.

(32) Pattantyus-Abraham, A. G.; Kramer, I. J.; Barkhouse, A. R.; Wang, X.; Konstantatos, G.; Debnath, R.; Levina, L.; Raabe, I.; Nazeeruddin, M. K.; Grätzel, M.; *et al.* Depleted-Heterojunction Colloidal Quantum Dot Solar Cells. *ACS Nano* **2010**, *4*, 3374–3380.

(33) Harvey, T. B.; Mori, I.; Stolle, C. J.; Bogart, T. D.; Ostrowski, D. P.; Glaz, M. S.; Du, J.; Pernik, D. R.; Akhavan, V. A.; Kesrouani, H.; *et al.* Copper Indium Gallium Selenide (CIGS) Photovoltaic Devices Made Using Multistep Selenization of Nanocrystal Films. *ACS Appl. Mater. Interfaces* **2013**, *5*, 9134–9140.

(34) Nelson, J. *The Physics of Solar Cells*; World Scientific Publishing Company, 2003.

(35) Henry, C. H. Limiting Efficiencies of Ideal Single and Multiple Energy Gap Terrestrial Solar Cells. *J. Appl. Phys.* **1980**, *51*, 4494–4500.

(36) Gregg, A.; Blieden, R.; Chang, A.; Ng, H. Performance Analysis of Large Scale, Amorphous Silicon, Photovoltaic Power Systems. In *Conference Record of the Thirty-first IEEE Photovoltaic Specialists Conference, 2005.*; 2005; pp. 1615–1618.

(37) Zhang, C.; Song, Y.; Wang, M.; Yin, M.; Zhu, X.; Tian, L.; Wang, H.; Chen, X.; Fan, Z.; Lu, L.; *et al.* Solar Cells: Efficient and Flexible Thin Film Amorphous Silicon Solar Cells on Nanotextured Polymer Substrate Using Sol–gel Based Nanoimprinting Method (Adv. Funct. Mater. 13/2017). *Adv. Funct. Mater.* **2017**, *27*, n/a-n/a.

(38) Haug, F.-J.; Ballif, C. Light Management in Thin Film Silicon Solar Cells. *Energy Environ. Sci.* **2015**, *8*, 824–837.

(39) Shah, A. V.; Platz, R.; Keppner, H. Thin-Film Silicon Solar Cells: A Review and Selected Trends. *Sol. Energy Mater. Sol. Cells* **1995**, *38*, 501–520.

(40) Kessler, F.; Rudmann, D. Technological Aspects of Flexible CIGS Solar Cells and Modules. *Sol. Energy* **2004**, *77*, 685–695.

(41) Brabec, C. J. Organic Photovoltaics: Technology and Market. *Sol. Energy Mater. Sol. Cells* **2004**, *83*, 273–292.

(42) Niggemann, M.; Glatthaar, M.; Gombert, A.; Hinsch, A.; Wittwer, V. Diffraction Gratings and Buried Nano-Electrodes—architectures for Organic Solar Cells. *Thin Solid Films* **2004**, *451–452*, 619–623.

(43) Akhavan, V. A.; Panthani, M. G.; Goodfellow, B. W.; Reid, D. K.; Korgel, B. A. Thickness-Limited Performance of CuInSe_2 Nanocrystal Photovoltaic Devices. *Opt. Express* **2010**, *18*, A411.

(44) Panthani, M. G.; Akhavan, V.; Goodfellow, B.; Schmidtke, J. P.; Dunn, L.; Dodabalapur, A.; Barbara, P. F.; Korgel, B. A. Synthesis of CuInS2, CuInSe2, and $Cu(In_xGa_{1-x})Se_2$ (CIGS) Nanocrystal "Inks" for Printable Photovoltaics. *J. Am. Chem. Soc.* **2008**, *130*, 16770–16777.

(45) Evans, C. M.; Evans, M. E.; Krauss, T. D. Mysteries of TOPSe Revealed: Insights into Quantum Dot Nucleation. *J. Am. Chem. Soc.* **2010**, *132*, 10973–10975.

(46) Panthani, M. G.; Stolle, C. J.; Reid, D. K.; Rhee, D. J.; Harvey, T. B.; Akhavan, V. A.; Yu, Y.; Korgel, B. A. $CuInSe_2$ Quantum Dot Solar Cells with High Open-Circuit Voltage. *J. Phys. Chem. Lett.* **2013**, *4*, 2030–2034.

(47) Zhang, L.; Xia, Y. Scaling up the Production of Colloidal Nanocrystals: Should We Increase or Decrease the Reaction Volume? *Adv. Mater.* **2014**, *26*, 2600–2606.

(48) Brabec, C. J.; Sariciftci, N. S.; Hummelen, J. C. Plastic Solar Cells. *Adv. Funct. Mater.* **2001**, *11*, 15–26.

(49) Shaheen, S. E.; Brabec, C. J.; Sariciftci, N. S.; Padinger, F.; Fromherz, T.; Hummelen, J. C. 2.5% Efficient Organic Plastic Solar Cells. *Appl. Phys. Lett.* **2001**, *78*, 841–843.

(50) Chuang, C.-H. M.; Brown, P. R.; Bulović, V.; Bawendi, M. G. Improved Performance and Stability in Quantum Dot Solar Cells through Band Alignment Engineering. *Nat. Mater.* **2014**, *13*, 796–801.

(51) McDonald, S. A.; Konstantatos, G.; Zhang, S.; Cyr, P. W.; Klem, E. J. D.; Levina, L.; Sargent, E. H. Solution-Processed PbS Quantum Dot Infrared Photodetectors and Photovoltaics. *Nat. Mater.* **2005**, *4*, 138–142.

# Chapter 2: Improved $CuInSe_2$ Nanocrystal Synthesis

## 2.1 INTRODUCTION

$CuInSe_2$ is a promising material for nanocrystal solar cells because it is well-characterized with low toxicity and can be solution processed in ambient conditions. There have been multiple different batch synthesis routes for preparing $CuInSe_2$ nanocrystals.[1–5] The highest reported efficiencies achieved in solar cells fabricated at low temperature ($\leq$ 200 ºC) employing these nanocrystals have been 3.1-3.2%, but we observed that these reactions have low yields.[5,6] Improving the quantity of nanocrystals produced from one batch of nanocrystal synthesis reduces material costs. We define reaction yield as

$$\frac{\text{experimental mass of product obtained}}{\text{theoretical mass of product obtained if complete conversion achieved}}\ x\ 100\%$$

We will discuss reaction yields of three different synthesis routes previously published in literature that we slightly modified and explored in solar cells.[1,6,7] We termed the three reactions "One pot synthesis," "DPP:Se injection synthesis," and "TBP:Se injection synthesis" for ease of reference. As the names indicate, the DPP:Se and TBP:Se injection methods have DPP and TBP in addition to all the other chemicals present in a one pot synthesis. We identify that tributylphosphine (TBP) introduced during $CuInSe_2$ nanocrystal synthesis binds to the nanocrystal surface and improves the $CuInSe_2$ nanocrystal device performance. This finding aided our development of an optimized synthesis method for $CuInSe_2$ nanocrystals involving both diphenylphosphine (DPP) to increase the product yield and tributylphosphine to increase the device performance. We

termed this reaction as the “Hybrid reaction”, which is a combination of the DPP:Se and TBP:Se injection synthesis.

## 2.2 EXPERIMENTAL METHODS

### 2.2.1 Materials

Oleylamine (OLA, 70%); copper (I) chloride (CuCl; 99.99+%), selenium powder (Se; 99.99%), diphenylphosphine (DPP, 98%), thiourea (< 99.0%), cadmium sulfate ($CdSO_4$; 99.999%), copper, indium and selenium standard ICP solutions with concentrations of 1mg/ml, 70% wt. nitric acid were purchased from Aldrich Chemical Co.; indium (III) chloride ($InCl_3$; 99.999%) was purchased from Strem Chemicals; ammonium hydroxide (18M $NH_3$; ACS certified), toluene (99.99%), ethanol (absolute) were purchased from Fischer Scientific. Prior to use, oleylamine was degassed overnight under vacuum at 110 °C using a standard Schlenk line set up in a 3-neck round bottom flask and stored in a nitrogen filled glovebox. All other chemicals were used as received without further purification.

### 2.2.2 $CuInSe_2$ Quantum Dot Synthesis

#### *2.2.2.1 One pot Method*

$CuInSe_2$ nanocrystals from the one pot synthesis were prepared based on a previously published method.[1] CuCl (0.495 g, 5 mmol), $InCl_3$ (1.11 g, 5 mmol), Se (0.79 g, 10 mmol) and 50 ml of OLA are added to a 150 mL, 3-neck round bottom flask inside a nitrogen-filled glovebox and sealed with a rubber septa before bringing the flask out of the glovebox. This flask is attached to a schlenk line, vacuum is applied, the flask is heated to 110 ºC and maintained at this temperature overnight. Then, the flask is filled with nitrogen and the temperature is ramped at 12 ºC/min to 240 ºC. The reaction mixture is maintained

at this temperature for 45 minutes, during which $CuInSe_2$ nanocrystals grow. The heating mantle is then removed and the reaction mixture is allowed to cool to room temperature under nitrogen.

The reaction mixture is transferred into glass centrifuge tubes and 20 mL of ethanol is added. This mixture is centrifuged at 4500 rpm for 10 minutes to isolate the nanocrystals from the reaction mixture. The dark green supernatant is discarded and toluene is added in steps of 1 mL to the separated nanocrystals, using a glass pipette, until they are redispersed. 20 mL of ethanol is then added to the redispersed nanocrystals and centrifuged at 4500 rpm for 10 more minutes. The supernatant is discarded and nanocrystals are redispersed in a minimal amount of toluene. Toluene is then evaporated from this dispersion using a rotovap and the dried nanocrystals are moved into a nitrogen filled glovebox, where they are dispersed in anhydrous toluene and stored at a concentration of 100 mg/mL until further use.

#### *2.2.2.2 DPP:Se Injection Method*

This synthesis is a modification of a previously published method.[7] CuCl (0.198 g, 2 mmol), $InCl_3$ (0.442 g, 2 mmol) and 10 mL OLA are mixed in a 50 mL, 3-neck round bottom flask inside a nitrogen-filled glovebox and sealed with a rubber septa. The flask is moved out and vacuum is applied using a schlenk line. The mixture is heated to 110 ºC and maintained at that temperature overnight. The flask is then purged with nitrogen gas and maintained at 110 ºC for 10 minutes. The reaction temperature is then ramped to 180 ºC and a solution of Se (0.316 g, 4 mmol) and DPP (1.5 mL), which is prepared in the

glovebox, is injected rapidly into the reaction mixture using a glass syringe. The reaction mixture is then heated to 240 ºC for 45 minutes and allowed to cool to room temperature in a nitrogen atmosphere.

To separate the nanocrystals, the reaction mixture is transferred into glass centrifuge tubes and 20 mL of ethanol is added. The mixture is centrifuged at 4500 rpm for 10 minutes and the resulting supernatant is discarded. The separated nanocrystals are redispersed in minimal amount of toluene, which is added drop wise using a glass pipette. 20 mL of ethanol is added and the dispersion is again centrifuged at 4500 rpm for 10 minutes. The supernatant is again discarded and the nanocrystals are redispersed in a minimal amount of toluene. The dispersion is the transferred into a 20-mL glass vial and dried out using a rotovap. The dried-out nanocrystal vial is transferred into a nitrogen filled glovebox and anhydrous toluene is added to redisperse the nanocrystals. The dispersion is stored at a concentration of 100 mg/mL in the nitrogen-filled glovebox.

#### *2.2.2.3 TBP:Se Injection Method*

$CuInSe_2$ nanocrystals were synthesized as previously described.[6] Briefly, 5 mmol of CuCl (0.495 g), 5 mmol of $InCl_3$ (1.11 g), 50 mL of degassed OLA and a magnetic stir bar are sealed in a 125-mL three-neck flask with rubber septa in a $N_2$ filled glovebox and attached to a conventional Schlenk line setup. Vacuum is pulled in the flask at 110 °C for 30 min, followed by $N_2$ bubbling at 110 °C for 10 minutes while stirring. A 1M solution of Se in TBP is separately prepared in the glovebox by dissolving 10 mmol of Se (0.79 g) in 10 ml TBP in a 20 mL vial under magnetic stirring. The resulting Se reactant solution is

drawn into a syringe and taken outside the glovebox in preparation for injection into the reaction flask on the Schlenk line. At this point, the temperature of the reaction flask is raised to 240 °C. When the temperature in the flask reaches 180 ºC, the TBP:Se stock solution is injected into the flask. The reaction mixture is then maintained at 240 ºC for 10 minutes. The heating mantle is removed from the flask to let the contents in the flask to cool to room temperature.

The contents of the reaction flask are transferred to a centrifuge tube and 20 ml of ethanol is added. The nanocrystal product is precipitated by centrifugation at 4500 rpm for 10 minutes. The supernatant is discarded. The nanocrystal product is redispersed in 5 mL of toluene and 6 ml of ethanol is added. This mixture is again centrifuged at 4500 rpm for 10 minutes to precipitate the nanocrystals. The supernatant is discarded, and the solid product is redispersed in toluene to a final concentration of 100 mg/ml in a nitrogen filled glovebox.

#### *2.2.2.4 Hybrid Method*

CuInSe2 nanocrystals were synthesized using reported methods.[8] In a $N_2$ filled glove box, 0.495 g CuCl, 1.11 g $InCl_3$, 1.5 ml DPP and 50 mL oleylamine are combined in a three neck flask, removed from the glovebox and attached to a standard Schlenk line. After degassing the reaction by pulling vacuum at 110 °C for 30 min, The flask is filled with $N_2$ and the temperature is maintained at 110ºC for 10 min. The temperature is then raised to 180ºC and 0.79 g of Se dissolved in 10 ml of TBP is rapidly injected into the reaction mixture. The temperature is then raised to 240 ºC and held for 10 minutes.

Purification of the nanocrystals is conducted by centrifugation using toluene/ethanol as solvent and antisolvent. The nanocrystals are precipitated by centrifuging at 4500 rpm for 10 min after adding 20 ml of ethanol, then redispersed in 5 ml of toluene and 6 ml of ethanol is added. The mixture is then centrifuged again at 4500 rpm for 10 minutes. The final solution is prepared by redispersing the nanocrystals in anhydrous toluene in a nitrogen filled glove box to a concentration of 100 mg/ml.

### 2.2.3 Materials Characterization

Transmission electron microscopy (TEM) was performed using FEI Tecnai G2 Spirit BioTwin microscopy operated at 80 kV. TEM samples were prepared by drop casting nanocrystals dispersed in chloroform onto a 200 mesh copper grid with a carbon film (Electron Microscopy Sciences). Energy dispersive X-ray spectroscopy (EDS) was carried out using an Bruker Quantax 200 detector mounted on a Hitachi S-5500 STEM. X-ray diffraction (XRD) was performed using a Rigaku R-Axis Spider diffractometer using Cu Kα (λ= 1.54 Å) radiation operated at 40 kV and 40 mA. Inductively Coupled Plasma-Optical Emission Spectrometers (ICP-OES) composition measurements were carried out on a Varian 710 ICP-OES instrument. Standard solutions for each of Cu, In and Se were prepared with their respective standards at concentrations of 0, 0.1, 0.5, 1, 5, and 10 mg/L. ICP-OES samples were prepared by digesting approximately 5 mg of $CuInSe_2$ nanocrystals into 1 ml of 70% nitric acid. The samples were then further diluted with 9 mL of DI water. 0.1 mL of each sample was the taken and mixed with 9.9 mL of 3% nitric acid to obtain a final product concentration of ~5 mg/L. Each element's concentration in the solution is

estimated from the calibration curve that is created by fitting the emission intensity of the standard solutions to a linear trend line.

### 2.2.4 PV Device Fabrication and Testing

Polished glass slides of size 25 mm x 12.5 mm were obtained from Delta Technologies. These slides were cleaned by sonicating in a 1:1 ratio of acetone and isopropyl alcohol for 5 minutes, followed by sonication in DI water for 5 minutes. The glass slides are then air dried. A 5-nm chrome (99.999%, Lesker) layer followed by a 60-nm layer of gold (99.95%, Lesker) is deposited by thermal evaporation. The gold layer serves as the back-contact electrode for the solar cell. $CuInSe_2$ nanocrystal layer is deposited by spin coating as follows. 100 mg/mL of $CuInSe_2$ nanocrystal solution is filtered through a 0.45 μm pore size filter and then diluted to 50 mg/mL by adding toluene. This dispersion is drop casted onto the gold coated glass substrate, which is spun at 600 rpm for 3 seconds followed by 2000 rpm for 40 seconds to deposit a 200 nm thick $CuInSe_2$ nanocrystal layer. CdS was deposited by chemical surface deposition method. 0.7 mL of a CdS precursor solution (1.25 mL of 15 mM CdSO4, 2.2 mL of 1.5 M thiourea, and 2.8 mL of 18 M NH4OH in water) was drop casted onto a pre-heated $CuInSe_2$ and gold coated glass substrate maintained at 90 ºC using a hot plate and covered with an inverted crystallization dish. The CdS precursor solution is allowed to react for 2 minutes, after which the excess solution is rinsed off with DI water. The substrates are then dried by blowing compressed nitrogen. The next two layers i-ZnO and ITO were deposited by Radio Frequency (RF) sputtering using ZnO (99.9%) and ITO (99.99 % $In_2O_3$:$SnO_2$ 9:1) targets

in Argon atmosphere. ZnO and ITO are deposited selectively onto 4 rectangular regions of area ranging from 0.08 $cm^2$ to 0.13 $cm^2$ using shadow masking. Silver paint is applied to the top and bottom contacts for PV testing. For baking the devices, they are placed in a rapid thermal processing (RTP) furnace and ramped at 1.5 ºC/minute to reach the required temperature under air/argon/vacuum.

The current-voltage measurements were performed under an A.M1.5 solar simulation, using a Keithley 2400 general purpose source meter. The light source is calibrated using a NIST- calibrated Si photodiode (Hamamatsu, S1787-08).

## 2.3 RESULTS AND DISCUSSION

Figure 2.1 shows the reaction yields and device characteristics for the $CuInSe_2$ nanocrystals synthesized from the four different synthesis routes mentioned above. All the synthesis routes produce a product of nanocrystals with ligands attached to their surface. We are interested in the yield of nanocrystals without their ligands. Hence, we subtracted the weight of the ligands from the weight of the final product when we calculated reaction yield. TGA was used to determine the weight of ligands that needed to be subtracted.

The DPP:Se injection reaction yields the maximum product, with a reaction yield of 87 %, while the TBP:Se injection method yields the least amount, with a reaction yield of only 4%. This role of DPP, a secondary phosphine, at improving reaction yield has been observed before, in II-VI and IV-VI nanocrystal syntheses.[9] However, the nanocrystals synthesized from the DPP:Se injection method are not the ideal choice for solar cells because the average PCE of the devices is two-fold lower for nanocrystals made from

DPP:Se than from the TBP:Se injection method (figure 1). In order to obtain the advantages of high yield from the DPP:Se injection method and high PCE from TBP:Se injection method, we developed the Hybrid synthesis method, which involves both DPP and TBP in the reaction mixture.

We are interested in comparing the three reaction method device efficiencies. In literature, heating devices after fabrication at 200 ºC in vacuum for 10 minutes led to an increase in PCE for devices made from particles synthesized by TBP:Se injection method.[6] We observed that the devices fabricated utilizing nanocrystals from the one pot and DPP:Se injection method were not able to withstand the temperature of 200 ºC, and hence, heating the devices resulted in shorting. Also, for fabricating $CuInSe_2$ nanocrystal devices on inexpensive substrates like plastics, processing temperatures must be lower than 100 ºC. Hence, we were interested in comparing device efficiencies before baking. We studied ligand content, crystal structure, nanocrystal size, nanocrystal stoichiometry, and type of ligand in each method to account for their devices' differences in PCE.

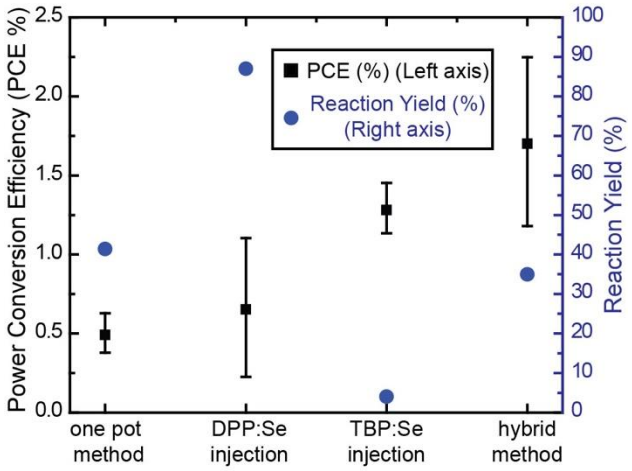


**Figure 2.1:** Plot showing PCEs (%) and reaction yields (%) for different nanocrystal synthesis routes. PCE values ( ■ ) are plotted with the scale on the left axis and the reaction yields ( ● ) with the scale on the right axis.

Thermogravimetric analysis (TGA) was used to determine the amount of organic capping ligand in the synthesized nanocrystals. TGA data in figure 2.2 shows no direct correlation between the amount of organic ligand content and PCE because low organic content did not yield a high PCE. Hence, ligand content is not the main determining factor in device performance. Nanocrystals from the one pot method have the least amount of organic content, but not the highest PCE. Similarly, nanocrystal size did not show any direct correlation and nanocrystal structure was the same, chalcopyrite, for each synthesis route. The data supporting nanocrystal size and structure is available in the figure 2.3.

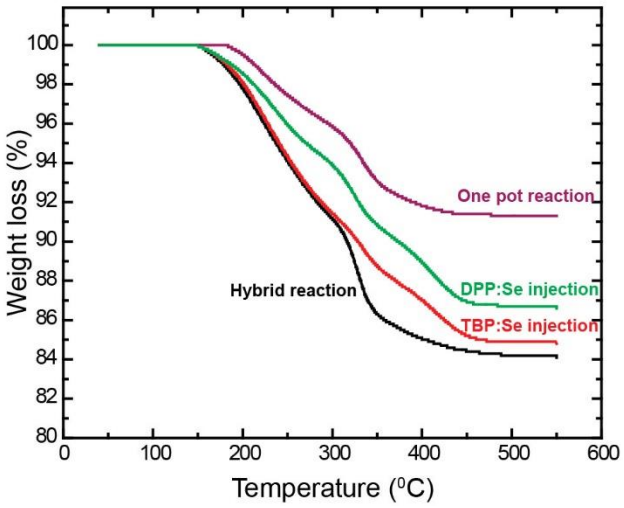


**Figure 2.2:** Thermogravimetric analysis performed on $CuInSe_2$ nanocrystals synthesized by various methods

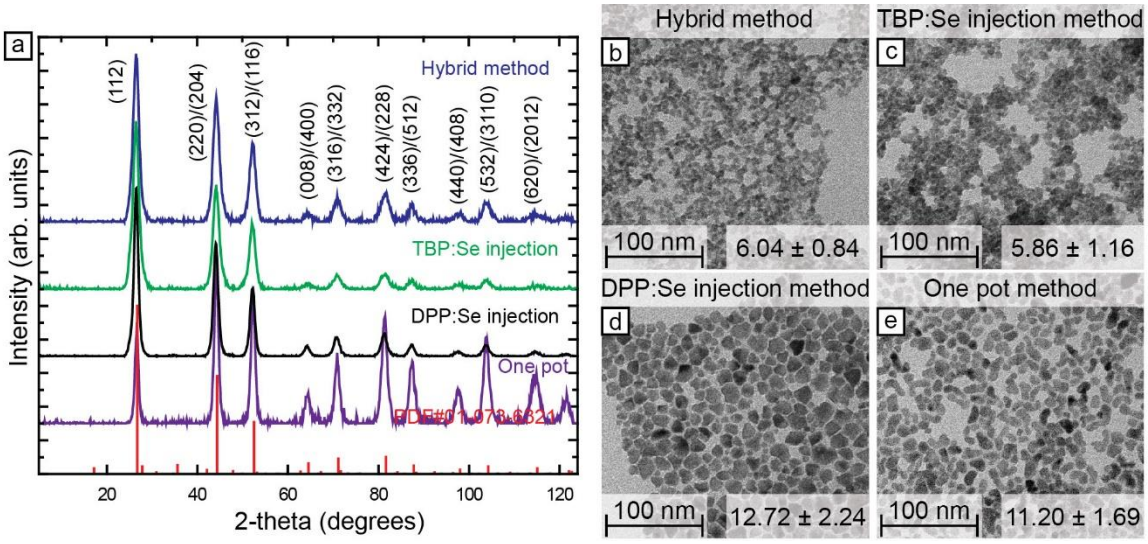


**Figure 2.3:** (a) XRD and (b-e) TEM of $CuInSe_2$ nanocrystals synthesized from four different synthesis. The size of nanocrystals with standard deviation is shown on each TEM image and we did not observe any direct correlation between size of nanocrystals and PCE (plotted in figure 2.1)

The two main factors that affect device performance are stoichiometry of the nanocrystals and the type of ligands attached to the nanocrystal surface. Table 2.1 shows

the elemental analysis obtained from inductively coupled plasma atomic emission spectroscopy (ICP-AES), normalized to a selenium content of 2. EDX data (table 2.2) showed similar trend in the stoichiometry. Lower copper content in the nanocrystals improved the device performance (ref. figure 2.1). A copper content lower than the stoichiometric amounts has been proven essential for the better performance of bulk copper indium gallium selenide (CIGS) devices.[10,11] We observe a similar trend with the $CuInSe_2$ nanocrystal solar cells.

| Synthesis | Cu | In | Se |
|---|---|---|---|
| **One pot** | 0.96 | 1.04 | 2 |
| **DPP:Se injection** | 0.90 | 1.04 | 2 |
| **TBP:Se injection** | 0.81 | 1.03 | 2 |
| **Hybrid** | 0.76 | 1.04 | 2 |

**Table 2.1:** Elemental analysis of $CuInSe_2$ nanocrystals synthesized by different methods obtained from ICP-AES

| element | Cu | In | Se |
|---|---|---|---|
| **One pot** | 0.94 ± 0.05 | 1.09 ± 0.13 | 2.00 ± 0.13 |
| **DPP:Se injection** | 0.87 ± 0.05 | 1.08 ± 0.12 | 2.00 ± 0.12 |
| **TBP:Se injection** | 0.84 ± 0.04 | 1.06 ± 0.11 | 2.00 ± 0.12 |
| **Hybrid** | 0.80 ± 0.05 | 1.16 ± 0.14 | 2.00 ± 0.13 |

**Table 2.2:** Elemental analysis obtained from EDX analysis for $CuInSe_2$ nanocrystals prepared from various synthesis methods.

The other important factor that seems to affect device performance is the type of ligand attached to the nanocrystals. There are three ligands involved in the four reactions discussed: oleylamine, TBP, and DPP. In order to know if these molecules are acting as a capping ligand for the nanocrystals, we used proton nuclear magnetic resonance ($^1$H

NMR). NMR is a useful tool to distinguish a bound ligand from an unbound ligand.[12] The restricted rotation of the molecules attached to the nanocrystals causes the peaks for bound ligands to be much broader than the peaks of free molecules.[13] Thus, broader peaks on the NMR spectra correspond to the hydrogens of bound ligands, and some of the peaks are so broad that they are unidentifiable from the rest of the spectrum. Of the hydrogens attached to the bound ligand, these broad peaks correspond to those closest to the nanocrystal surface. Another observation of the NMR spectra is a downfield shift of the broad peaks caused by an increase in the electropositivity of protons, which is induced by attachment of the ligand to the nanocrystal surface.

The effect of ligands on the electronic properties of nanocrystals is a well-known factor on PCE. Drastic improvements in device performance have been achieved by choosing the right kind of ligand.[14–19] The NMR spectra of the nanocrystals synthesized by the four different synthesis methods is shown in figure 2.4a, and the signature matches with that of neat oleylamine. The non-overlapping peaks will be utilized to distinguish one ligand from the other in systems employing multiple ligands. Figure 2.4c, shows the magnified spectra from 8 to 7.5 ppm, where the characteristic DPP peaks can be observed for the DPP:Se injection method and the Hybrid reaction method. The peaks are broadened and shifted compared to 'free' DPP molecules (figure 2.4c), indicating its attachment to the nanocrystal surface. Most peaks from oleylamine and TBP overlap, the most distinguishable peak corresponding to TBP is circled in figure 2.4d.

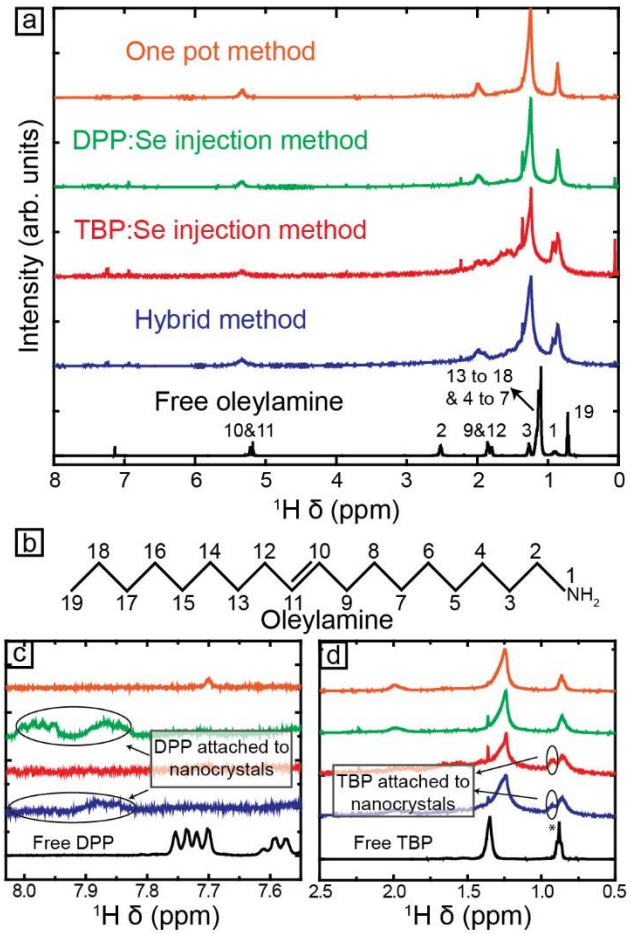


**Figure 2.4:** (a) $^{1}$H NMR spectra of oleylamine and $CuInSe_2$ nanocrystals synthesized from various routes. (b) Oleylamine molecule with numbered atoms to indicate the corresponding proton peaks in (a). (c, d) Magnified spectra of (a) from 7.6 to 8 ppm with unbound DPP spectra shown in black and from 0.5 to 2.5 ppm with unbound TBP spectra in black, respectively. The peak marked with * in the TBP spectra is distinguishable from the oleylamine peaks.

Hence, $^{1}$H NMR data proves that all the ligands used in each reaction are bounded to the nanocrystal surface. Based on the device PCE, we observe that the TBP ligand is crucial in increasing the device performance. Both the TBP:Se injection method particles and the hybrid method particles (containing TBP) show significantly higher PCEs in

devices than the other two reactions, in which TBP does not act as a ligand. The partial replacement of long chain oleylamine molecules with shorter chain TBP molecules allows for easier charge transfer between nanocrystals. Better charge transfer improves short circuit current, which improves PCE. Similarly, when DPP molecules partially replace the oleylamine molecules in the DPP:Se injection method, the PCE increase is less than the increase when TBP is acting as a ligand.

## 2.4 CONCLUSIONS

The Hybrid reaction combines the reaction yield benefits from the DPP:Se injection method and the PCE gains from the TBP:Se injection method. As shown in figure 1, the Hybrid reaction devices show a 160 % increase in average PCE from the DPP:Se injection particles, and a 32 % increase in PCE from the TBP:Se injection nanocrystals. Additionally, the reaction yield is increased by 9-fold compared to the TBP:Se injection reaction. Thus, we conclude that the hybrid reaction, developed herein, is the most promising method for $CuInSe_2$ nanocrystal solar cells. To further improve the PCE of devices, fabricated from $CuInSe_2$ nanocrystals that are synthesized from the Hybrid reaction, we baked the devices at 200 ºC for 10 minutes in vacuum. The JV curve and EQE of the best performing device, fabricated from the Hybrid reaction nanocrystals, is shown in figure 4. We obtained an efficiency of 3.04 %, which is similar to record efficiencies obtained for low temperature processed ($\leq 200$ °C) nanocrystal $CuInSe_2$ devices previously published in literature, but with an added advantage of higher yields than other methods.[6]

## 2.5 REFERENCES


(1) Panthani, M. G.; Akhavan, V.; Goodfellow, B.; Schmidtke, J. P.; Dunn, L.; Dodabalapur, A.; Barbara, P. F.; Korgel, B. A. Synthesis of $CuInS_2$, $CuInSe_2$, and $Cu(In_xGa_{1-x})Se_2$ (CIGS) Nanocrystal "Inks" for Printable Photovoltaics. *J. Am. Chem. Soc.* **2008**, *130*, 16770–16777.

(2) Koo, B.; Patel, R. N.; Korgel, B. A. Synthesis of $CuInSe_2$ Nanocrystals with Trigonal Pyramidal Shape. *J. Am. Chem. Soc.* **2009**, *131*, 3134–3135.

(3) Tang, J.; Hinds, S.; Kelley, S. O.; Sargent, E. H. Synthesis of Colloidal $CuGaSe_2$, $CuInSe_2$, and $Cu(InGa)Se_2$ Nanoparticles. *Chem. Mater.* **2008**, *20*, 6906–6910.

(4) Zhong, H.; Wang, Z.; Bovero, E.; Lu, Z.; van Veggel, F. C. J. M.; Scholes, G. D. Colloidal CuInSe2 Nanocrystals in the Quantum Confinement Regime: Synthesis, Optical Properties, and Electroluminescence. *J. Phys. Chem. C* **2011**, *115*, 12396–12402.

(5) Guo, Q.; Kim, S. J.; Kar, M.; Shafarman, W. N.; Birkmire, R. W.; Stach, E. A.; Agrawal, R.; Hillhouse, H. W. Development of $CuInSe_2$ Nanocrystal and Nanoring Inks for Low-Cost Solar Cells. *Nano Lett.* **2008**, *8*, 2982–2987.

(6) Akhavan, V. A.; Panthani, M. G.; Goodfellow, B. W.; Reid, D. K.; Korgel, B. A. Thickness-Limited Performance of $CuInSe_2$ Nanocrystal Photovoltaic Devices. *Opt. Express* **2010**, *18*, A411.

(7) Panthani, M. G.; Stolle, C. J.; Reid, D. K.; Rhee, D. J.; Harvey, T. B.; Akhavan, V. A.; Yu, Y.; Korgel, B. A. $CuInSe_2$ Quantum Dot Solar Cells with High Open-Circuit Voltage. *J. Phys. Chem. Lett.* **2013**, *4*, 2030–2034.

(8) Stolle, C. J.; Panthani, M. G.; Harvey, T. B.; Akhavan, V. A.; Korgel, B. A. Comparison of the Photovoltaic Response of Oleylamine and Inorganic Ligand-Capped $CuInSe_2$ Nanocrystals. *ACS Appl. Mater. Interfaces* **2012**, *4*, 2757–2761.

(9) Evans, C. M.; Evans, M. E.; Krauss, T. D. Mysteries of TOPSe Revealed: Insights into Quantum Dot Nucleation. *J. Am. Chem. Soc.* **2010**, *132*, 10973–10975.

(10) Contreras, M. A.; Romero, M. J.; Noufi, R. Characterization of $Cu(In,Ga)Se_2$ Materials Used in Record Performance Solar Cells. *Thin Solid Films* **2006**, *511*, 51–54.

(11) Jackson, P.; Hariskos, D.; Lotter, E.; Paetel, S.; Wuerz, R.; Menner, R.; Wischmann, W.; Powalla, M. New World Record Efficiency for $Cu(In,Ga)Se_2$ Thin-Film Solar Cells beyond 20%. *Prog. Photovolt. Res. Appl.* **2011**, *19*, 894–897.

(12) Hens, Z.; Martins, J. C. A Solution NMR Toolbox for Characterizing the Surface Chemistry of Colloidal Nanocrystals. *Chem. Mater.* **2013**, *25*, 1211–1221.

(13) Hens, Z.; Moreels, I.; Martins, J. C. In Situ 1H NMR Study on the Trioctylphosphine Oxide Capping of Colloidal InP Nanocrystals. *ChemPhysChem* **2005**, *6*, 2578–2584.

(14) Barkhouse, D. A. R.; Pattantyus-Abraham, A. G.; Levina, L.; Sargent, E. H. Thiols Passivate Recombination Centers in Colloidal Quantum Dots Leading to Enhanced Photovoltaic Device Efficiency. *ACS Nano* **2008**, *2*, 2356–2362.

(15) Koleilat, G. I.; Levina, L.; Shukla, H.; Myrskog, S. H.; Hinds, S.; Pattantyus-Abraham, A. G.; Sargent, E. H. Efficient, Stable Infrared Photovoltaics Based on Solution-Cast Colloidal Quantum Dots. *ACS Nano* **2008**, *2*, 833–840.

(16) Sarasqueta, G.; Choudhury, K. R.; So, F. Effect of Solvent Treatment on Solution-Processed Colloidal PbSe Nanocrystal Infrared Photodetectors. *Chem. Mater.* **2010**, *22*, 3496–3501.

(17) Guyot-Sionnest, P.; Wang, C. Fast Voltammetric and Electrochromic Response of Semiconductor Nanocrystal Thin Films. *J. Phys. Chem. B* **2003**, *107*, 7355–7359.

(18) Talgorn, E.; Moysidou, E.; Abellon, R. D.; Savenije, T. J.; Goossens, A.; Houtepen, A. J.; Siebbeles, L. D. A. Highly Photoconductive CdSe Quantum-Dot Films: Influence of Capping Molecules and Film Preparation Procedure. *J. Phys. Chem. C* **2010**, *114*, 3441–3447.

(19) Fafarman, A. T.; Koh, W.; Diroll, B. T.; Kim, D. K.; Ko, D.-K.; Oh, S. J.; Ye, X.; Doan-Nguyen, V.; Crump, M. R.; Reifsnyder, D. C.; *et al.* Thiocyanate-Capped Nanocrystal Colloids: Vibrational Reporter of Surface Chemistry and Solution-Based Route to Enhanced Coupling in Nanocrystal Solids. *J. Am. Chem. Soc.* **2011**, *133*, 15753–15761.

# Chapter 3: Ligand Engineering of $CuInSe_2$ Nanocrystals for Improvement in Device Performance

## 3.1 INTRODUCTION

The common way to improve nanocrystal PV efficiency is ligand engineering: replacing longer chain ligands with smaller chain ligands or introducing ligands that better passivate nanocrystal surfaces.[1,2] This technique led to huge improvements in device efficiencies in various nanocrystal systems. For example, first reports employing Pb(S,Se) nanocrystals as the absorber material achieved efficiencies as low as 3%.[3] By choosing suitable ligands, the Pb(S,Se) nanocrystal solar cells were able to achieve efficiencies as high as 10.6%.[4] The improvement in device efficiency with ligand exchange can be due to the increase in the short circuit current resulting from the replacement of insulating long chain organic ligands with less insulating shorter molecules or by an increase in open circuit voltage resulting from better passivation or by band engineering.[2,5–10] Ligand engineering for $CuInSe_2$ nanocrystals is still in its infancy. To our knowledge, only two reports have been published for ligand exchanged $CuInSe_2$ nanocrystal solar cells.[11,12] However, their ligand engineering did not increase their device efficiency above 3.1 (the reported maximum efficiency for $CuInSe_2$ nanocrystal solar cells fabricated under mild processing conditions).[13] Here we develop a ligand exchange procedure for $CuInSe_2$ nanocrystals using ammonium sulfide to increase the efficiency beyond 3.1%. Ammonium sulfide was chosen as the chemical to facilitate the ligand exchange of long chain oleylamine ligands with shorter sulfide ions. Such use of ammonium sulfide to replace

insulating organic ligands with smaller ions in order to achieve performance gains has been exploited before in $Cu_2ZnSnS_4$ nanocrystals.[14]

## 3.2 EXPERIMENTAL DETAILS

### 3.2.1 Materials

Chemicals: Copper(I) chloride (CuCl, 99.99%), elemental Selenium (Se, 99.99%), ammonium sulfide (20% in water), cadmium sulfate (CdSO4, 99.99%), thiourea (99%), formamide (99.5%), oleylamine (OLA; >70%), tributylphosphine (TBP; 97%), diphenylphosphine (DPP; 98%), and anhydrous toluene (99.8%) were obtained from Aldrich; indium (III) chloride ($InCl_3$, 99.99%) was obtained from Strem Chemical; toluene, ethanol, chloroform-d and ammonium hydroxide (18 M NH4OH) were obtained from Fisher Scientific. The oleylamine stock solution is prepared by degassing it at 1100°C under vacuum overnight and stored in a nitrogen filled glovebox for future use. CuCl and $InCl_3$ are stored in the glovebox to prevent degradation. All other chemicals are used as received.

### 3.2.2 $CuInSe_2$ Nanocrystal Synthesis

$CuInSe_2$ nanocrystals have been prepared by methods previously described by Voggu et. al. In a typical synthesis 5 mmol of CuCl, 5 mmol of $InCl_3$, 1.5 ml of DPP and 50 ml of OLA are heated in a 3-neck reaction flask at 110 ºC under vacuum, for 30 minutes, followed by heating at 110 ºC, for 10 minutes, under nitrogen atmosphere. The flask and its contents are then heated to 180 ºC where a 10 mmol of Se in 10 ml of TBP solution is injected rapidly into the reaction mixture. This mixture is then heated to 240 ºC for 10

minutes. The reaction mixture is then allowed to cool to room temperature while maintaining the nitrogen atmosphere. The nanocrystals were then separated by adding ethanol and centrifuging at 4500 rpm for 10 minutes. This washing process is repeated one more time. The nanocrystals are dispersed in anhydrous toluene and stored at a concentration of 100 mg/mL in a nitrogen filled glove box.

### 3.2.3 Solid-State Ligand Exchange Procedure with Ammonium Sulfide

A layer by layer solid state ligand exchange has been employed. A 20 mg/mL of $CuInSe_2$ nanocrystal dispersion is spin coated at 600 rpm for 3 seconds followed by 2000 rpm for 40 seconds. This produces a 30-nm thick $CuInSe_2$ nanocrystal layer. This layer is then treated with a solution of ammonium sulfide (20 wt % in water) in methanol. 70 µL of ammonium sulfide is added to 2 mL of methanol solution and mixed well. This solution is drop casted onto the $CuInSe_2$ nanocrystal film and is left to react for 15 seconds. The layer is then rinsed off with methanol. The nanocrystal layer is not soluble in toluene anymore, indicating the ligand exchange with ammonium sulfide. This makes it possible to spin coat another layer of $CuInSe_2$ nanocrystals on top of this layer. The process is repeated a few times to achieve the desired thickness. The number of layers of $CuInSe_2$ to be spin coated is optimized for maximum PCE, and we observe that four coats give the best performance. A final layer of $CuInSe_2$ nanocrystals is spin coated to fill in the pores that were caused by removal of the long chain oleylamine molecule.

### 3.2.4 Solution Phase Ligand Exchange Procedure with Ammonium Sulfide

A 5 mL solution of 10 mg/mL $CuInSe_2$ nanocrystals, that were prepared through the Hybrid synthesis, dispersed in toluene is mixed with a solution containing 0.5 mL of ammonium sulfide (20 wt % in $H_2O$) and 4.5 mL of formamide inside a nitrogen filled glovebox. This mixture is allowed to stir for 12 hours in the glovebox. The oleylamine capped $CuInSe_2$ nanocrystals dispersed in the non-polar solvent toluene are transferred into the polar formamide solvent. The two solvents are phase separated with the higher density formamide being the bottom phase. The nanocrystal-formamide dispersion is then separated and centrifuged at 6000 rpm for 3 minutes. After stirring overnight, fresh toluene is added and the mixture is vigorously shaken to remove the remaining oleylamine ligand. This process is repeated one more time and 10 mL of acetonitrile is added to the nanocrystal dispersion in formamide and centrifuged at 6000 rpm for 3 minutes. A yellow colored supernatant is separated, which indicates the presence of ammonium sulfide, and is discarded. The precipitate is redispersed in methanol and rotovaped. Dried nanocrystals are redispersed in methanol and stored at a concentration of 100 mg/mL. The polar and non-polar solvent system is chosen in such a way that they are immiscible with each other. Toluene and formamide are immiscible.

### 3.2.5 PV Device Fabrication and Testing

A 5-nm chrome (99.999%, Lesker) layer followed by a 60-nm layer of gold (99.95%, Lesker) are deposited by thermal evaporation onto a polished glass slide. In a non-ligand exchanged device, $CuInSe_2$ nanocrystal layer is deposited by spin coating as

follows. 100 mg/mL of $CuInSe_2$ nanocrystal solution is filtered through a 0.45 μm pore size filter and then diluted to 50 mg/mL by adding toluene. This dispersion is drop casted onto the gold coated glass substrate and spun at 600 rpm for 3 seconds followed by 2000 rpm for 40 seconds to deposit a $CuInSe_2$ nanocrystal layer that is approximately 200 nm thick. For devices incorporating ligand exchanged $CuInSe_2$ nanocrystal layer the procedure is described in section 3.2.3. CdS was deposited by chemical surface deposition method.[15] 0.7 mL of a CdS precursor solution which is a mixture of 1.25 mL of 15 mM CdSO4, 2.2 mL of 1.5 M thiourea, and 2.8 mL of 18 M NH4OH in water in taken in a 1 mL pipette and was drop casted onto a pre-heated $CuInSe_2$ and gold coated glass substrate maintained at 90 ºC and covered with an inverted crystallization dish. The CdS precursor solution is left on the substrate for 2 minutes and a CdS layer is deposited. The excess CdS precursor solution is rinsed off with a jet of DI water. The substrates are then dried by blowing compressed nitrogen. The next two layers are i-ZnO and ITO. They were deposited by Radio Frequency (RF) sputtering using ZnO (99.9%) and ITO (99.99 % $In_2O_3$:$SnO_2$ 9:1) targets in Argon atmosphere. ZnO and ITO are deposited selectively onto 4 or 8 rectangular regions of area ranging from 0.08 $cm^2$ to 0.13 $cm^2$ using shadow masking. Silver paint is applied to the top ITO contact and the bottom gold contact for PV testing. Baking of the devices is done in a rapid thermal processing (RTP) furnace where the temperature is ramped at 1.5 ºC/minute to reach the required temperature under air/argon/vacuum.

Keithley 2400 general purpose source meter was used to perform the current-voltage measurements under an A.M1.5 solar simulation. The light source is calibrated using a NIST- calibrated Si photodiode (Hamamatsu, S1787-08). External Quantum

Efficiency measurements were made using a monochromatic light generated from a commercial monochromator (Newport Cornerstone 260 1/4M), chopped at 213 Hz, and focused to a spot size of 1 mm in diameter on the active region of the device. The monochromatic light is calibrated using silicon (Hamamatsu) and germanium (Judson) photodiodes. For these measurements, the monochromatic light is swept across a wavelength from 320 nm to 1330 nm with a step size increment of 10 nm using a lock-in-amplifier (Stanford Research Systems, model SR830).

### 3.2.6 Characterization

Transmission electron microscopy (TEM) was performed on a FEI Tecnai G2 Spirit BioTwin microscopy operated at 80 kV. Scanning electron microscopy (SEM) was done on a Zeiss Supra 40 VP SEM operated at 5 keV accelerating voltage. X-ray diffraction (XRD) was performed on a Rigaku R-axis Spider diffractometer with an image plate detector and using graphite monochromatized Cu Kα ($\lambda = 1.5418$ Å) radiation operated at 40 kV and 40 mA. For XRD measurements, the nanocrystals are dried onto a glass substrate and the nanocrystal powder is scraped off onto a 0.5 mm nylon loop, which is rotated at 1º per second for 10 minutes while X-rays are being shined. Energy Dispersive Spectroscopy (EDS) was done on a Hitachi S5500 SEM operated at 30 kV.

## 3.3 RESULTS AND DISCUSSION

Herein, we report a PCE of 3.5 % using a solid-state ligand exchange with ammonium sulfide on $CuInSe_2$ nanocrystals prepared by the Hybrid method that is described in chapter 2. Baking to remove the solvent remains from ligand exchange is very

essential in improvement of device performance as shown in figure 3.1. All these devices have been baked in an RTP furnace at 200 ºC under vacuum.

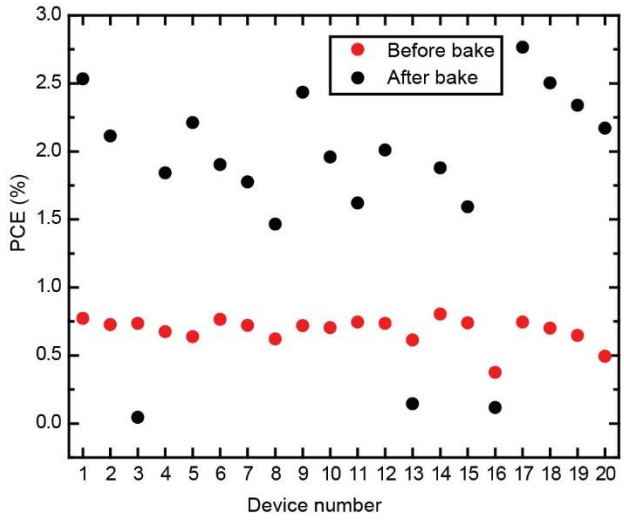


**Figure 3.1:** PCE for solar cells employing ligand exchanged $CuInSe_2$ nanocrystals before (●) and after (● ) baking at 200 ºC in vacuum.

### 3.3.1 Optimization of Solid State Ammonium Sulfide Ligand Exchange for Devices

The data supporting various optimization experiments is provided in figures 3.2 and 3.3. Figure 3.2 shows the device characteristics of ligand exchanged $CuInSe_2$ nanocrystal solar cells with top most $CuInSe_2$ nanocrystal coating to be untreated with ammonium sulfide versus it being treated with ammonium sulfide. There is an increase in average PCE from 0.6% to 2.44% by having an additional non-ligand exchanged $CuInSe_2$ nanocrystal coat. We attribute this increase in PCE, on using untreated $CuInSe_2$ nanocrystal top layer, is due to the filling up of void spaces caused by removal of long chain oleylamine molecules during ammonium sulfide treatment.

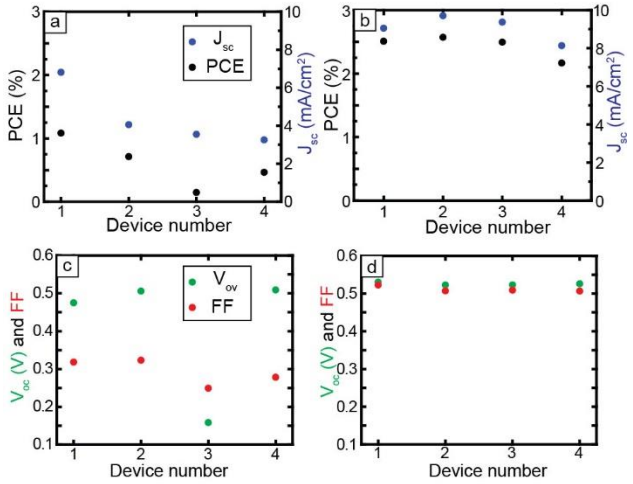


**Figure 3.2:** Device characteristics for four $CuInSe_2$ nanocrystal solar cells with the top-most $CuInSe_2$ nanocrystal layer (a and c) treated with ammonium sulfide and (b and d) untreated with ammonium sulfide.

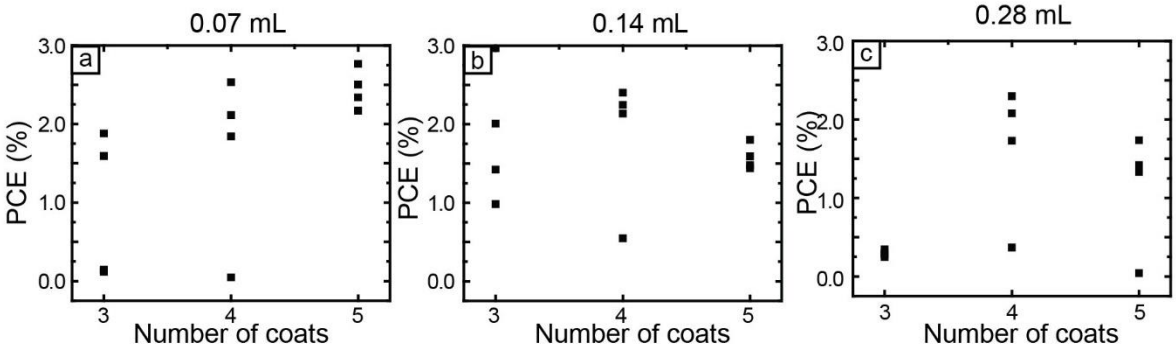


**Figure 3.3:** Power conversion efficiency as a function of $CuInSe_2$ nanocrystal coats at various concentrations of ammonium sulfide used for ligand exchange. Plots (a-c) show the PCE at 3,4 and 5 coats of $CuInSe_2$ nanocrystal layer after treatment with (a)70 µL, (b)140 µL and (c) 280 µL of ammonium sulfide in 2 mL of methanol solution. There is an additional $CuInSe_2$ coat on each of these devices that is not treated with ammonium sulfide.

The JV characteristics for 4 devices made with $CuInSe_2$ nanocrystals (Hybrid method) with and without ammonium sulfide treatment with these optimized fabrication

conditions are shown in figure 3.4. The average device performance for devices with $(NH_4)_2S$ treatment (2.68 %) is 11 % higher than the average PCE of devices fabricated without any $(NH_4)_2S$ treatment (2.41%). The JV characteristics of the best device and its external quantum efficiency (EQE) are shown in figure 3.5. The short circuit current calculated from the EQE equals 11.42 mA/cm$^2$, which is within 20 % of the short circuit current that was measured from JV testing. We predict that the slight reduction in open circuit voltage ($V_{oc}$) from 0.52 V to 0.49 V is due to a decreased passivation of the nanocrystal surface after ammonium sulfide treatment.

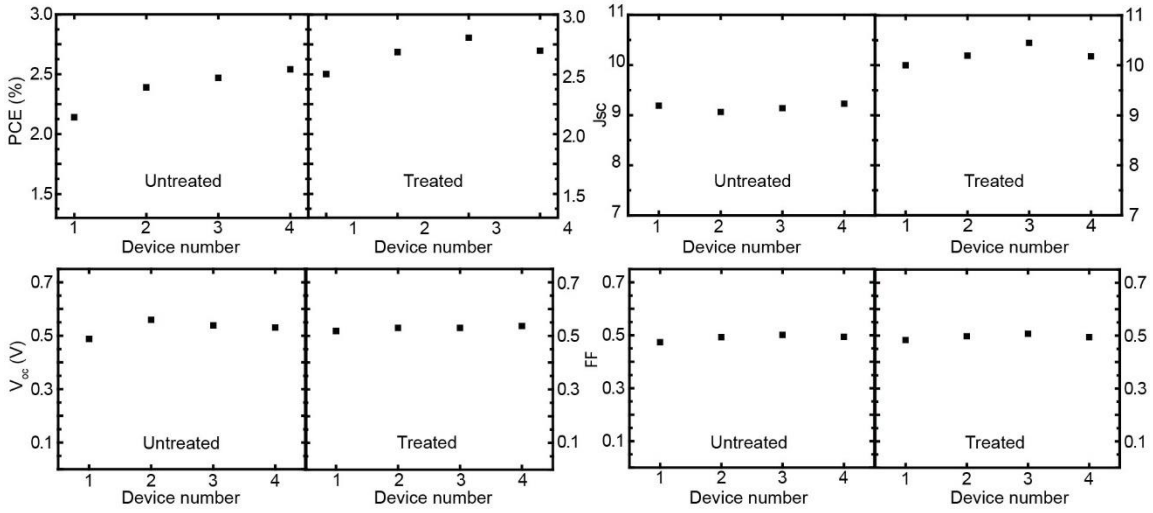


**Figure 3.4:** Device characteristics for $CuInSe_2$ nanocrystal solar cells with and without solid state ligand exchange with ammonium sulfide measured under AM1.5G illumination. The nanocrystals used are synthesized from the Hybrid method. An increase in $J_{sc}$, leading to an increase in PCE can be observed after the ammonium sulfide treatment, while $V_{oc}$ and FF remain the same.

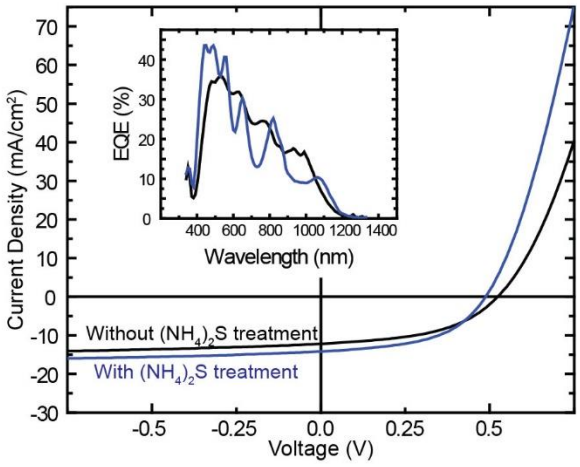


**Figure 3.5:** JV curves of best performing solar cells utilizing $CuInSe_2$ nanocrystals synthesized from Hybrid method with (blue) and without (black) ammonium sulfide treatment. The device with ammonium sulfide treatment has a PCE of 3.49%, short-circuit current density ($J_{sc}$) of 14.16 mA/cm$^2$, open-circuit voltage ($V_{oc}$) of 0.49 V and fill factor (FF) of 0.51. The device without ammonium sulfide treatment has a PCE of 3.04%, $J_{sc}$ of 12.18 mA/cm$^2$, $V_{oc}$ of 0.52 V and FF of 0.48 V. The JV characteristics are measured under A.M. 1.5G illumination. Inset shows EQE for these devices measured under a white light bias of 50 mW/cm$^2$. The short circuit current calculated from EQE for $(NH_4)_2S$ treated device is 11.62 mA/cm$^2$ and for untreated device is 9.89 mA/cm$^2$.

### 3.3.2 NMR Spectroscopy Study on Addition of $(NH_4)_2S$ to $CuInSe_2$ Nanocrystals

In this study, we observed that ammonium sulfide displaces the ligands oleylamine and TBP from the nanocrystal surface. This displacement reduces the barrier to charge transfer between nanocrystals and causes an increase in short circuit current, which directly increases the PCE as can be seen in figure 3.4. The removal of oleylamine and TBP ligands from nanocrystal surface can be observed in the NMR spectra shown in figure 3.6. When 6 µg of $(NH_4)_2S$ aqueous solution is added in 100 mg of $CuInSe_2$ nanocrystals with d-chloroform as the solvent, we noticed strong TBP signal in the NMR proving that TBP has

been dislodged by $(NH_4)_2S$ as shown in figure 3.6b. When even more $(NH_4)_2S$ (40 µg) is added, OLA is also dislodged. As seen in the figure 3.6c, the characteristic peak corresponding to the hydrogen attached to the double bonded carbon, at 5.35 ppm, appears as a sharp peak. The peak corresponding to the hydrogen attached to the carbon next to the amine group, at 2.7 ppm, that is otherwise absent due to strong restricted motion, also appears as sharp peaks. When 40 µg of $(NH_4)_2S$ is added the nanocrystals precipitate out of solution and NMR is conducted on the supernatant (that contains dislodged ligands) which is collected by centrifugation.

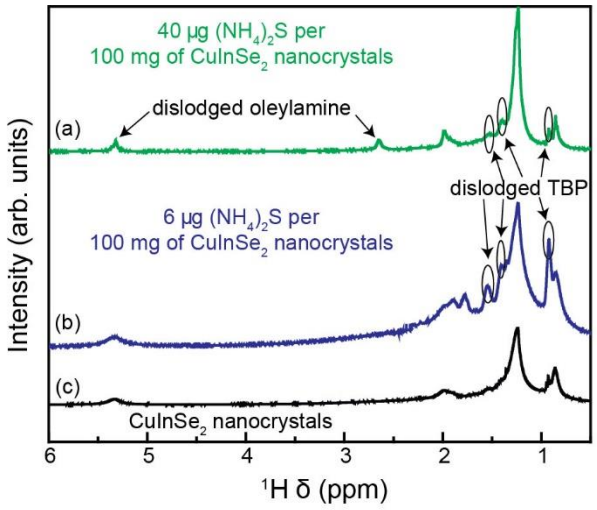


**Figure 3.6:** $^1H$ NMR of (a &b) $CuInSe_2$ nanocrystals dispersed in d-chloroform after addition of 40 µg and 6 µg of $(NH_4)_2S$ to 100 mg of nanocrystals, respectively and (c) $^1H$ NMR of $CuInSe_2$ nanocrystals. The nanocrystals are synthesized by Hybrid method.

### 3.3.3 FTIR and TGA on Ammonium Sulfide Treated $CuInSe_2$ Nanocrystals

In order to further confirm that ammonium sulfide removes the long chain oleylamine ligands, Fourier Transform Infrared Spectroscopy (FTIR) and TGA can be

performed on ammonium sulfide treated nanocrystals, but FTIR requires that samples be prepared on smooth, polished silicon substrates to maximize signal to noise ratio. However, the poor adherence of $CuInSe_2$ nanocrystals to the silicon wafer caused the $CuInSe_2$ nanocrystal layer to wash away during the methanol rinse step of the $(NH_4)_2S$ treatment and hence we could not perform FTIR on solid state ligand exchanged nanocrystals. Hence, a solution-phase ligand exchange was employed in place of a solid-state ligand exchange. In order to readily extract the exchanged nanocrystals, we used two immiscible solvents, a polar solvent that dissolved the ammonium sulfide, and a non-polar solvent that dispersed the nanocrystals. The nanocrystals that underwent a ligand exchange transferred from the nonpolar to polar phase. Thus, we extracted the polar phase containing the ligand-exchanged $CuInSe_2$ nanocrystals. The nonpolar and polar solvent system that we studied was toluene and formamide, and the detailed procedure for this ligand exchange is discussed in section 3.2.3. TEM image of the nanocrystals before and after the ligand exchange is also provided in figure 3.7. It can be seen from these TEM images that the nanocrystals are more prone to agglomeration because of shorter ligands compared to oleylamine.

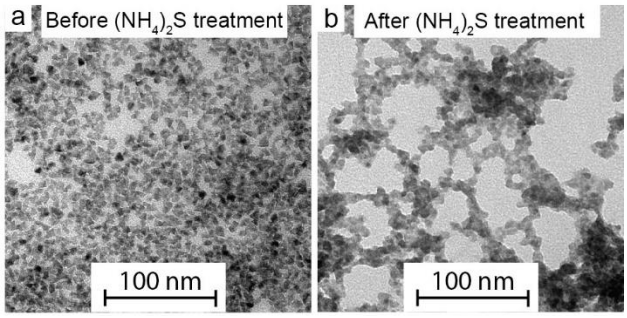


**Figure 3.7:** TEM images of $CuInSe_2$ nanocrystals (a) before and (b) after solution phase ligand exchange with ammonium sulfide.

Figure 3.8 shows the FTIR of $CuInSe_2$ nanocrystals before and after treatment with ammonium sulfide. The samples were prepared by drop casting 100 µL of 100 mg/mL $CuInSe_2$ nanocrystal solution in a suitable solvent onto a double-sided, polished, un-doped silicon substrate. The bond stretches that correspond to oleylamine disappeared from the ammonium sulfide-treated sample, which indicated successful removal of oleylamine from the nanocrystals. The FTIR signature for the ligand-exchanged particles matches the FTIR signature of formamide, indicating the presence of residual formamide.

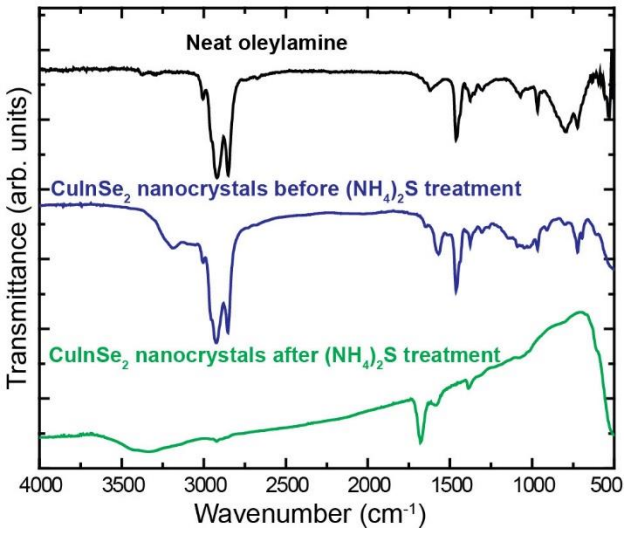


**Figure 3.8:** FTIR spectra of neat oleylamine, $CuInSe_2$ nanocrystals before and after treatment with ammonium sulfide.

The TGA results in figure 3.9 show that the sample had a low boiling point component, supporting the FTIR data that formamide remained in the nanocrystal dispersion. To confirm that the observed weight loss was formamide, TGA (figure 3.10) was conducted on pure formamide, and we observed a similar weight loss trend for both formamide and the ligand-exchanged $CuInSe_2$ nanocrystals. Thus, we conclude that formamide remained in the ammonium sulfide-exchanged particles.

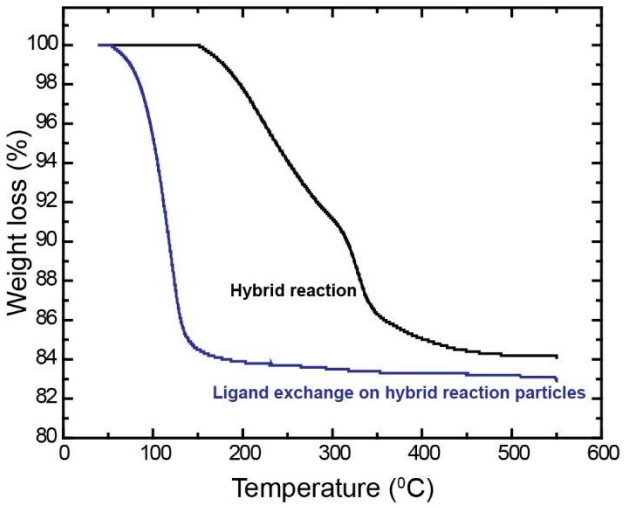


**Figure 3.9:** TGA of $CuInSe_2$ nanocrystals prepared from the Hybrid reaction before and after ligand exchange treatment with ammonium sulfide.

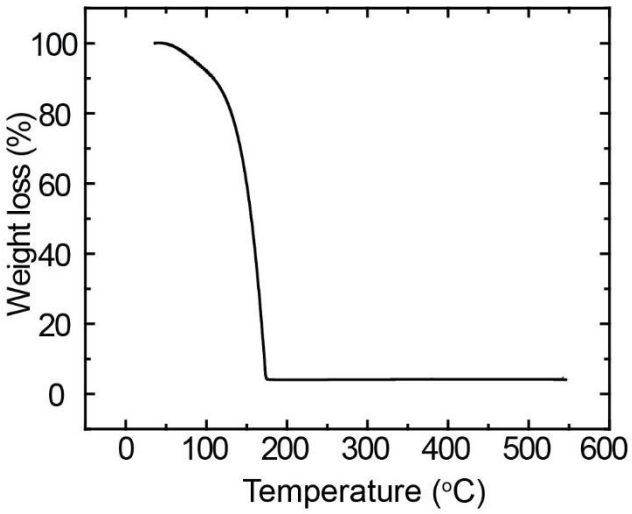


**Figure 3.10:** TGA of pure formamide

To conclude that the formamide remaining in the ligand-exchanged particles was residual and not acting as a capping ligand, a solution phase exchange was performed in the absence of ammonium sulfide. If formamide was the capping ligand, the nanocrystals

would have transferred to the polar formamide phase. However, no distinguishable phase transfer was observed. We were able to extract the nanocrystals by centrifugation instead, but they did not disperse in polar or nonpolar solvents, which indicated that neither formamide nor any other species was acting as a capping ligand. These results allow us to conclude that ammonium sulfide was indeed necessary for exchanging the native oleylamine ligands.

### 3.3.4 Elemental Analysis and X-ray Diffraction Studies on $(NH_4)_2S$ Treated $CuInSe_2$ Nanocrystals

For elemental analysis, EDX has been performed on ammonium sulfide treated nanocrystals. The data shown in table 3.1 is the average taken over three different spots on a sample. The nanocrystals were observed to be copper poor and indium rich. The EDX data has been normalized to indium to compare stoichiometric values for copper, selenium and sulfur. It can be observed that the copper and indium remain the same before and after treatment with ammonium sulfide but, a slight decrease in the amount of selenium is noted. We attribute this decrease to replacement of some of the selenium atoms with sulfur. XRD (figure 3.12) shows no peak shift due to incorporation of sulfur and hence we predict that sulfur is being adsorbed on the surface rather than being incorporated into the crystal lattice. These sulfide ions on the surface act as capping ligands and are responsible for nanocrystal dispersibility in polar solvents such as methanol and formamide. Such role of sulfide ions as the capping ligands by adsorption on the surface has been previously observed in CdSe nanocrystals.[16]

| element | untreated nanocrystals | treated with $(NH_4)_2S$ in formamide & toluene |
|---|---|---|
| **Cu** | 0.67 ± 0.04 | 0.65 ± 0.04 |
| **In** | 1.00 ± 0.11 | 1.00 ± 0.12 |
| **Se** | 1.69 ± 0.11 | 1.52 ± 0.10 |
| **S** | 0 | 0.24 ± 0.01 |

**Table 3.1:** Elemental analysis for $CuInSe_2$ nanocrystals before and after treatment with ammonium sulfide indicating the presence of sulfur after treatment.

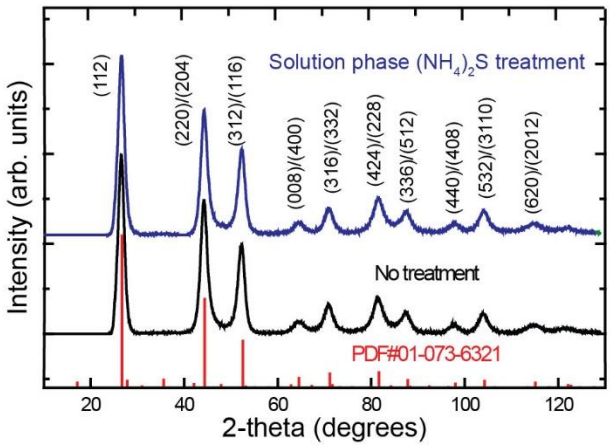


**Figure 3.11:** XRD pattern for $CuInSe_2$ nanocrystals synthesized by hybrid method before (black) and after treatment with $(NH_4)_2S$ (blue). The red reference lines correspond to the chalcopyrite $CuInSe_2$ (PDF #01-073-3621).

## 3.4 CONCLUSIONS

We increased the PCE to 3.5%, the highest ever achieved for low temperature processed $CuInSe_2$ nanocrystal solar cells, by employing a ligand exchange with ammonium sulfide that replaces long chain oleylamine molecules with sulfide ions.

## 3.5 REFERENCES

(1) Tang, J.; Kemp, K. W.; Hoogland, S.; Jeong, K. S.; Liu, H.; Levina, L.; Furukawa, M.; Wang, X.; Debnath, R.; Cha, D.; *et al.* Colloidal-Quantum-Dot Photovoltaics Using Atomic-Ligand Passivation. *Nat. Mater.* **2011**, *10*, 765–771.

(2) Chuang, C.-H. M.; Brown, P. R.; Bulović, V.; Bawendi, M. G. Improved Performance and Stability in Quantum Dot Solar Cells through Band Alignment Engineering. *Nat. Mater.* **2014**, *13*, 796–801.

(3) Ma, W.; Luther, J. M.; Zheng, H.; Wu, Y.; Alivisatos, A. P. Photovoltaic Devices Employing Ternary PbSxSe1-X Nanocrystals. *Nano Lett.* **2009**, *9*, 1699–1703.

(4) Lan, X.; Voznyy, O.; García de Arquer, F. P.; Liu, M.; Xu, J.; Proppe, A. H.; Walters, G.; Fan, F.; Tan, H.; Liu, M.; *et al.* 10.6% Certified Colloidal Quantum Dot Solar Cells via Solvent-Polarity-Engineered Halide Passivation. *Nano Lett.* **2016**, *16*, 4630–4634.

(5) Barkhouse, D. A. R.; Pattantyus-Abraham, A. G.; Levina, L.; Sargent, E. H. Thiols Passivate Recombination Centers in Colloidal Quantum Dots Leading to Enhanced Photovoltaic Device Efficiency. *ACS Nano* **2008**, *2*, 2356–2362.

(6) Koleilat, G. I.; Levina, L.; Shukla, H.; Myrskog, S. H.; Hinds, S.; Pattantyus-Abraham, A. G.; Sargent, E. H. Efficient, Stable Infrared Photovoltaics Based on Solution-Cast Colloidal Quantum Dots. *ACS Nano* **2008**, *2*, 833–840.

(7) Sarasqueta, G.; Choudhury, K. R.; So, F. Effect of Solvent Treatment on Solution-Processed Colloidal PbSe Nanocrystal Infrared Photodetectors. *Chem. Mater.* **2010**, *22*, 3496–3501.

(8) Guyot-Sionnest, P.; Wang, C. Fast Voltammetric and Electrochromic Response of Semiconductor Nanocrystal Thin Films. *J. Phys. Chem. B* **2003**, *107*, 7355–7359.

(9) Talgorn, E.; Moysidou, E.; Abellon, R. D.; Savenije, T. J.; Goossens, A.; Houtepen, A. J.; Siebbeles, L. D. A. Highly Photoconductive CdSe Quantum-Dot Films: Influence of Capping Molecules and Film Preparation Procedure. *J. Phys. Chem. C* **2010**, *114*, 3441–3447.

(10) Fafarman, A. T.; Koh, W.; Diroll, B. T.; Kim, D. K.; Ko, D.-K.; Oh, S. J.; Ye, X.; Doan-Nguyen, V.; Crump, M. R.; Reifsnyder, D. C.; *et al.* Thiocyanate-Capped Nanocrystal Colloids: Vibrational Reporter of Surface Chemistry and Solution-Based Route to Enhanced Coupling in Nanocrystal Solids. *J. Am. Chem. Soc.* **2011**, *133*, 15753–15761.

(11) Pernik, D. R.; Gutierrez, M.; Thomas, C.; Voggu, V. R.; Yu, Y.; van Embden, J.; Topping, A. J.; Jasieniak, J. J.; Vanden Bout, D. A.; Lewandowski, R.; *et al.* Plastic Microgroove Solar Cells Using CuInSe2 Nanocrystals. *ACS Energy Lett.* **2016**, *1*, 1021–1027.

(12) Stolle, C. J.; Panthani, M. G.; Harvey, T. B.; Akhavan, V. A.; Korgel, B. A. Comparison of the Photovoltaic Response of Oleylamine and Inorganic Ligand-Capped CuInSe2 Nanocrystals. *ACS Appl. Mater. Interfaces* **2012**, *4*, 2757–2761.

(13) Akhavan, V. A.; Panthani, M. G.; Goodfellow, B. W.; Reid, D. K.; Korgel, B. A. Thickness-Limited Performance of $CuInSe_2$ Nanocrystal Photovoltaic Devices. *Opt. Express* **2010**, *18*, A411.

(14) Korala, L.; Braun, M. B.; Kephart, J. M.; Tregillus, Z.; Prieto, A. L. Ligand-Exchanged CZTS Nanocrystal Thin Films: Does Nanocrystal Surface Passivation Effectively Improve Photovoltaic Performance? *Chem. Mater.* **2017**, *29*, 6621–6629.

(15) McCandless, B. E.; Shafarman, W. N. *Chemical Surface Deposition of Ultra-Thin Semiconductors*; Google Patents, 2003.

(16) Nag, A.; Kovalenko, M. V.; Lee, J.-S.; Liu, W.; Spokoyny, B.; Talapin, D. V. Metal-Free Inorganic Ligands for Colloidal Nanocrystals: $S^{2-}$, $HS^-$, $Se^{2-}$, $HSe^-$, $Te^{2-}$, $HTe^-$, $TeS_3^{2-}$, $OH^-$, and $NH^{2-}$ as Surface Ligands. *J. Am. Chem. Soc.* **2011**, *133*, 10612–10620.

# Chapter 4: All-printed $CuInSe_2$ Nanocrystal Solar Cells

## 4.1 INTRODUCTION

The improvement that can be made to manufacturing solar cells, besides increasing yield and device efficiency, is reducing their processing costs. The processing costs are high due to high temperature and ultra-low vacuum that are traditionally required to deposit thin films. Instead, solution processing, or printing, of these thin films can be done at mild temperatures (<100 °C) and ambient pressure. Research on printed solar cells is concentrated in developing printed absorber layers while depositing all the other layers by traditional vacuum methods.[1–4] Considerable amount of research has also been done at identifying suitable solution processed alternatives to the traditional top transparent conductors deposited in ultra-low vacuum.[5–8] Very few reports have been focused on fabrication of solar cells that have all solution processed layers.[9,10] In all the devices discussed in other chapters, the $CuInSe_2$ nanocrystal absorber layer is the only printed layer. The gold back-contact, ZnO, and ITO layers are deposited in vacuum using thermal evaporation and sputtering, as per traditional methods of fabrication.

## 4.2 EXPERIMENTAL DETAILS

### 4.2.1 Materials

Copper(I) chloride (CuCl, 99.99%), elemental Selenium (Se, 99.99%), ammonium sulfide (20% in water), cadmium sulfate (CdSO4, 99.99%), thiourea (99%), oleylamine (OLA; >70%), tributylphosphine (TBP; 97%), diphenylphosphine (DPP; 98%), zinc oxide nanocrystal dispersion in butyl acetate (40 wt.%) and anhydrous toluene (99.8%) were

obtained from Aldrich; indium (III) chloride ($InCl_3$, 99.99%) was obtained from Strem Chemical; toluene, ethanol, ammonium hydroxide (18 M NH4OH) were obtained from Fisher Scientific. Silver nanowires were obtained from Carestream Advanced Materials. The oleylamine stock solution is prepared by degassing it at 110°C under vacuum overnight and stored in a nitrogen filled glovebox for future use. CuCl and $InCl_3$ are stored in the glovebox to prevent degradation. All other chemicals are used as received.

### 4.2.2 $CuInSe_2$ Nanocrystal Synthesis

CuInSe2 nanocrystals were synthesized by arrested precipitation following methods reported previously[11]. Briefly, 5 mmol of CuCl, 5 mmol of InCl3 and 1.5 ml of DPP are added to a three neck flask under an inert atmosphere. 10 mmol of Se powder is dissolved in 10 mL TBP. The flask is attached to a standard Schlenk line and degassed at 110°C for 30 minutes under vacuum. The flask is then purged with nitrogen and maintained at 110ºC for 10 more minutes. The flask is then heated to 240°C. Once the flask reaches 180°C, the Se solution is injected and the flask is allowed to reach 240°C and held for 10 minutes. The heating mantle is then removed and the flask is allowed to cool to room temperature. The nanocrystals are precipitated by adding excess ethanol and centrifugation at 4500 rpm. The nanocrystals are washed by precipitation using toluene/ethanol solvent/antisolvent pair.

### 4.2.3 PV Device Fabrication and Testing

A 5 nm chrome layer followed by 60 nm of gold layer are deposited by thermal evaporation on polished glass substrates. $CuInSe_2$ nanocrystal layer has been spin coated from a 50

mg/mL solution. The spin coating is done at two speeds - 600 rpm for 3 seconds followed by 2000 rpm for 40 seconds. A CdS layer (50 nm thick) was deposited on cured CuInSe2 nanocrystal films by chemical surface deposition. 1.25 mL of 15 mM $CdSO_4$, 2.2 mL of 1.5 M thiourea, and 2.8 mL of 18 M $NH_4OH$ in water are mixed and drop casted onto a heated (90ºC) substrate and allowed to form a CdS layer for 2 minutes. The substrate is then rinsed off with DI water. ZnO (50 nm) and ITO (300 nm) was then deposited by rf-sputter coating at 2 mtorr. Physical shadow masks were used during window layer deposition, providing an active device area of 0.1 $cm^2$. For the devices described as I, II, III and IV one or two of Au, ZnO and ITO layers are deposited in a different way and are described in their respective sections.

Current-Voltage characteristics were measured using a Keithley 2400 general purpose source meter. The devices were illuminated using a Xenon lamp solar simulator (Newport) equipped with an AM1.5G optical filter and calibrated to 100 $mW/cm^2$ light intensity with a NIST-calibrated Si photodiode (Hamamatsu, S1787-08). Incident photon conversion efficiency (IPCE) was measured using a home-built device with lock-in amplifier (Stanford Research Systems, model SR830) and monochromator (Newport Cornerstone 260 1/4M), and calibrated with Si and Ge photodiodes (Hamamatsu).

### 4.2.4 Characterization

Scanning electron microscopy (SEM) was conducted using an In-lens detector and a 5 keV accelerating voltage on a Zeiss Supra VP SEM.

## 4.3 RESULTS AND DISCUSSION

Herein, we discuss a fabrication process for an all-printed $CuInSe_2$ solar cell that greatly reduces its processing costs by reducing processing time and utilizing mild processing conditions. The fabrication is as simple as printing a newspaper and eliminates the costs associated with ultra-low vacuum and high temperature. Traditionally, gold is thermally evaporated, ZnO and ITO are sputtered. Instead, we solution processed layers of Au nanocrystals, ZnO nanocrystals, and Ag nanowires. Each of these new solution-processed layers were studied independently by building four types of devices, shown in Table 4.1 below. Each device has one traditionally processed layer exchanged with a solution processed alternative, keeping the other layers traditionally processed. In summary, we explored the effect of each new solution-processed layer on device performance and analyzed how the solution-processing procedure affects processing time.

| Device Number | Description |
|---|---|
| I | **Au nanocrystal layer**, sputtered ZnO, and sputtered ITO |
| II | thermally evaporated gold, **ZnO nanocrystals**, and sputtered ITO |
| III | thermally evaporated gold, sputtered ZnO, and **Ag nanowires** |
| IV | thermally evaporated gold, **ZnO nanocrystals, *and* Ag nanowires** |

**Table 4.1:** Table showing the four device types investigated. All of the four device types included solution-processed $CuInSe_2$ nanocrystal and CdS buffer layers.

### 4.3.1 Study of Device I: Solution Processed Gold Back-contact

The first device type includes a gold nanocrystal layer instead of a thermally evaporated gold layer. Gold nanocrystals were prepared using the method described by Yu et al.[12] The gold nanocrystals, dispersed in toluene, were diluted to 100 mg/mL and spin coated onto a glass substrate at 600 rpm for 3 seconds, followed by 1000 rpm for 40 seconds. The glass substrate with the gold nanocrystal layer was heated to 200 ºC using a hot plate, which sinters the gold nanocrystals. While these conditions yield the desired gold-thickness of 50 nm, complete coverage could not be obtained, and there were regions of exposed glass. In order to eliminate such regions, multiple layers of gold nanocrystals were deposited with heat treatment at 200º C in between each deposition.

The change in surface morphology and thickness after each spin coating and sintering step is shown in the SEM images in figure 4.1. The other layers in this device type were deposited as described in the photovoltaic device fabrication section 4.2.3. As shown in table 4.3, the highest device efficiency with the gold nanocrystal layer as the back contact is considerably lower than when gold is deposited by thermal evaporation. The JV characteristics of the device type with gold nanocrystals are displayed in figure 4.2.

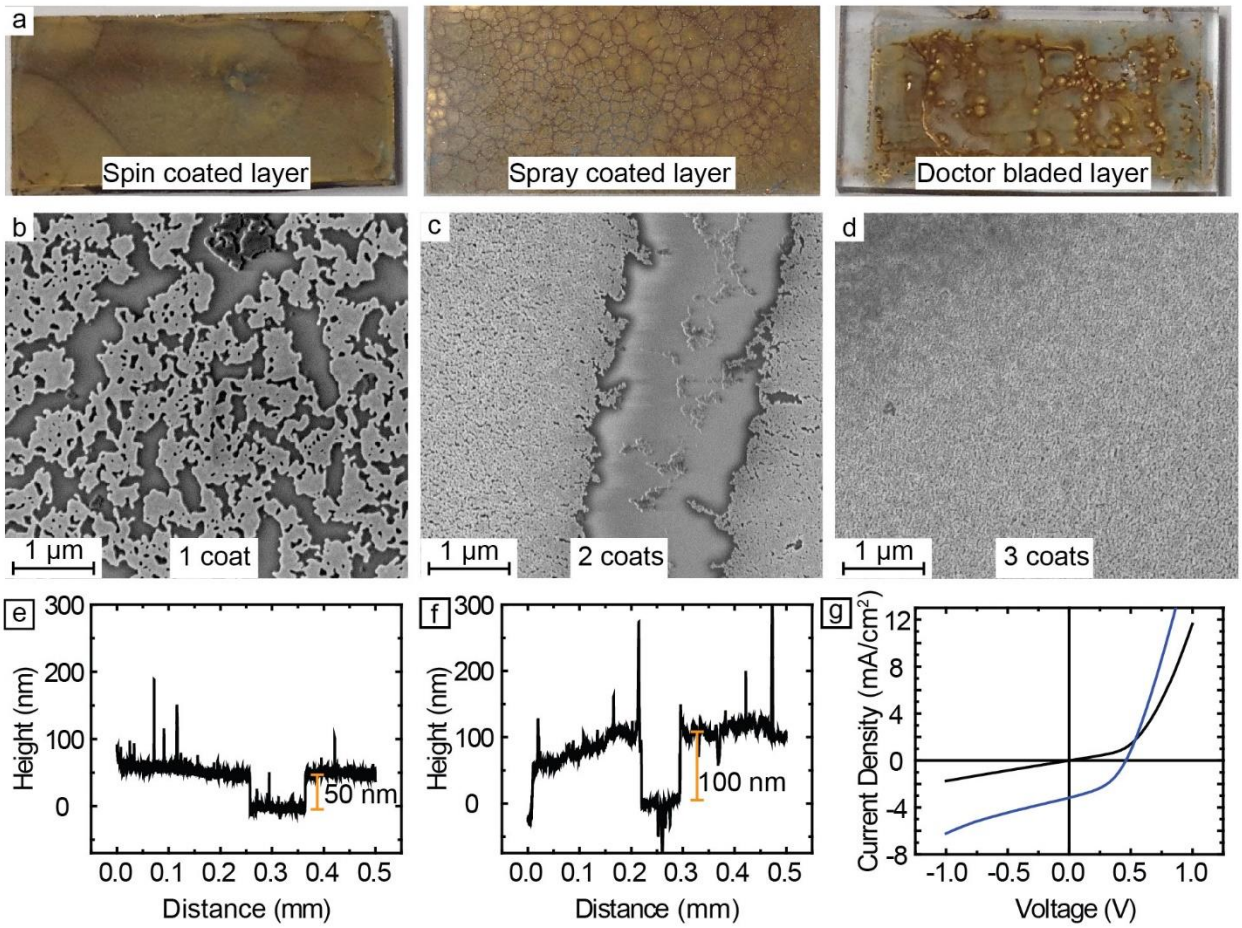


**Figure 4.1:** (a) Photographs of the sintered nanocrystal gold layer deposited by spin coating, spray coating and doctor blading. (b), (c) and (d) show SEM images of sintered gold nanocrystals after 1, 2 and 3 nanocrystal layer depositions by spin coating. Before each deposition, the gold nanocrystal layer is sintered. (e & f) Profilometry plots

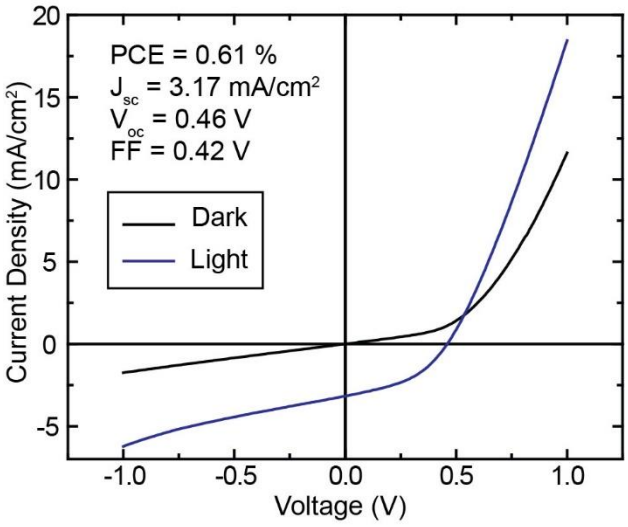


**Figure 4.2:** JV characteristics of the best performing device I.

### 4.3.2 Study of Device II: Solution Processed ZnO n-type Material

Similarly, devices were fabricated using a ZnO nanocrystal layer instead of sputtered ZnO as the n-type material. A ZnO nanocrystal dispersion in butyl acetate was purchased from Sigma Aldrich. 0.3 mL of this solution was diluted with 0.5 mL of ethyl alcohol and spin coated onto the $CuInSe_2$/CdS layer at 600 rpm for 3 seconds followed by 2000 rpm for 40 seconds. A ZnO solution was spin coated again to form a more uniform film.

We observed that baking the devices in a rapid thermal processing (RTP) improves device performance. We tested two bake procedures, shown in Table 4.2 below.

| bake procedure | description |
|---|---|
| A | bake after ZnO nanocrystal layer deposition |
| B | bake after ZnO nanocrystal layer deposition and bake after ITO sputtering |

**Table 4.2:** Bake procedures for device II and device IV.

Bake A is crucial for the functionality of the device. Without any baking, the devices do not function (Figure 4.3a). Bake A evaporates the solvent from the ZnO nanocrystal layer, causing improved charge extraction and increased short circuit current. Performing bake A under inert atmosphere is more beneficial than baking in the air because baking in air causes oxidation of the device layers, which leads to changes in the layers' electronic properties. The JV characteristics of these devices are shown in figure 4.3a.

After ZnO baking and ITO sputtering, the device fabrication is complete. We found that light soaking the completed device improves the power conversion efficiency considerably. As shown in the figure 4.3c, there is an increase in $J_{sc}$ and FF after light soaking the device for 10 minutes. A similar phenomenon was observed in bulk CIGS devices previously.[13,14] The origin of this effect is presumably related to the defects in the CIGS layer and its interface, but further investigation is needed to fully understand the reason behind the improvement in device performance on light soaking

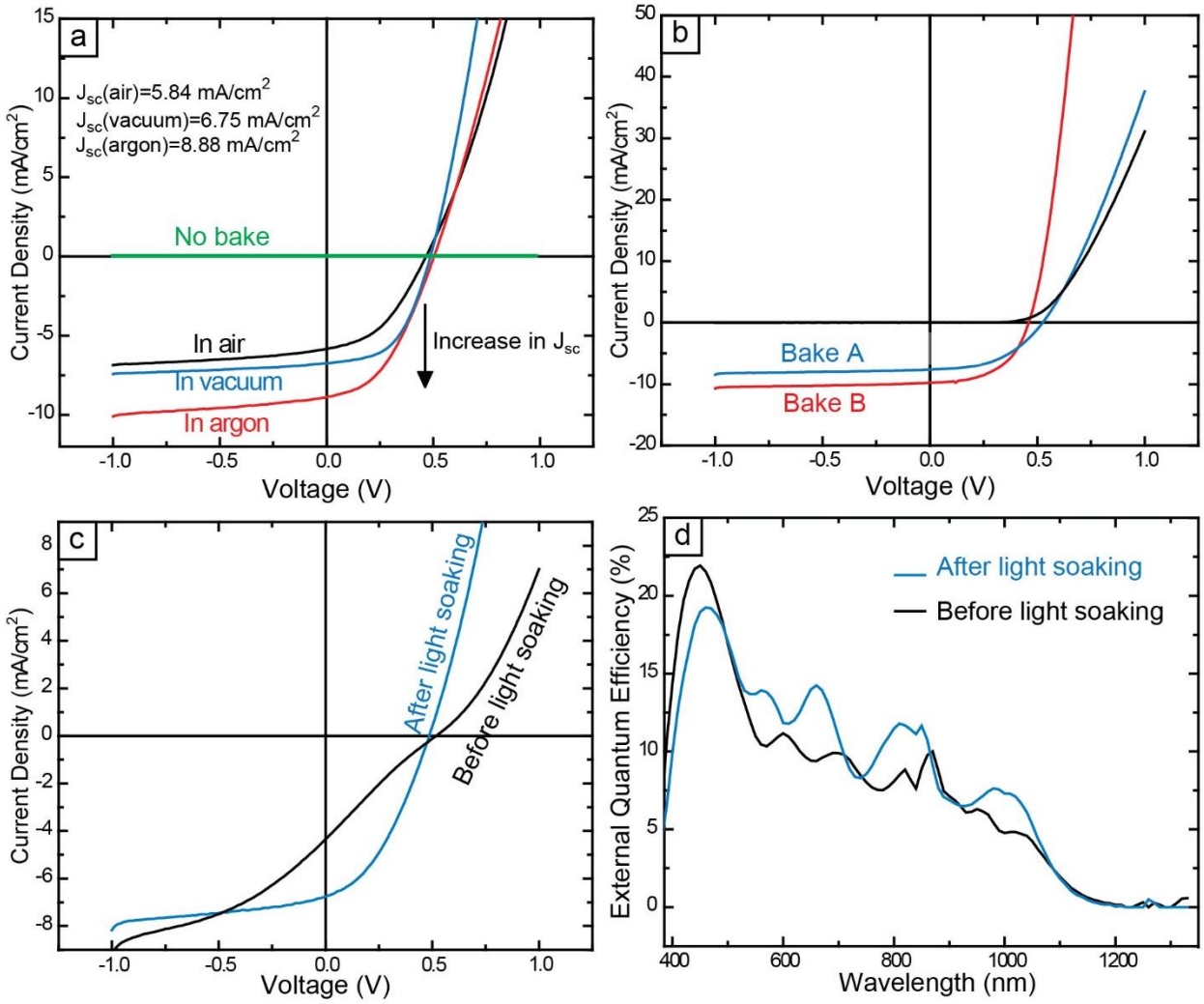


**Figure 4.3:** (a) JV light curves of device II with bake A at 200º C in air, vacuum, and argon. (b) JV curves of the best performing device II with bake A ($J_{sc}$=7.63 mA/cm$^2$, $V_{oc}$=0.52 V, FF=0.47, PCE=1.89 %) and the best performing device with bake B ($J_{sc}$=9.79 mA/cm$^2$, $V_{oc}$=0.46 V, FF=0.52 V, PCE=2.34%) at 200º C in vacuum. (c) JV light curves of device II before ($J_{sc}$=4.35 mA/cm$^2$, $V_{oc}$=0.52 V, FF=0.23, PCE=0.52 %) and after ($J_{sc}$=6.76 mA/cm$^2$, $V_{oc}$=0.49 V, FF=0.38, PCE=1.26 %) light soaking for 10 minutes and (d) corresponding EQE measured for devices shown in (c) before and after light soaking.

### 4.3.3 Study of Device III: Solution Processed Silver Nanowire Top Contact

Silver nanowires were used as a solution processed, transparent top contact instead of a sputtered ITO layer. The silver nanowires used were purchased from Carestream Advanced Materials. The nanowire solution was drop-casted onto the sputtered ZnO layer and spin coated at 600 rpm for 3 seconds followed by 2000 rpm for 40 seconds. This spin coated process was repeated one more time to create an evenly coated silver nanowire layer. After the Ag nanowire deposition, the solar device was heated to 100º C for 10 minutes on a hotplate in air to complete the device III fabrication.

Next, each 1" x 0.5" device was separated into four separate devices by scribing the continuous silver nanowire layer with a needle in order to obtain statistical replicates. To ensure that the devices were separated, each device's current was measured while only one device was placed under monochromatic light, focused to a spot size of 1 mm. If the devices were fully separated, no current was observed from the devices adjacent to the device under light.

### 4.3.4 Study of Device IV: Solution Processed ZnO Nanocrystal n-type Material and Silver Nanowire Top Contact

Lastly, we successfully incorporated both ZnO nanocrystals and Ag nanowires into a single device. The cross-sectional SEM of this device IV is shown in figure 4.4. Bake A was performed on the device, but they were never baked in vacuum; thus, vacuum was only employed for gold deposition. Additionally, the devices were separated and tested in a procedure similar to that described for device III.

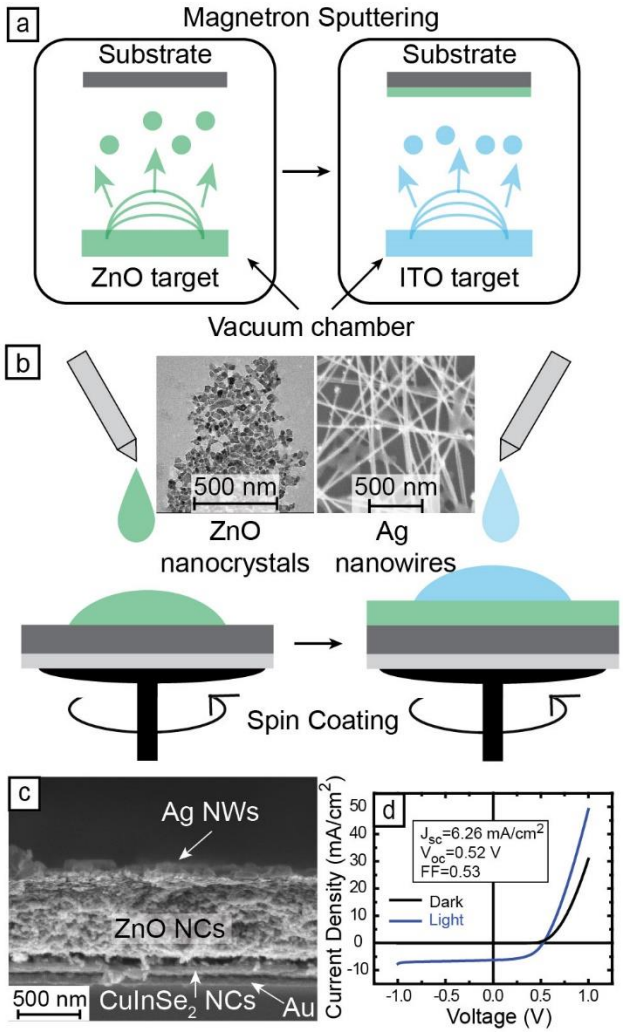


**Figure 4.4:** Illustrations showing the n-type material (ZnO) and transparent conductor (ITO/Ag NWs) deposition in $CuInSe_2$ nanocrystal solar cells using (a) vacuum based - magnetron sputtering method and (b) solution processed - spin coating method. (c) Cross-sectional SEM image of a $CuInSe_2$ nanocrystal solar cell with ZnO nanocrystals as n-type material and Ag nanowires as transparent electrode. (d) JV curve and device parameters of the solar cell shown in (c).

| Device type | Best PCE (%) | Avg. PCE (%) | Avg. $J_{sc}$ (mA/cm$^2$) | Avg. $V_{oc}$ (V) | Avg. FF |
|---|---|---|---|---|---|
| **I** | 0.61 | 0.60 | 3.08 | 0.46 | 0.43 |
| **II** | 1.89 | 1.45 | 8.25 | 0.49 | 0.42 |
| **III** | 1.94 | 1.62 | 6.03 | 0.50 | 0.54 |
| **IV** | 1.72 | 1.52 | 5.55 | 0.52 | 0.52 |
| **standard** | 2.04 | 1.93 | 6.95 | 0.48 | 0.58 |

**Table 4.3:** Device characteristics for the four types of $CuInSe_2$ nanocrystal solar cells without post fabrication vacuum bake. The values corresponding to 'standard' belong to a $CuInSe_2$ nanocrystal solar cell with thermally evaporated gold, spin coated $CuInSe_2$ layer, sputtered ZnO and sputtered ITO fabricated in the same batch, along with the 4 other devices, for comparison. The average is taken over 4 solar cells.

## 4.4 CONCLUSION

The highest PCE and the average device parameters of all four solar cell types discussed are displayed in Table 4.3. The device I performance is significantly lower than the others, and we conclude that the poor performance is due to cracks in the gold layer formed after sintering. We predict another cause of poor performance could be carbon residue remaining from the ligands of gold nanocrystals, which cause resistance to charge transfer. The gold-layer cracks are shown in figure 4.1a. In order to mitigate the gold cracking, we explored other deposition techniques such as spray coating and doctor blading, with their resulting films shown in figure 4.1a. Overall, spin coating produced the smoothest layers with the fewest cracks.

The other two solution processed layers, ZnO nanocrystals and Ag nanowires, did not have detrimental performance problems due to cracking. However, we found that the

bake A procedure is crucial to the functioning of device II. The highest PCE obtained for device II with bake A was 1.9%, and the efficiency was further improved after bake B. Thus, the highest efficiency for device II that is listed in Table 4.3 was measured after bake B. The JV curve for the best performing bake A device and the best performing bake B device are shown in figure 4.3b. Device III performance, also shown in Table 4.3, was remarkably similar to $CuInSe_2$ nanocrystal devices with vacuum-processed layers. Device IV includes both of the solution processed layers used in device II and III, and thus has comparable performance.

Finally, we compare the processing time required to fabricate a single device with one solution processed layer (or two, in the case of device IV) versus fabricating a single device with all vacuum processed layers. Each solution processed layer can be fabricated in under a minute, whereas the traditional, vacuum-based methods require 2-3 hours per layer. Thus, the overall processing time for devices I and III were reduced by 2-3 hours each because one layer was solution processed. However, device II's processing time was only reduced by 1-2 hours because the ZnO bake A requires an additional hour. Device IV required a ZnO bake as well, so its processing time was reduced by 3-5 hours instead of 4-6 hours due to its two solution processed layers.

## 4.5 REFERENCES

(1) Krebs, F. C. Fabrication and Processing of Polymer Solar Cells: A Review of Printing and Coating Techniques. *Sol. Energy Mater. Sol. Cells* **2009**, *93*, 394–412.

(2) Kan, B.; Zhang, Q.; Li, M.; Wan, X.; Ni, W.; Long, G.; Wang, Y.; Yang, X.; Feng, H.; Chen, Y. Solution-Processed Organic Solar Cells Based on Dialkylthiol-

Substituted Benzodithiophene Unit with Efficiency near 10%. *J. Am. Chem. Soc.* **2014**, *136*, 15529–15532.

(3) Tian, Q.; Xu, X.; Han, L.; Tang, M.; Zou, R.; Chen, Z.; Yu, M.; Yang, J.; Hu, J. Hydrophilic Cu2ZnSnS4 Nanocrystals for Printing Flexible, Low-Cost and Environmentally Friendly Solar Cells. *CrystEngComm* **2012**, *14*, 3847–3850.

(4) Hoth, C. N.; Schilinsky, P.; Choulis, S. A.; Brabec, C. J. Printing Highly Efficient Organic Solar Cells. *Nano Lett.* **2008**, *8*, 2806–2813.

(5) Lee, J.-Y.; Connor, S. T.; Cui, Y.; Peumans, P. Solution-Processed Metal Nanowire Mesh Transparent Electrodes. *Nano Lett.* **2008**, *8*, 689–692.

(6) Becerril, H. A.; Mao, J.; Liu, Z.; Stoltenberg, R. M.; Bao, Z.; Chen, Y. Evaluation of Solution-Processed Reduced Graphene Oxide Films as Transparent Conductors. *ACS Nano* **2008**, *2*, 463–470.

(7) Hau, S. K.; Yip, H.-L.; Zou, J.; Jen, A. K.-Y. Indium Tin Oxide-Free Semi-Transparent Inverted Polymer Solar Cells Using Conducting Polymer as Both Bottom and Top Electrodes. *Org. Electron.* **2009**, *10*, 1401–1407.

(8) Cui, J.; Wang, A.; Edleman, N. L.; Ni, J.; Lee, P.; Armstrong, N. R.; Marks, T. J. Indium Tin Oxide Alternatives—High Work Function Transparent Conducting Oxides as Anodes for Organic Light-Emitting Diodes. *Adv. Mater.* **2001**, *13*, 1476–1480.

(9) Kim, J. Y.; Lee, K.; Coates, N. E.; Moses, D.; Nguyen, T.-Q.; Dante, M.; Heeger, A. J. Efficient Tandem Polymer Solar Cells Fabricated by All-Solution Processing. *Science* **2007**, *317*, 222–225.

(10) Krebs, F. C. All Solution Roll-to-Roll Processed Polymer Solar Cells Free from Indium-Tin-Oxide and Vacuum Coating Steps. *Org. Electron.* **2009**, *10*, 761–768.

(11) Voggu, V. R.; Sham, J.; Pfeffer, S.; Pate, J.; Fillip, L.; Harvey, T. B.; Brown, R. M.; Korgel, B. A. Flexible CuInSe2 Nanocrystal Solar Cells on Paper. *ACS Energy Lett.* **2017**, *2*, 574–581.

(12) Yu, Y.; Bosoy, C. A.; Smilgies, D.-M.; Korgel, B. A. Self-Assembly and Thermal Stability of Binary Superlattices of Gold and Silicon Nanocrystals. *J. Phys. Chem. Lett.* **2013**, *4*, 3677–3682.

(13) Kobayashi, T.; Yamaguchi, H.; Nakada, T. Effects of Combined Heat and Light Soaking on Device Performance of Cu(In,Ga)$Se_2$ Solar Cells with ZnS(O,OH) Buffer Layer. *Prog. Photovolt. Res. Appl.* **2014**, *22*, 115–121.

(14) Nakada, T.; Furumi, K.; Kunioka, A. High-Efficiency Cadmium-Free Cu(In,Ga)$Se_2$ Thin-Film Solar Cells with Chemically Deposited ZnS Buffer Layers. *IEEE Trans. Electron Devices* **1999**, *46*, 2093–2097.

# Chapter 5: Flexible $CuInSe_2$ Nanocrystal Solar Cells on Paper*

## 5.1 INTRODUCTION

As an innovation, paper has had profound global impact, enabling the written document a degree of adoptability beyond stone-based tablets.[1] The device described in this paper represents an analogous step forward in the field of photovoltaics. Whereas conventional solar panels have limits of use and adoptability because of their rigid and heavy design, flexible paper PVs have the potential to power a completely different class of devices that can be integrated into everyday life. As a commodity, paper and paper products are ubiquitous in the global economy, with nearly 400 million tons of paper is produced annually. That said, paper is not yet used as a substrate to build electronics on a commercial scale. Transistors,[2–4] light emitting diodes,[5,6] electrothermochromic displays,[7] microfluidic devices,[8] and touch pads[9] have all been demonstrated on paper, but without a lightweight portable power supply. The use of paper as a substrate for these applications is countered by the need to use a stationary power supply or a heavy battery system. Paper solar cells could provide a useful power solution for these emerging devices.

Beyond portable electronics, paper solar cells offer advantages over PVs on glass or flexible substrates like metal foils and plastics, such as lower cost, consumer adoptability, eco-friendliness, biodegradability and ease of recycling.

* Large portions of this chapter were reproduced with permission from Voggu, V. R.; Sham, J.; Pfeffer, S.; Pate, J.; Fillip, L.; Harvey, T. B.; Brown, R. M.; Korgel, B. A. Flexible CuInSe2 Nanocrystal Solar Cells on Paper. *ACS Energy Lett.* **2017**, *2*, 574–581. Copyright 2017 American Chemical Society. I am the first author of the paper. My contributions include fabricating solar cells; synthesizing nanocrystals; performing SEM, AFM, and device characterizations.

Extremely light paper PVs would allow for cheap and simple shipping and installation, unlike glass-mounted solar panels. Furthermore, paper-compatible roll-to-roll manufacturing processes could dramatically increase solar cell production rates, reducing the cost and time required for processing.[10] From a manufacturing perspective, paper PVs—especially those made using nanocellulose produced using bacteria have the distinct advantage over conventional glass-mounted solar panels in that they can be cultivated and produced with little more than a simple wet laboratory set up, enabling for on-site fabrication.

To date, there have been only a few examples of paper solar cells. These have been made using organics (OPVs)[10,11] and dye-sensitized solar cell materials (DSSCs).[12] The lack of air-stability for many OPV materials makes them less compatible with paper-based processing. And DSSCs that make use of a liquid electrolyte are particularly difficult to make compatible with paper substrates. Here, we show that $CuInSe_2$ nanocrystals spray coated on paper made from pure crystalline cellulose nanofibers (synthesized by the microorganism *Gluconacetobacter hansenii*) exhibit good thermal and air-stability, with power conversion efficiencies as high as 2.25% were made—the highest efficiency yet reported for solar cells fabricated directly on paper.[13,14]

Furthermore, the paper PVs reported here show a high degree of mechanical flexibility without degradation. Devices retained their performance after more than 100 bending cycles to a radius as small as 5 mm. Past research on copper-indium-gallium-diselenide (CIGS) solar cells on flexible plastic and metal foil substrates has achieved

impressive efficiency results, similar to those obtained on glass; however, these devices have not been particularly flexible.[15–18] The smallest bending radius reported for CIGS solar cells without considerable performance loss is only 2 cm.[19] The nanocellulose paper PVs with a nanocrystal absorber layer of $CuInSe_2$ operated at much smaller bending radius (5 mm), even without replacing the typically brittle indium-tin-oxide (ITO) transparent conducting oxide (TCO) layer with alternative "flexible" transparent conducting electrode materials. The nanocrystal paper PVs also functioned when folded across the active region of the device.

## 5.2 EXPERIMENTAL DETAILS

### 5.2.1 Materials

Copper(I) chloride (CuCl, 99.99%), elemental selenium (Se, 99.99%), cadmium sulfate (CdSO4, 99.99%), thiourea (99%), oleylamine (OLA; >70%), tributylphosphine (TBP; 97%), diphenylphosphine (DPP; 98%), carboxymethylcellulose and anhydrous toluene (99.8%) were obtained from Aldrich; indium (III) chloride ($InCl_3$, 99.99%) was obtained from Strem Chemical; toluene, ethanol, hexanes, and ammonium hydroxide (18 M $NH_4OH$) were obtained from Fisher Scientific. The cellulose membranes were produced in Schramm Hestrin (SH) medium (Schramm and Hestrin 1954) consisting of (per liter): 20.0 g of glucose (Fisher D16-10), 5.0 g of bacto peptone (BD 211820), 5.0 g bacto yeast extract (BD 212720), 2.7 g of sodium phosphate dibasic heptahydrate (Fisher 7782-85-6), and 1.5 g of citric acid (Mallinckrodt 0627-12). 200 mL of a stock solution of oleylamine was degassed under vacuum overnight at $110^0$C in a 250 mL glass 3 neck flask and stored in a nitrogen filled glovebox until further use. All other chemicals are used as received.

### 5.2.2 $CuInSe_2$ Quantum Dot Synthesis

$CuInSe_2$ nanocrystals were synthesized using a modification of published methods.[20,21] Two reactant solutions were prepared in a nitrogen-filled glovebox: (1) an oleylamine reactant solution was prepared by combining CuCl (0.495 g, 5 mmol), $InCl_3$ (1.106 g, 5 mmol), and 1.5 mL DPP with 50 mL oleylamine in a 125 mL three-neck flask, and (2) a TBP:Se reactant solution prepared by dissolving elemental Se (0.79 g, 10 mmol) in 10 mL TBP. The oleylamine reactant flask was sealed with rubber septa, brought out of the glovebox and attached to a Schlenk line. The flask was heated to 110°C for 30 min under vacuum, then filled with nitrogen and the temperature is maintained at 110°C for 10 more minutes. Then the reaction flask is heated to 180°C while maintaining $N_2$ atmosphere. The Se precursor solution was loaded into a 12 mL plastic syringe, brought out of the glovebox and rapidly injected into the oleylamine-containing flask. The temperature was raised to 240°C and maintained for 10 min. The heating mantle was then removed and the reaction mixture was allowed to cool to room temperature.

The nanocrystals were isolated from the crude reaction mixture by precipitation with 20 mL of ethanol and centrifugation at 4500 rpm for 10 minutes. The yellow supernatant was discarded. Toluene is added to the nanocrystals using a pipette in steps of 1 mL, until all the nanocrystals redisperse (typically a total of 7 mL). 6 mL of ethanol is added to this dispersion to reprecipitate the nanocrystals. The dispersion was centrifuged at 4500 rpm for 10 min and the supernatant discarded. The precipitate was redipsersed with a minimal amount of toluene (≈7 mL) for transfer to a 20 mL glass vial. The nanocrystals were dried, transferred into a $N_2$ filled glovebox and dispersed in anhydrous toluene at a concentration of 100 mg/mL for further use. The nanocrystals were diluted to a concentration of 10 mg/mL in toluene for spray deposition during PV device fabrication.

### 5.2.3 Synthesis and Preparation of Cellulose Substrates

Pure crystalline cellulose was produced using *Gluconacetobacter hansenii* ATCC 53582 strain NQ5.[22] Liquid cultures of *G. hansenii* NQ5 were grown to log phase until reaching an optical density of 2 at 600 nm. 10 mL of the resulting inoculum was added to a culture tray containing 500 mL SH media[23] supplemented with 0%, 2%, or 4% carboxymethylcellulose (CMC). The trays were allowed to incubate under static conditions for 7 to 14 days at 28˚C. The pellicles were harvested and the cells were removed using a 2% solution of Alconox (Sigma-Aldrich 242985) and stored in an aqueous solution of 20% ethanol until further use.

*G. hansenii* ATCC 53582 strain NQ5 is a rod shaped, aerobic, gram negative bacterium that synthesizes cellulose through linear pores along the long axis of the cell resulting in a cellulose membrane at the air liquid interface.[22-24] Examination of the pellicle suggests two slightly different morphologies with respect to the top (surface at the air liquid interface) and bottom of the membrane (inside the liquid). The top appeared to be stronger and denser than the bottom and provided a smoother surface for solar cell application while the bottom would flake and peel after drying. It has not been extensively studied, but the discrepancy may be due to the synthesis of cellulose by the newly inoculated cells before increased cell division occurs. That initial cellulose appears to be less organized and weaker than cellulose produced after doubling time (1.5 to 8 hr.) due to the fewer number of cells in the medium.[25] During the division process, the cells continue synthesizing cellulose creating a branching point upon separation. Repetition of this produces a cascade of branchings that form the stronger matrix at the top of the membrane with respect to the bottom.[22,25] To prepare the membrane as a PV substrate, the pellicle was placed with the nanocellulose surface at the air liquid interface faced down on a smooth Teflon sheet (16

cm x 16 cm). The pellicle was then pressed to eliminate bubbles. A cotton fiber fabric was then placed on top of the cellulose and further pressed to release air trapped between the materials. The Teflon sheet was then placed inside a 15-ton hydraulic press. The press was slowly lowered to remove as much water as possible, allowing for easier material handling. The plate and fabric were then removed from the press leaving behind the compressed cellulose, with the air liquid interface side face down on the Teflon sheet. A rectilinear stretching armature (made from surfaced pine wood) was placed on the microbial cellulose. Each side of the cellulose was gently lifted and a staple placed into the wood armature starting from the center, working outwardly toward the corners. After each staple placement, more pressure was applied before placing the next, allowing for even surface tension on the cellulose, and uniform pressure on the armature. The corners were evenly folded, in a manner similar to the conventional method of mounting linen onto canvas stretchers in preparation for an oil painting. After stretching, the cellulose was dried with a hair dryer on low heat for one hour to dry the surface. The substrate was left overnight at room temperature to dry completely.

### 5.2.4 PV Device Fabrication and Testing

Glass microscope slides cut into 1" x 1" dimensions were used as a support media for fabricating the solar cells on microbial cellulose substrates. The cellulose substrates were mounted on glass slides using either Kapton tape or PDMS as adhesives. PDMS was prepared by heating a siloxane monomer and a cross linking agent (Sylgard Elastomer 184, Dow Corning Corporation) in a 1:30 weight ratio on the glass slide at $150^0$C for 15 min. A 10 nm layer of chrome and 80 nm gold layer were thermally evaporated onto the cellulose layers. $CuInSe_2$ nanocrystals were spray deposited onto substrates heated to 100°C with a

Sonotek ExactaCoat ultrasonic automated spray system equipped with a 120 kHz ultrasonic nozzle. The spray nozzle was rastered across a rectangular area with 3 mm raster spacing, a speed of 10 mm/sec, an ink injection rate of 0.1 mL/min, an air pressure of 1.6 psi and a nozzle-to-substrate separation of 11.5 cm. CdS was deposited by a chemical bath deposition procedure onto the $CuInSe_2$ nanocrystal layer.[26] 0.7 mL of CdS precursor solution (1.25 mL of 15 mM $CdSO_4$, 2.2 mL of 1.5 M thiourea, and 2.8 mL of 18 M $NH_4OH$ in water) was dropped onto each 1"x1" $CuInSe_2$ deposited cellulose-glass substrate heated to 90°C on a hot plate and covered with an inverted crystallization dish for 2 min. The substrates were then rinsed with DI water and dried with compressed nitrogen. Top contact layers of i-ZnO and ITO were deposited by Radio Frequency (RF) sputtering using ZnO (99.9%) and ITO targets from Lesker (99.99% $In_2O_3$:$SnO_2$ 9:1) in Ar atmosphere. ZnO and ITO were deposited selectively onto 8 rectangular regions using shadow masking, with active device areas varying from 0.08 $cm^2$ to 0.15 $cm^2$. Silver paint was applied to the contacts for PV performance testing.

PV current-voltage characteristics were measured using a Keithley 2400 general purpose source meter and a xenon lamp source meter equipped with A.M. 1.5 filter. EQE measurements were made using a home-built spectrophotometer with lock-in amplifier (Stanford Research Systems, model SR830) and monochromator (Newport Cornerstone 260 1/4M), and calibrated with Si and Ge photodiodes (Hamamatsu). The monochromatic light used in the instrument is generated using a commercial monochromator (Newport Cornerstone 260 1/4M) chopped at 213 Hz and focused to a spot size of 1 mm diameter on the active region.[2]

### 5.2.5 Characterization

Scanning electron microscopy was done on a Zeiss Supra 40 VP SEM operated at 5 keV accelerating voltage. Atomic force microscopy was performed on Asylum MFP-3D AFM in tapping mode.

## 5.3 Results and Discussion

### 5.3.1 The Role of Type of Paper Substrate on PV device Fabrication and Performance

Our first tests to make paper PVs used standard office paper as a substrate with the standard device stack of a bottom contact layer of gold, an ink spray-deposited layer of $CuInSe_2$ nanocrystals, a CdS buffer layer and a top contact of ZnO/ITO. None of these devices worked. It became immediately apparent that the type of paper used as the substrate is critical and that we would need to modify the paper to make a functioning solar cell.

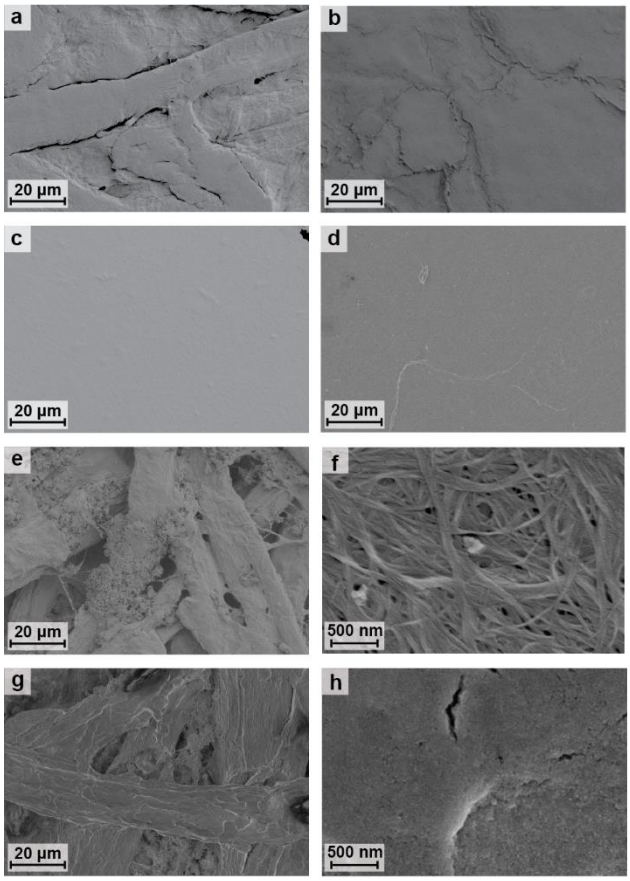


**Figure 5.1:** SEM images of different kinds of paper tested as PV substrates: (a) wax paper; (b) parafilm; (c) photo printing paper; (d) bacterial cellulose; (e) office paper; (f) bacterial cellulose. (g) and (h) show SEM images of (g) office paper and (h) bacterial cellulose paper coated with $CuInSe_2$ nanocrystals.

Figure 5.1 shows scanning electron microscope (SEM) images of the various types of paper that were tested. The cellulose fibers in standard office paper (Figure 5.1e) and wax paper (Figure 5.1a) are quite thick, generally more than 10 µm in diameter, resulting in very large pores in the substrate. The cellulose fibers in parafilm are not visible in the SEM images because of plastic fillers, but the surface of the paper is still very rough as a

result of the large cellulose fibers in the material (Figure 5.1b). None of the PVs fabricated on office paper, wax paper or parafilm worked. Photoprinting paper has a very smooth surface with fewer pores than office paper (Figure 5.1c). However, photoprinting paper also did not work because the device layers had very poor adhesion to the substrate. The deposited nanocrystal layer/Au/Cr back contact stack would rinse off the substrates during the CdS deposition step (see Figure 5.2). One other problem with all four of these types of paper was water uptake during the CdS deposition step. This led to wrinkling and made it impossible to fabricate PVs with reasonable device integrity (Figure 5.2 shows SEM images and photographs of these four types of paper after the CdS deposition step.) One way that others have avoided some of these problems has been to use only dry deposition processes, as in the case of organic solar cells.[11]

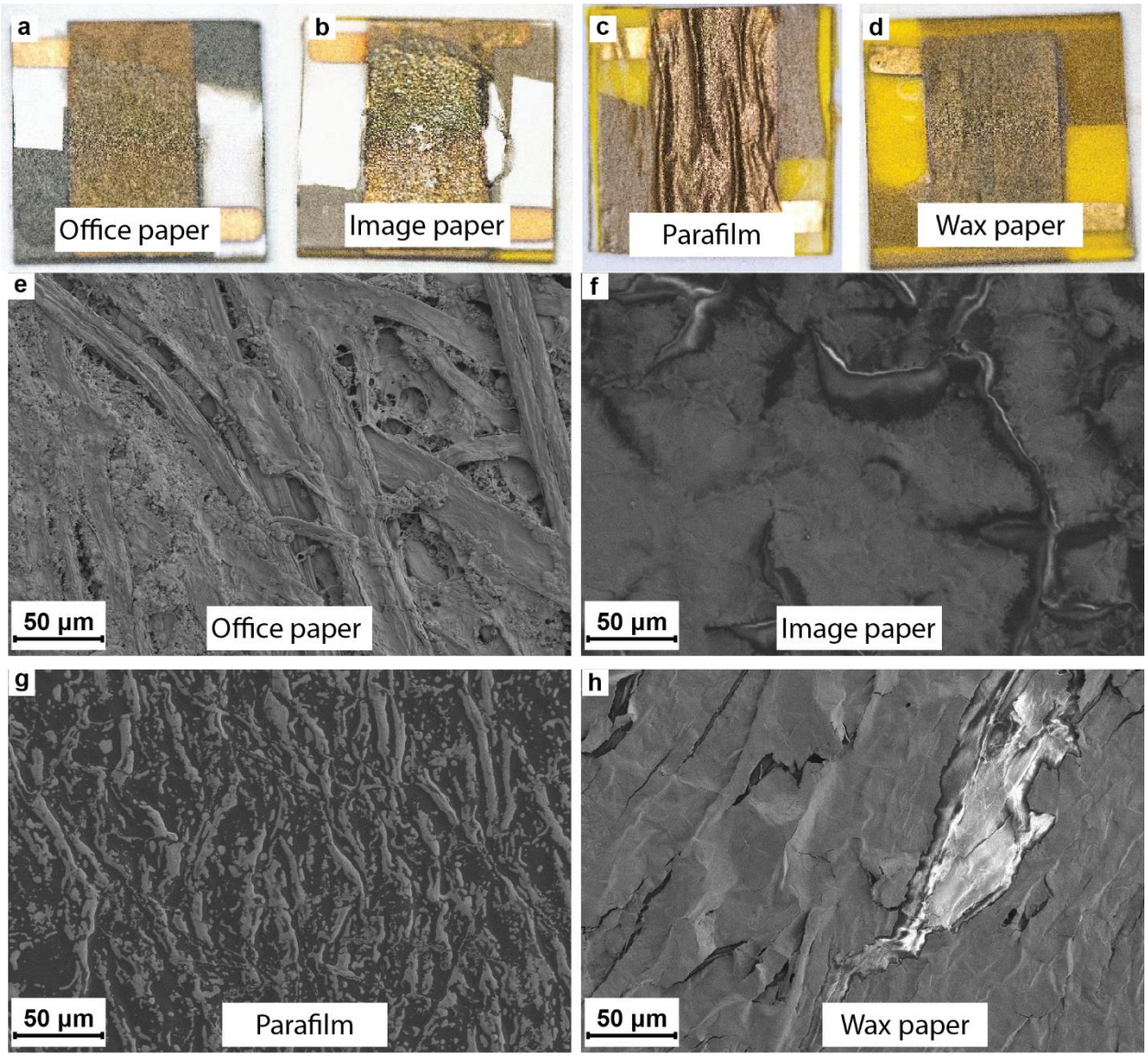


**Figure 5.2:** (a-d) Photographs of nanocrystal PVs after CdS deposition on different kinds of paper. (e-h) SEM images of different kinds of paper after CdS deposition.

Paper made of bacterial nanocellulose did not have the same process incompatibilities as the other paper substrates. Bacterial nanocellulose fibers are orders of magnitude smaller in diameter (~100 nm) than the cellulose fibers found naturally in plant material (>10 μm in diameter), and provide a much smoother paper surface with smaller pores.[27] Figure 5.1d shows an SEM image of a bacterial cellulose substrate. Figures 5.1g and 5.1h show SEM images of standard office paper and nanocellulose paper with 80 nm of gold and a layer of $CuInSe_2$ nanocrystals. The pores of the underlying office paper are still visible (Figure 5.1g), but there are no observable pores when bacterial cellulose paper is the substrate (Figure 5.1h). Pores lead to electrical shorts in the device and having a uniform, continuous coating of nanocrystals is critical for making paper PVs.

Nanocellulose paper PVs were made using the standard device stack of a bottom contact layer of chrome followed by gold, an ink spray-deposited layer of $CuInSe_2$ nanocrystals, a CdS buffer layer and a top contact of ZnO/ITO that have been optimized for devices on glass.[20] The performance of devices made with a range of nanocrystal layer thicknesses is shown in Figure 5.3a. AFM images of the nanocrystal-coated paper substrate and nanocrystal coated glass substrate are shown in Figures 5.3c and 5.3d. Figure 5.4 shows an SEM image of a cross-sectioned $CuInSe_2$ nanocrystal PV on a bacterial nanocellulose paper substrate. The device efficiency was the highest after three coats of nanocrystals had been applied (~150 nm layer thickness). A leveling off of device performance with increasing nanocrystal layer thickness is similar to what is observed on glass.[20]

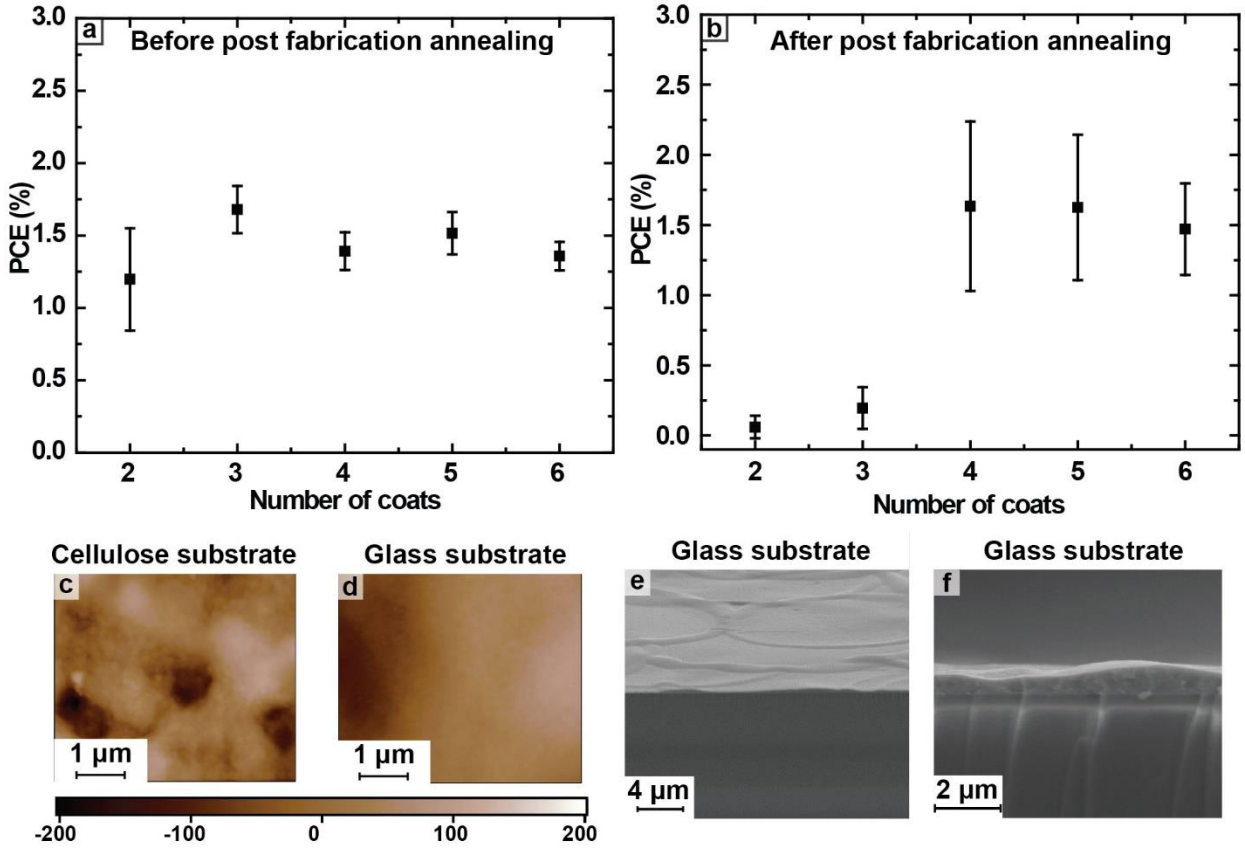


**Figure 5.3:** Power conversion efficiency (PCE) of $CuInSe_2$ nanocrystal PVs on bacterial cellulose paper measured under AM 1.5 illumination (100 $mW/cm^2$) (a) before and (b) after rapid thermal processing (RTP) of completed devices at $200^0C$ for 5 min under vacuum. Error bars represent standard deviation. AFM images of $CuInSe_2$ layer on (c) bacterial cellulose and (d) glass substrate. (e,f) SEM images of a sprayed $CuInSe_2$ nanocrystal layer on gold-coated glass. Devices made with only one coat of nanocrystals are not plotted because these devices were generally shorted.

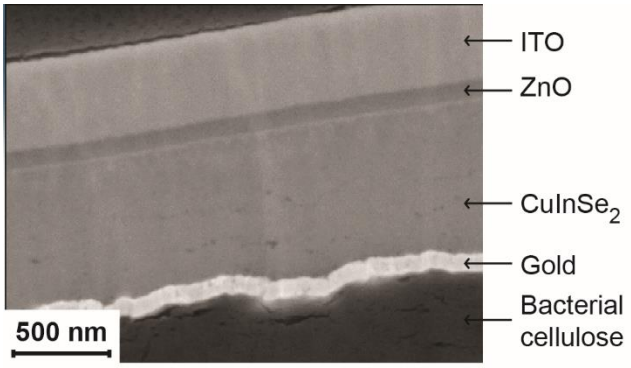


**Figure 5.4:** SEM image of a cross-sectioned $CuInSe_2$ nanocrystal PV on bacterial nanocellulose. (Published with permission from JEOL USA Inc.) An Argon ion beam was used to create pristine cross-sections.

$CuInSe_2$ nanocrystal PVs on glass are generally put through a post-fabrication heating step to improve device efficiency by about a factor of two.[20] We believe that the increase in PCE after annealing is due to defect passivation of surface selenium deficiencies similar to what is observed by Rau et al.[28] In very thin $CuInSe_2$ films (less than 4 coats) the number of surface defects is smaller than thicker films which results in excess incorporation of oxygen leading to poor device performance. We carried out an analogous post-fabrication thermal treatment on the paper PVs by rapid thermal processing (RTP) at 200$^{o}$C under vacuum for 5 min (See figure 5.5 for more RTP device data). The average PCE and standard deviation in PCE as a function of thickness of $CuInSe_2$ layer after annealing is shown in Figure 5.3b. the device data in both the plots 5.3a and 5.3b is over 6 to 8 devices depending on the number of shorted devices excluded that are excluded from the statistics. The performance of devices with thicker nanocrystal layers (>3 coats) improved in half of the devices but also fell in the remaining half (figure 5.3b and 5.6) making the average PCE to be around the same value while pushing the best efficiency to

2.25%. In devices with thinner nanocrystal layer, the devices performed very poorly due to the above-mentioned reasons of excess oxygen incorporation.

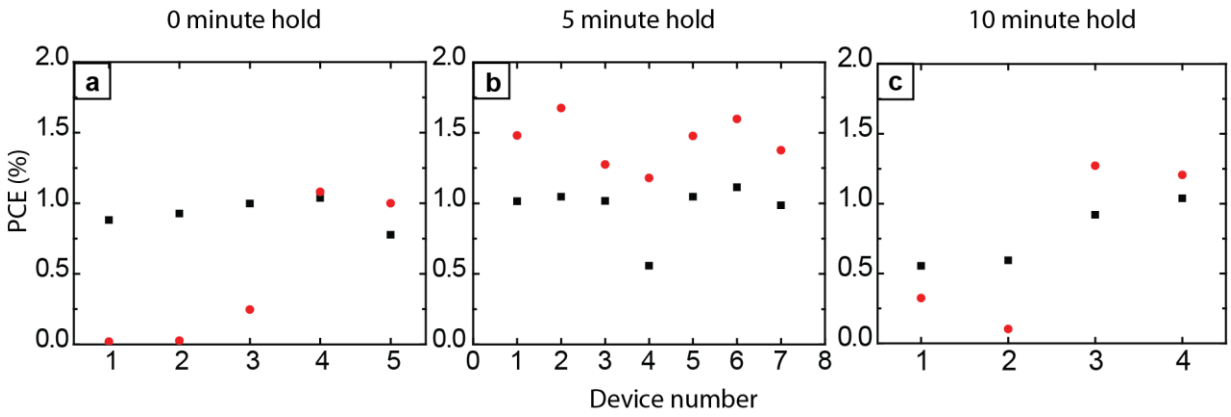


**Figure 5.5:** Power conversion efficiency (PCE) of $CuInSe_2$ nanocrystal PVs tested under AM 1.5 illumination (100 $mW/cm^2$) on bacterial cellulose ( ■ ) before and (●) after heating at 200°C under vacuum for (a) 0 min, (b) 5 min, and (c) 10 min.

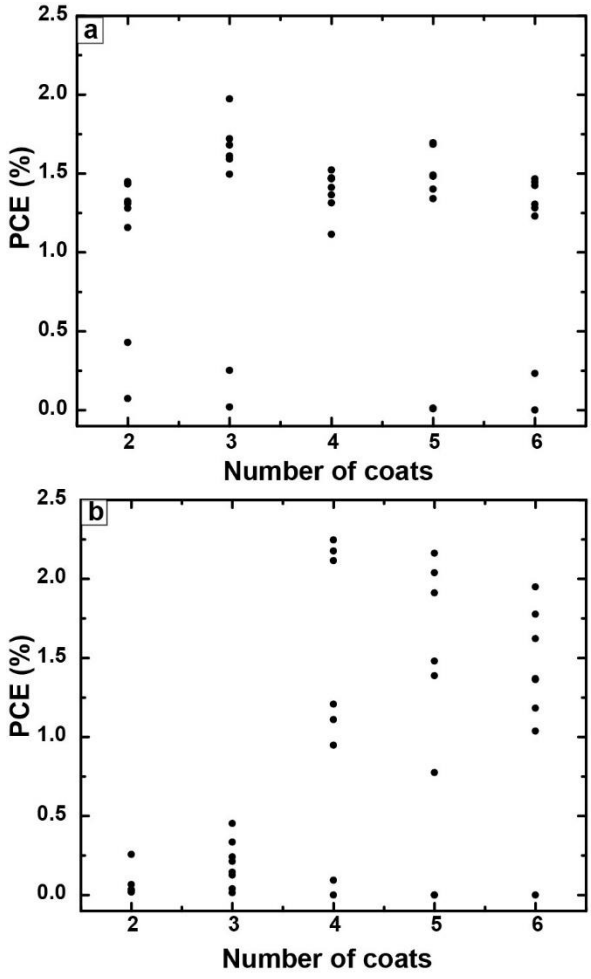


**Figure 5.6:** Power conversion efficiency (PCE) of $CuInSe_2$ nanocrystal PVs on bacterial cellulose paper measured under AM 1.5 illumination (100 $mW/cm^2$) (a) before and (b) after rapid thermal processing (RTP) of completed devices at $200^0C$ for 5 min under vacuum.

Figure 5.7 shows the current-voltage response of a typical device after this heating step. The PCE of 2.25% is the highest achieved to date for a solar cell fabricated directly on paper. The previously reported best efficiency was 1.3% for an OPV device on paper,[10] and there is one report of 4% PCE on paper, but this device was fabricated on a zinc-coated

polypropylene foil (functioning as back electrode) glued onto a piece of paper.[29] The power to weight ratio of these devices is around 0.35 to 0.4 W/g, which is similar to high efficiency Si and triple junction solar cells with power to weight ratios of 0.82 and 0.39 W/g, respectively.[30] The paper PVs are much lighter, although less efficient.[30]

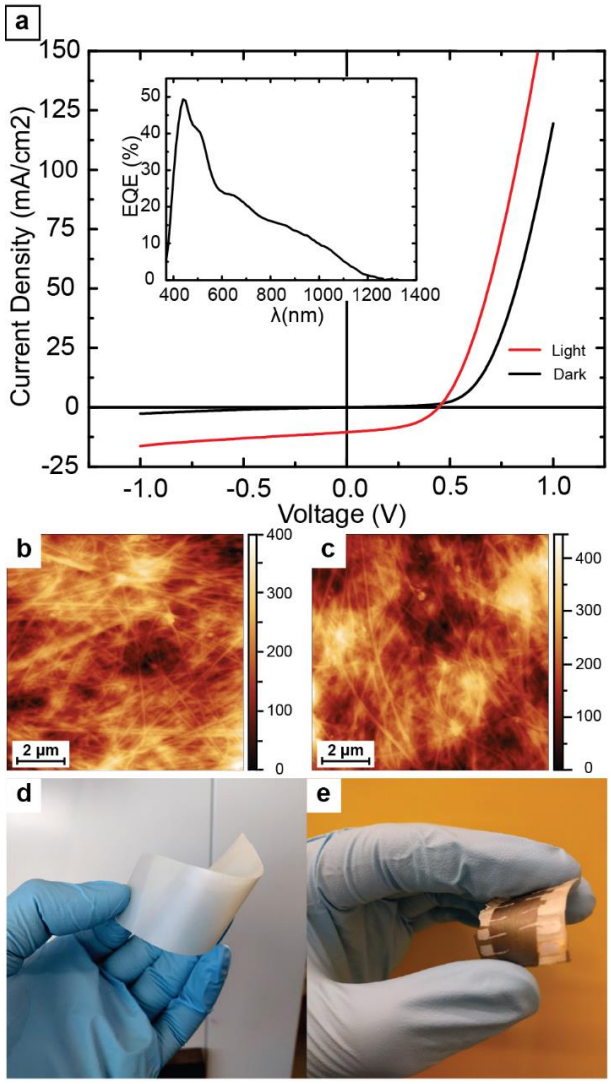


**Figure 5.7:** (a) *J-V* curves of a $CuInSe_2$ nanocrystal PV on bacterial cellulose with a PCE of 2.25%, short circuit current density $J_{sc}$=10.47 Ma/cm$^2$, open circuit voltage $V_{oc}$=0.44 V and fill factor FF=0.48. Inset: External quantum efficiency (EQE) of the device measured under AM 1.5 with 50 mW/cm$^2$ white light bias. The short circuit current calculated from the EQE curve measured under white light bias is 9.2 mA/cm$^2$, which is 12% less than the $J_{sc}$ measured for the device and within reasonable limits. (b, c) AFM images of bacterial cellulose substrates before and after depositing 80 nm of Au. (d) Photograph of bacterial cellulose paper. (e) A bacterial cellulose substrate with eight $CuInSe_2$ nanocrystal PVs, each with an active area of 0.1 cm$^2$.

One aspect of the paper PVs that requires future improvement is the need to reduce the variation in device performance. The variation in device performance on paper is considerable compared to similar $CuInSe_2$ nanocrystal PVs made on glass. On glass, the devices before the post fabrication baking step with 5 coats of $CuInSe_2$ nanocrystals, have a standard deviation in PCE of about 5.6% (Data in Figure 5.8). The standard deviation in device PCE before post baking on paper was 32% (devices with five spray coats). Post-fabrication heating helped improve overall device performance (Figure 5.3b), but did not help alleviate large variations in performance. The performance variation on paper results from uneven surface morphology, as shown in the AFM images in Figures 5.3c and 5.7b. The surface roughness of the bacterial cellulose substrates is about 100 nm and gold deposition does not reduce the surface roughness (Figure 5.7c). This surface roughness also limits the device efficiency to some extent, as devices fabricated on glass have achieved higher efficiencies of up to 3.1%.[20] Spray-deposited $CuInSe_2$ nanocrystal layers on glass also exhibit some thickness non-uniformity due to solvent drying rings (Figures 5.3d-5.3f), but this is relatively insignificant compared to the non-uniformities related to the paper substrate. Increasing the number of nanocrystal layer deposition cycles did not improve the layer uniformity either (Figure 5.9), although the variation in device performance was slightly better with the thicker nanocrystal films. The standard deviations in PCE for devices before post baking made with 4, 5 and 6 spray coats were 37%, 32% and 22%, respectively. In all cases, the device yield is less than desirable, as at least one or two devices in eight were shorted and did not function.

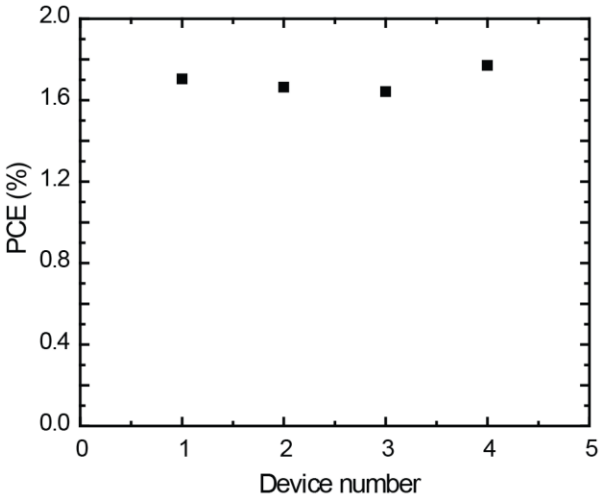


**Figure 5.8:** PCE of $CuInSe_2$ nanocrystal PVs on glass before heating with 5 deposition cycles of $CuInSe_2$ nanocrystals.

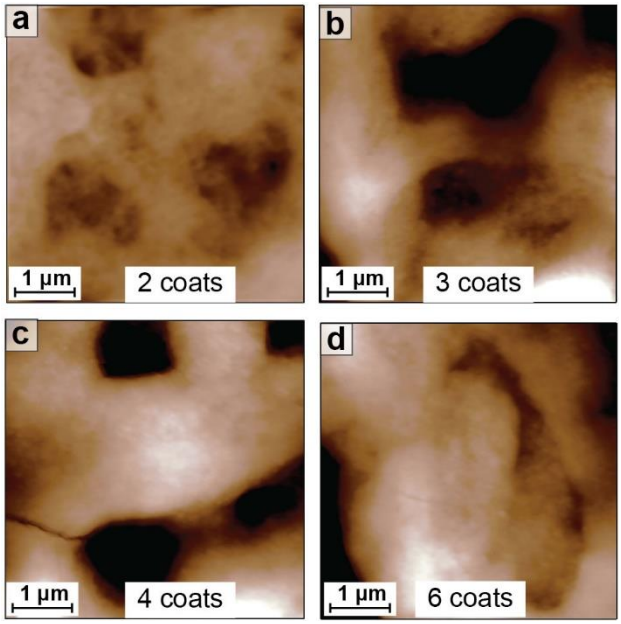


**Figure 5.9:** AFM images of $CuInSe_2$ nanocrystals sprayed onto gold coated bacterial cellulose substrates at various thicknesses.

### 5.3.2 Flexibility of $CuInSe_2$ Nanocrystal Solar Cells on Paper

Most research making solution-processed flexible solar cells has focused on organic materials on transparent conducting ITO layers; however, ITO is brittle and tends to limit the mechanical flexibility of the device. As a result, a number of ITO alternatives have been studied for P3HT:PCBM OPVs including carbon nanotubes, graphene, PEDOT:PSS, metal based transparent electrodes (Ag, Cu nanowires), [31–34] but the ITO-based devices have had significantly higher device efficiencies.[35] We find that ITO layers on nanocellulose paper substrates tolerate much more mechanical flexing than on plastic. As shown in Figures 5.10a-5.10c, the ITO and nanocrystal layers crack when deposited on polyethylene terephthalate (PET) substrates after bending to a radius of 10 to 15 mm. The nanocrystal devices on nanocellulose substrates are much more structurally resilient. Figure 5.10d plots the device characteristics of the PVs on nanocellulose substrates measured after a series of flex cycles to a 5 mm bending radius. There was no significant change in performance after 120 mechanical flexing cycles. Movie 2 in supporting information shows the open circuit voltage that is being measured after bending the device. As shown in the SEM image in Figure 5.10f, these solar cells did not show any cracks in the ITO layer even after bending to a radius of 5 mm for more than 100 times. The curved line features in the SEM image are due to differences in ITO thickness caused by the rough bacterial cellulose substrate and the uneven $CuInSe_2$ layer, and are not cracks. The bacterial cellulose substrates enable the use of ITO as the top electrode without sacrificing mechanical flexibility.

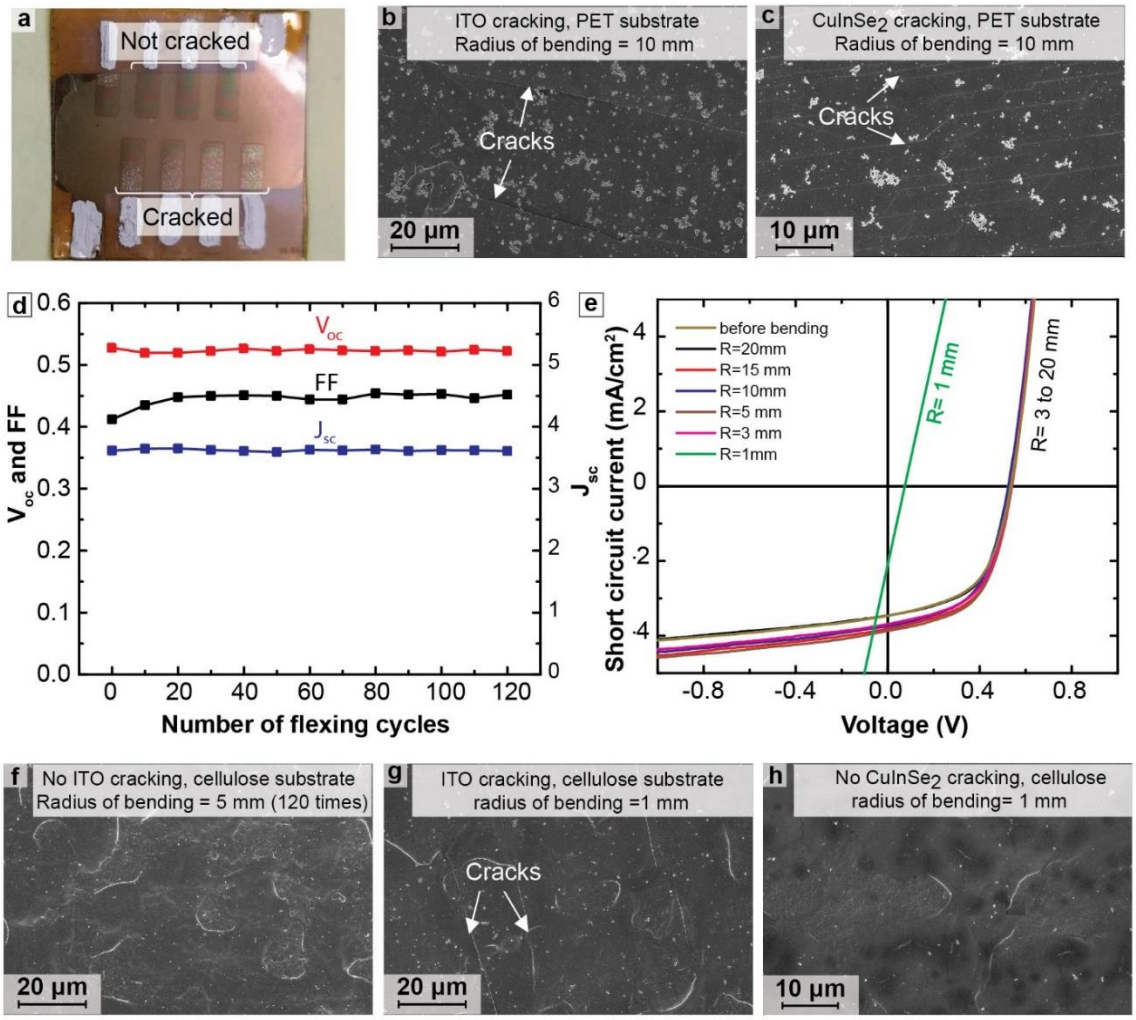


**Figure 5.10:**(a) $CuInSe_2$ nanocrystal PVs on PET: the top devices have not been bent and the bottom side devices have been bent to 10 mm radii. (b, c) SEM images of ITO and $CuInSe_2$ nanocrystal layers in PET substrate devices after bending to 10 mm radius. (d) Average device characteristics for four $CuInSe_2$ nanocrystal PVs on bacterial cellulose substrates measured as a function of number of flex cycles ($R$=5 mm). (e) $J$-$V$ curves of $CuInSe_2$ nanocrystal PV device on bacterial cellulose in flat orientation after bending to various radii. (f) SEM image of the ITO layer in a PV device fabricated on bacterial cellulose after flexing 120 times (R= 5mm). (g, h) SEM images of the ITO and $CuInSe_2$ nanocrystal layers in bacterial cellulose devices after bending to 1 mm radius.

Figure 5.10e shows the device performance of the bacterial cellulose paper PVs after flexing to different radii of curvature. The devices work after bending to a radius as small as 3 mm. Bending further to a radius of 1 mm destroys the device. Bending to a radius of curvature of 1 mm led to cracks in the ITO layer as shown in the SEM image in Figure 5.10g. Even though these devices failed, the cracks were much smaller than those observed in the ITO layers on PET after flexing. It appears that the underlying roughness of the bacterial cellulose substrate helps to limit the propagation of cracks in the $CuInSe_2$ layer as shown in the SEM image in Figure 5.10h where no cracks were observed even after bending the layer to a radius of 1 mm This limitation of the crack propagation in the $CuInSe_2$ layer and strong adhesion between the nanocrystal layer and the underlying nanocellulose substrate help stabilize the ITO layer.

PDMS was found to be an effective releasable adhesive for the nanocellulose device fabrication on a solid glass support. It was difficult to unmount the paper devices from the glass support without a sacrificial layer. When Kapton tape was used as an adherent, it was not possible to unmount the devices after fabrication without destroying the device. PDMS was stable at the processing temperatures and thermally conductive, and could be released for unmounting. PDMS has all these required properties and is the ideal glue for unmounting completed devices from glass.[36]

Paper PVs were also tested while being bent, as shown in Figure 5.11a. The observed decrease in short circuit current with decreased bending radius results from the loss of incident light intensity upon bending, as illustrated in Figure 5.11a.[37] The *J-V*

characteristics return after returning the device to the flat configuration (inset in Figure 5.11b).

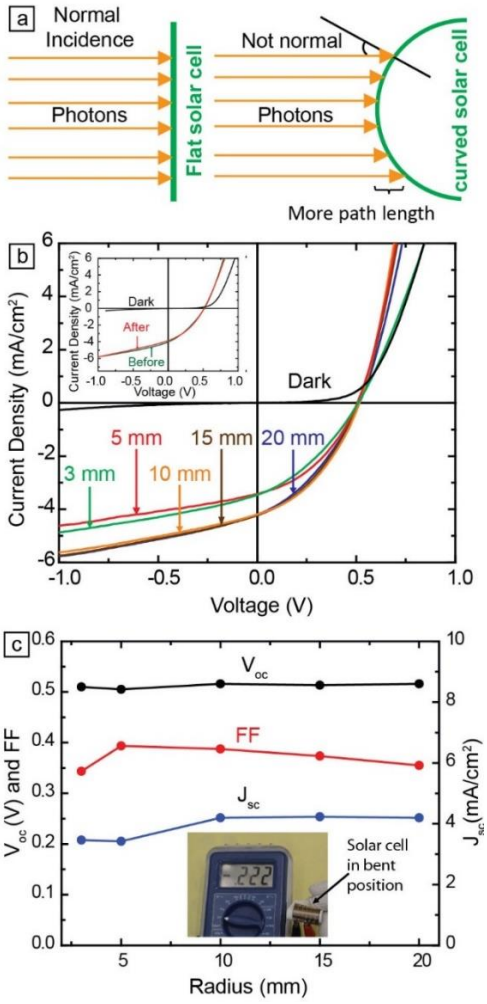


**Figure 5.11:** (a) Illustration of how the illumination changes when the device is curved. (b) *J-V* response of $CuInSe_2$ nanocrystal PVs on bacterial cellulose at various bending radii. Shown in the inset is the JV curve before and after all the bending tests were performed. (c) Device characteristics of $CuInSe_2$ nanocrystal PVs on bacterial cellulose measured while being bent plotted as a function of bending radii. Inset shows the picture of a nanocellulose device whose open circuit voltage is being measured with a voltmeter in ambient lighting.

### 5.3.3 Foldability of $CuInSe_2$ Nanocrystal Solar Cells on Paper

Figure 5.12a shows the device response of a folded $CuInSe_2$ nanocrystal PV on bacterial cellulose. The device retains more than 80% of its efficiency after folding and unfolding. There have been examples of "foldable" PVs reported in the literature, but these have only functioned when folded in places away from the active area of the devices.[38,39] In the case of the bacterial nanocellulose PVs, the solar cell is actually folded across the active layer in the device and the device response was stable after 5 cycles of folding and unfolding. Eventually, the device failed after folding due to the formation of large cracks in the ITO and nanocrystal layers, as shown in the SEM images in Figures 5.12b and 5.12c. Cracking is observed in the nanocrystal layer only in regions where the layer was relatively thick (Figure 5.12c). When the device is folded, the open circuit voltage decreases considerably. "Movie 1" in Supporting Information shows the voltage of the device measured when folded under room lighting. When the device is folded, cracks form in the ITO layer, which reduce the device performance. When the device is unfolded, these cracks are largely healed. The other device layers remain intact upon folding except the ITO layer. Perhaps replacing the ITO layer with alternative flexible transparent conducting electrodes like PEDOT:PSS[40], graphene[41,42], nanowires[43,44] could make the device function even better when folded. It seems like it could be possible to further develop these paper PVs so that they could be folded for transport and unfolded for use.

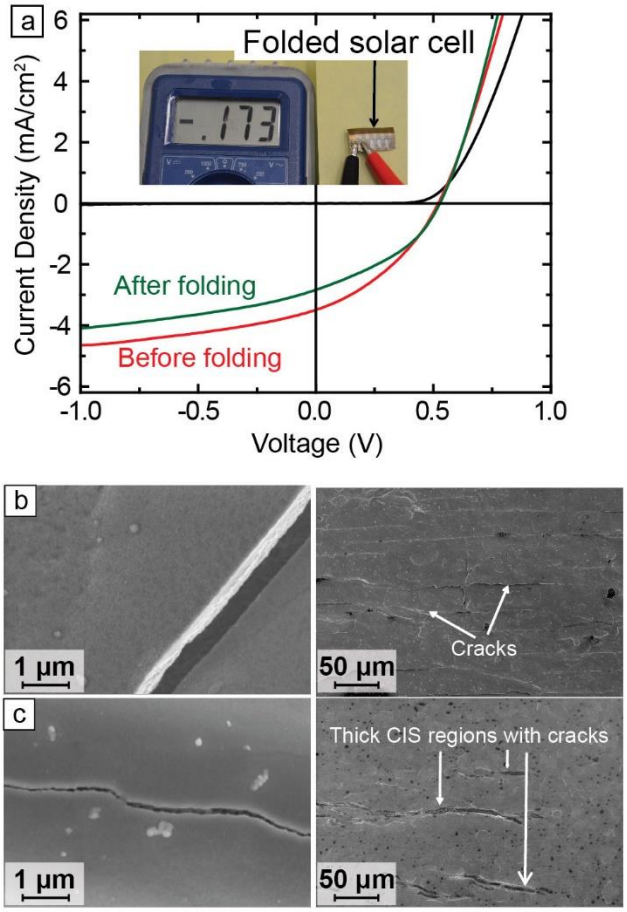


**Figure 5.12:** (a) *J-V* response of the $CuInSe_2$ nanocrystal device on bacterial cellulose shown in the inset before and after folding. (b) SEM images of the ITO layer of a folded $CuInSe_2$ nanocrystal device on bacterial cellulose showing cracks. (c) SEM images of the $CuInSe_2$ nanocrystal layer in a PV device on bacterial cellulose showing cracks in the thick $CuInSe_2$ regions.

### 5.3.4 $CuInSe_2$ Nanocrystal Solar Cell Prototype on Paper to Power an LCD Display

To power electronics, multiple $CuInSe_2$ nanocrystal PV devices can be fabricated and interconnected on bacterial cellulose paper substrates to provide sufficient power.

Figure 5.13a shows the fabrication of ten devices with areas of 0.1 $cm^2$ on a 3"x1" bacterial cellulose substrate. These devices can be electrically connected either in series or parallel depending on the application needs. To demonstrate the manipulation of these devices, they have been cut in the middle as shown in Figure 5.13b into two strips of 5 cells. The ten devices are then connected in series. Figures 5.13c-5.13e show the devices mounted to flat and curved surfaces to power electronic devices. (See the associated Movies 3 and 4 in Supporting Information). Each row of devices delivers 1.5 V under indoor fluorescent lighting, which is close to the expected summation of voltages from the individual devices. The active area of each device is relatively small to provide predictable buildup of voltage (by connecting cells in series) since device shorting is reduced. Both the mechanical flexibility and the ability to power electronics have been demonstrated by sticking the flexible $CuInSe_2$ cellulose devices onto a variety of surfaces including the complex curvature of a water bottle and around a person's wrist. In multiple surface mountings, a calculator was powered and tested to give accurate summations.

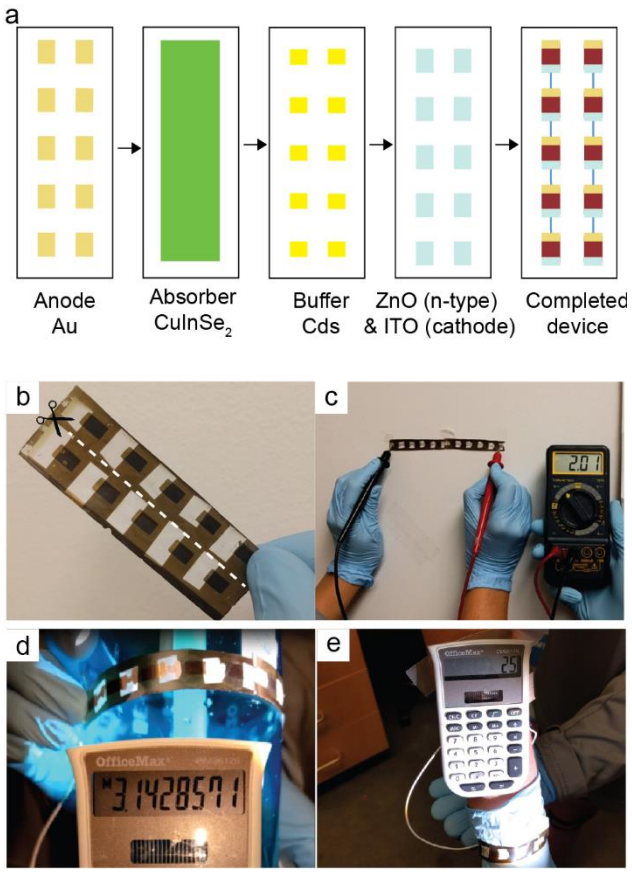


**Figure 5.13:** (a) Schematic showing different layers of the solar cell fabricated starting from the initial gold layer to the completed device. Photographs of (b) 10 $CuInSe_2$ nanocrystal PVs fabricated on bacterial cellulose paper; (c) a strip device with solar cells connected in series and voltage being measured with a voltmeter; (d,e) a $CuInSe_2$ nanocrystal strip device curved around a support powering an LCD screen.

## 5.4 CONCLUSIONS

Several different types of paper were investigated as substrates for nanocrystal-based PVs. Paper made of bacterial nanocellulose was found to be an excellent substrate for nanocrystal solar cells. These devices exhibited the highest efficiencies yet reported for

PVs made directly on paper[10–12] and exhibited significantly greater bending flexibility compared to previously made $CuInSe_2$ and $CuIn_xGa_{(1-x)}Se$ solar cells.[19] Since bacterial cellulose is already used commercially in a variety of other applications, such as a temporary skin in medical care,[45,46] in acoustic diaphragms,[47,48] to make conductive carbon films,[49] and as a separation medium,[50–53] it represents a realistic substrate for making paper PVs. Bacterial cellulose has also been used to make electronic paper displays[54] and as a substrate for light emitting diodes (LEDs).[55,56] Its use as a wound dresser demonstrates its compatibility with the human body, indicating that solar cells on microbial cellulose could be adhered directly to the skin for human body portability and seamless integration into everyday life. The attributes of bacterial cellulose make it suitable for *extreme* integration of electronic devices—not only with the human body—but also in infrastructure, devices and sensors related to the "Internet of Things" and data-mining devices for dynamic field research practices. Furthermore, the fabrication of microbial cellulose is a process that can be semi-portable and enable on-site fabrication of PV cells where the resources of a wet laboratory are available. The process through which these solar cells are fabricated lends itself to development in extremely off-grid sites where the cost of shipment and consequently the weight of the solar cells becomes a limiting factor.

Few materials like paper exist with an ability to maintain a crease when folded and hold its structure—paper can improvise multiple structural configurations, as demonstrated by the practice of origami. Origami has been incorporated into photovoltaic design recently to maximize sunlight absorption using rigid non-foldable silicon devices connected by

serpentine-shaped interconnects.[57] The use of paper PVs could enable greater complexity in such designs since the paper PVs can withstand wrinkles and creases. Paper PVs could be mounted on nearly any type of surface, be it convex, concave or complex. In architectural applications, these PVs could be directly adhered onto walls, enhancing aesthetic building solutions and increasing design options in urban planning. Given that the $CuInSe_2$ nanocrystal layer can be printed,[20,21] the flexibility of these devices allows for paper photovoltaics to function as custom designed PV wallpaper for both interior and exterior applications.

## 5.5 REFERENCES


(1) Miodownik, M. *Stuff Matters: Exploring the Marvelous Materials That Shape Our Manmade World*; Houghton Mifflin Harcourt, New York, U.S.; **2014**.

(2) Lim, W.; Douglas, E. A.; Kim, S.-H.; Norton, D. P.; Pearton, S. J.; Ren, F.; Shen, H.; Chang, W. H. High Mobility $InGaZnO_4$ Thin-Film Transistors on Paper. *Appl. Phys. Lett.* **2009**, *94*, 072103.

(3) Eder, F.; Klauk, H.; Halik, M.; Zschieschang, U.; Schmid, G.; Dehm, C. Organic Electronics on Paper. *Appl. Phys. Lett.* **2004**, *84*, 2673–2675.

(4) Grau, G.; Kitsomboonloha, R.; Swisher, S. L.; Kang, H.; Subramanian, V. Printed Transistors on Paper: Towards Smart Consumer Product Packaging. *Adv. Funct. Mater.* **2014**, *24*, 5067–5074.

(5) Legnani, C.; Vilani, C.; Calil, V. L.; Barud, H. S.; Quirino, W. G.; Achete, C. A.; Ribeiro, S. J. L.; Cremona, M. Bacterial Cellulose Membrane as Flexible Substrate for Organic Light Emitting Devices. *Thin Solid Films* **2008**, *517*, 1016–1020.

(6) Ummartyotin, S.; Juntaro, J.; Sain, M.; Manuspiya, H. Development of Transparent Bacterial Cellulose Nanocomposite Film as Substrate for Flexible Organic Light Emitting Diode (OLED) Display. *Ind. Crops Prod.* **2012**, *35*, 92–97.

(7) Yoon, B.; Ham, D.-Y.; Yarimaga, O.; An, H.; Lee, C. W.; Kim, J.-M. Inkjet Printing of Conjugated Polymer Precursors on Paper Substrates for Colorimetric

Sensing and Flexible Electrothermochromic Display. *Adv. Mater.* **2011**, *23*, 5492–5497.

(8) Martinez, A. W.; Phillips, S. T.; Whitesides, G. M.; Carrilho, E. Diagnostics for the Developing World: Microfluidic Paper-Based Analytical Devices. *Anal. Chem.* **2010**, *82*, 3–10.

(9) Mazzeo, A. D.; Kalb, W. B.; Chan, L.; Killian, M. G.; Bloch, J.-F.; Mazzeo, B. A.; Whitesides, G. M. Paper-Based, Capacitive Touch Pads. *Adv. Mater.* **2012**, *24*, 2850–2856.

(10) Hübler, A.; Trnovec, B.; Zillger, T.; Ali, M.; Wetzold, N.; Mingebach, M.; Wagenpfahl, A.; Deibel, C.; Dyakonov, V. Printed Paper Photovoltaic Cells. *Adv. Energy Mater.* **2011**, *1*, 1018–1022.

(11) Barr, M. C.; Rowehl, J. A.; Lunt, R. R.; Xu, J.; Wang, A.; Boyce, C. M.; Im, S. G.; Bulović, V.; Gleason, K. K. Direct Monolithic Integration of Organic Photovoltaic Circuits on Unmodified Paper. *Adv. Mater.* **2011**, *23*, 3500–3505.

(12) Wang, B.; Kerr, L. L. Dye Sensitized Solar Cells on Paper Substrates. *Sol. Energy Mater. Sol. Cells* **2011**, *95*, 2531–2535.

(13) Hillhouse, H. W.; Beard, M. C. Solar Cells from Colloidal Nanocrystals: Fundamentals, Materials, Devices, and Economics. *Curr. Opin. Colloid Interface Sci.* **2009**, *14*, 245–259.

(14) Gur, I.; Fromer, N. A.; Geier, M. L.; Alivisatos, A. P. Air-Stable All-Inorganic Nanocrystal Solar Cells Processed from Solution. *Science* **2005**, *310*, 462–465.

(15) Kapur, V. K.; Bansal, A.; Le, P.; Asensio, O. I. Non-Vacuum Processing of $CuIn_{1-x}Ga_xSe_2$ Solar Cells on Rigid and Flexible Substrates Using Nanoparticle Precursor Inks. *Thin Solid Films* **2003**, *431*, 53–57.

(16) Reinhard, P.; Chirila, A.; Blosch, P.; Pianezzi, F.; Nishiwaki, S.; Buechelers, S.; Tiwari, A. N. Review of Progress toward 20% Efficiency Flexible CIGS Solar Cells and Manufacturing Issues of Solar Modules. *Photovolt. IEEE J.* **2013**, *3*, 572–580.

(17) Kessler, F.; Herz, K.; Powalla, M.; Hartmann, M.; Schmidt, M.; Jasenek, A.; Schock, H. W. Flexible and Monolithically Integrated CIGS-Modules. *MRS Proceedings*; Cambridge Univ Press, **2001**; Vol. 668, pp. H3–H6.

(18) Herrmann, D.; Kessler, F.; Herz, K.; Powalla, M.; Schulz, A.; Schneider, J.; Schumacher, U. High-Performance Barrier Layers for Flexible CIGS Thin-Film Solar Cells on Metal Foils. *MRS Proceedings*; Cambridge Univ Press, **2003**; Vol. 763, pp. B6–B10.

(19) Chirilă, A.; Buecheler, S.; Pianezzi, F.; Bloesch, P.; Gretener, C.; Uhl, A. R.; Fella, C.; Kranz, L.; Perrenoud, J.; Seyrling, S.; *et al.* Highly Efficient Cu (In, Ga) $Se_2$ Solar Cells Grown on Flexible Polymer Films. *Nature Mater.* **2011**, *10*, 857–861.

(20) Akhavan, V. A.; Panthani, M. G.; Goodfellow, B. W.; Reid, D. K.; Korgel, B. A. Thickness-Limited Performance of CuInSe2 Nanocrystal Photovoltaic Devices. Opt. Express 2010, 18, A411.

(21) Panthani, M. G.; Stolle, C. J.; Reid, D. K.; Rhee, D. J.; Harvey, T. B.; Akhavan, V. A.; Yu, Y.; Korgel, B. A. $CuInSe_2$ Quantum Dot Solar Cells with High Open-Circuit Voltage. J. Phys. Chem. Lett. 2013, 4, 2030–2034.

(22) Brown, R. M.; Willison, J. H.; Richardson, C. L. Cellulose Biosynthesis in Acetobacter Xylinum: Visualization of the Site of Synthesis and Direct Measurement of the in Vivo Process. *Proc. Natl. Acad. Sci. U. S. A.* **1976**, *73*, 4565–4569.

(23) Haigler, C. H.; White, A. R.; Brown, R. M.; Cooper, K. M. Alteration of in Vivo Cellulose Ribbon Assembly by Carboxymethylcellulose and Other Cellulose Derivatives. *J. Cell Biol.* **1982**, *94*, 64–69.

(24) Hesse, S.; Kondo, T. Behavior of Cellulose Production of Acetobacter Xylinum in 13 C-Enriched Cultivation Media Including Movements on Nematic Ordered Cellulose Templates. *Carbohydr. Polym.* **2005**, *60*, 457–465.

(25) Nishi, Y.; Uryu, M.; Yamanaka, S.; Watanabe, K.; Kitamura, N.; Iguchi, M.; Mitsuhashi, S. The Structure and Mechanical Properties of Sheets Prepared from Bacterial Cellulose. *J. Mater. Sci.* **1990**, *25*, 2997–3001.

(26) McCandless, B. E.; Shafarman, W. N. *Chemical Surface Deposition of Ultra-Thin Semiconductors*; Google Patents, 2003.

(27) Ververis, C.; Georghiou, K.; Christodoulakis, N.; Santas, P.; Santas, R. Fiber Dimensions, Lignin and Cellulose Content of Various Plant Materials and Their Suitability for Paper Production. *Ind. Crops Prod.* **2004**, *19*, 245–254.

(28) Rau, U.; Braunger, D.; Herberholz, R; Schock, H. W.; Guillemoles, J. F., Kronik, L., & Cahen, D. Oxygenation and air-annealing effects on the electronic properties of Cu(In,Ga)$Se_2$ films and devices. *Journal of Applied Physics*, **1999**, *86(1)*, 497-505.

(29) Leonat, L.; White, M. S.; Głowacki, E. D.; Scharber, M. C.; Zillger, T.; Rühling, J.; Hübler, A.; Sariciftci, N. S. 4% Efficient Polymer Solar Cells on Paper Substrates. *J. Phys. Chem. C* **2014**, *118*, 16813–16817.

(30) Fatemi, N. S.; Pollard, H. E.; Hou, H. Q.; Sharps, P. R. Solar Array Trades between Very High-Efficiency Multi-Junction and Si Space Solar Cells. In *Conference*

*Record of the Twenty-Eighth IEEE Photovoltaic Specialists Conference,* **2000**; pp. 1083–1086.

(31) Gaynor, W.; Burkhard, G. F.; McGehee, M. D.; Peumans, P. Smooth Nanowire/Polymer Composite Transparent Electrodes. *Adv. Mater.* **2011**, *23*, 2905–2910.

(32) Kumar, A.; Zhou, C. The Race to Replace Tin-Doped Indium Oxide: Which Material Will Win? *ACS Nano* **2010**, *4*, 11–14.

(33) Wu, H.; Hu, L.; Rowell, M. W.; Kong, D.; Cha, J. J.; McDonough, J. R.; Zhu, J.; Yang, Y.; McGehee, M. D.; Cui, Y. Electrospun Metal Nanofiber Webs as High-Performance Transparent Electrode. *Nano Lett.* **2010**, *10*, 4242–4248.

(34) Rowell, M. W.; Topinka, M. A.; McGehee, M. D.; Prall, H.-J.; Dennler, G.; Sariciftci, N. S.; Hu, L.; Gruner, G. Organic Solar Cells with Carbon Nanotube Network Electrodes. *Appl. Phys. Lett.* **2006**, *88*, 233506.

(35) Lin, Q.; Huang, H.; Jing, Y.; Fu, H.; Chang, P.; Li, D.; Yao, Y.; Fan, Z. Flexible Photovoltaic Technologies. *J. Mater. Chem. C* **2014**, *2*, 1233.

(36) Kaltenbrunner, M.; White, M. S.; G lowacki, E. D.; Sekitani, T.; Someya, T.; Sariciftci, N. S.; Bauer, S. Ultrathin and Lightweight Organic Solar Cells with High Flexibility. *Nat. Commun.* **2012**, *3*, 770.

(37) Seshan, C. Cell Efficiency Dependence on Solar Incidence Angle. In *2010 35th IEEE Photovoltaic Specialists Conference (PVSC)*; **2010**; pp. 002102–002105.

(38) Tvingstedt, K.; Andersson, V.; Zhang, F.; Inganäs, O. Folded Reflective Tandem Polymer Solar Cell Doubles Efficiency. *Appl. Phys. Lett.* **2007**, *91*, 123514.

(39) Zhou, Y.; Zhang, F.; Tvingstedt, K.; Tian, W.; Inganäs, O. Multifolded Polymer Solar Cells on Flexible Substrates. *Appl. Phys. Lett.* **2008**, *93*, 033302.

(40) Vosgueritchian, M.; Lipomi, D. J.; Bao, Z. Highly Conductive and Transparent PEDOT:PSS Films with a Fluorosurfactant for Stretchable and Flexible Transparent Electrodes. *Adv. Funct. Mater.* **2012**, *22*, 421–428.

(41) Bae, S.; Kim, H.; Lee, Y.; Xu, X.; Park, J.-S.; Zheng, Y.; Balakrishnan, J.; Lei, T.; Ri Kim, H.; Song, Y. I.; *et al.* Roll-to-Roll Production of 30-Inch Graphene Films for Transparent Electrodes. *Nat. Nanotechnol.* **2010**, *5*, 574–578.

(42) Li, X.; Zhu, Y.; Cai, W.; Borysiak, M.; Han, B.; Chen, D.; Piner, R. D.; Colombo, L.; Ruoff, R. S. Transfer of Large-Area Graphene Films for High-Performance Transparent Conductive Electrodes. *Nano Lett.* **2009**, *9*, 4359–4363.

(43) Rathmell, A. R.; Wiley, B. J. The Synthesis and Coating of Long, Thin Copper Nanowires to Make Flexible, Transparent Conducting Films on Plastic Substrates. *Adv. Mater.* **2011**, *23*, 4798–4803.

(44) De, S.; Higgins, T. M.; Lyons, P. E.; Doherty, E. M.; Nirmalraj, P. N.; Blau, W. J.; Boland, J. J.; Coleman, J. N. Silver Nanowire Networks as Flexible, Transparent, Conducting Films: Extremely High DC to Optical Conductivity Ratios. *ACS Nano* **2009**, *3*, 1767–1774.

(45) Fontana, J. D.; De Souza, A. M.; Fontana, C. K.; Torriani, I. L.; Moreschi, J. C.; Gallotti, B. J.; De Souza, S. J.; Narcisco, G. P.; Bichara, J. A.; Farah, L. F. X. Acetobacter Cellulose Pellicle as a Temporary Skin Substitute. *Appl. Biochem. Biotechnol.* **1990**, *24*, 253–264.

(46) Czaja, W.; Krystynowicz, A.; Bielecki, S.; Brown Jr., R. M. Microbial Cellulose—the Natural Power to Heal Wounds. *Biomaterials* **2006**, *27*, 145–151.

(47) Iguchi, M.; Yamanaka, S.; Budhiono, A. Bacterial Cellulose—a Masterpiece of Nature's Arts. *J. Mater. Sci.* **2000**, *35*, 261–270.

(48) Nishi, Y.; Uryu, M.; Yamanaka, S.; Watanabe, K.; Kitamura, N.; Iguchi, M.; Mitsuhashi, S. The Structure and Mechanical Properties of Sheets Prepared from Bacterial Cellulose. *J. Mater. Sci.* **1990**, *25*, 2997–3001.

(49) Yoshino, K.; Matsuoka, R.; Nogami, K.; Yamanaka, S.; Watanabe, K.; Takahashi, M.; Honma, M. Graphite Film Prepared by Pyrolysis of Bacterial Cellulose. *J. Appl. Phys.* **1990**, *68*, 1720–1725.

(50) Shibazaki, H.; Kuga, S.; Onabe, F.; Usuda, M. Bacterial Cellulose Membrane as Separation Medium. *J. Appl. Polym. Sci.* **1993**, *50*, 965–969.

(51) Dubey, V.; Pandey, L. K.; Saxena, C. Pervaporative Separation of Ethanol/water Azeotrope Using a Novel Chitosan-Impregnated Bacterial Cellulose Membrane and Chitosan–poly(vinyl Alcohol) Blends. *J. Membr. Sci.* **2005**, *251*, 131–136.

(52) Choi, Y.-J.; Ahn, Y.; Kang, M.-S.; Jun, H.-K.; Kim, I. S.; Moon, S.-H. Preparation and Characterization of Acrylic Acid-Treated Bacterial Cellulose Cation-Exchange Membrane. *J. Chem. Technol. Biotechnol.* **2004**, *79*, 79–84.

(53) Dubey, V.; Saxena, C.; Singh, L.; Ramana, K. V.; Chauhan, R. S. Pervaporation of Binary Water–ethanol Mixtures through Bacterial Cellulose Membrane. *Sep. Purif. Technol.* **2002**, *27*, 163–171.

(54) Shah, J.; Jr, R. M. B. Towards Electronic Paper Displays Made from Microbial Cellulose. *Appl. Microbiol. Biotechnol.* **2004**, *66*, 352–355.

(55) Legnani, C.; Vilani, C.; Calil, V. L.; Barud, H. S.; Quirino, W. G.; Achete, C. A.; Ribeiro, S. J. L.; Cremona, M. Bacterial Cellulose Membrane as Flexible Substrate for Organic Light Emitting Devices. *Thin Solid Films* **2008**, *517*, 1016–1020.

(56) Yano, H.; Sugiyama, J.; Nakagaito, A. N.; Nogi, M.; Matsuura, T.; Hikita, M.; Handa, K. Optically Transparent Composites Reinforced with Networks of Bacterial Nanofibers. *Adv. Mater.* **2005**, *17*, 153–155.

(57) Tang, R.; Huang, H.; Tu, H.; Liang, H.; Liang, M.; Song, Z.; Xu, Y.; Jiang, H.; Yu, H. Origami-Enabled Deformable Silicon Solar Cells. *Appl. Phys. Lett.* **2014**, *104*, 083501.

# Chapter 6: Large Area $CuInSe_2$ Nanocrystal Solar Cells

## 6.1 INTRODUCTION

Internet of Things (IoT) has been growing tremendously in recent years. IoT doesn't just encompass personal computers and mobile phones connected through the internet, but also encompasses billons of other devices that are interconnected, constantly communicating, and transmitting useful information through the internet or other wireless technologies. These devices are typically sensors, which are responsive to changes in pressure, temperature, humidity, gas, position, flowrate, etc.

The rapid Internet of Things (IoT) growth is projected to reach 20.4 billion devices in use by 2020.[1] The challenge is to find an inexpensive, portable power source that can deliver multiple years of unattended operation to these billions of sensors. Their power cannot be supplied through power cords because the location of these sensors is usually in remote places. Thus, a portable power source, such as a battery will be required, but batteries are not a viable option due to their cost, maintenance, and, in some cases, their incompatible size with the IoT device. An attractive solution to this portable power problem in a typically small sized IoT device is a lightweight, flexible solar cell.

With the current developments on IoT sensors, they now require very low power and most are voltage driven.[2,3] Solar cells manufactured by traditional vacuum-based, high temperature processes can have significantly high efficiencies, but are rigid and might be too expensive for these applications. Many IoT devices do not require such high efficiency. Thus, a more fitting solution to this problem is to use solar cells fabricated at mild

processing temperatures and ambient pressures by solution processable, roll-to-roll techniques that are less expensive.[4,5]

Amongst the various solution processable solar cell technologies, nanocrystal solar cells have higher stability, which makes them the ideal choice for the IoT device power supply. Their stability enables them to operate for over a decade without maintenance. Even though nanocrystal solar cells cannot generate currents as high as traditional Si and thin film solar cells, the voltages they produce are sufficient to power the IoT devices.

Herein, we report a processing paradigm to fabricate a $CuInSe_2$ nanocrystal micro grid solar cell system that provides the IoT-required amount of voltage and current. Typically, the voltage needed for IoT devices, like beacons, is 1.8 V to 3.6 V, and the current required ranges from µA to a few mA.[6]

## 6.2 EXPERIMENTAL DETAILS

### 6.2.1 Chemicals

Copper (I) chloride (CuCl, 99.99%), elemental selenium (Se, 99.99%), cadmium sulfate (CdSO4, 99.99%), thiourea (99%), diphenylphosphine (DPP), tributylphosphine (TBP), oleylamine (70%), anhydrous toluene (99.8%) and anhydrous ethanol (99.5%), were obtained from Aldrich; indium (III) chloride (InCl3, 99.99%) was obtained from Strem Chemical; toluene, ethanol, hexanes, and ammonium hydroxide (18M $NH_4OH$) were obtained from Fisher Scientific. Oleylamine was degassed by pulling vacuum overnight at ~200 mTorr at 110 °C and stored in an $N_2$ filled glovebox before use.

### 6.2.2 $CuInSe_2$ Nanocrystal Synthesis

$CuInSe_2$ nanocrystals were synthesized as previously described.[7] In a typical reaction, 5 mmol of CuCl, 5 mmol of $InCl_3$, 1.5 ml of DPP, and 50 ml of degassed oleylamine are added to a 100 ml three neck flask inside an $N_2$ filled glovebox. The flask is attached to a standard Schlenk line and degassed at 110 °C under vacuum for 30 minutes. The flask is then filled with nitrogen held at 100 ºC for 10 minutes. The flask and its contents are then heated to 240 °C. When the temperature reaches 180 ºC, a solution of 10 mmol Se in 10 ml of TBP is rapidly injected into the reaction mixture and the temperature is allowed to rise to 240 ºC. After 10 min, the heating mantle is removed and the reaction is allowed to cool to room temperature. The nanocrystals are washed via centrifugation using toluene and ethanol as the solvent and anti-solvent, respectively. The final nanocrystals dispersion is then transferred to a nitrogen filled glovebox.

### 6.2.3 $CuInSe_2$ Nanocrystal Device Fabrication

$CuInSe_2$ nanocrystal PVs were fabricated with a Au/CIS/CdS/i-ZnO/indium tin oxide (ITO) device structure. A 5-nm layer of chromium followed by 60 nm of gold were thermally evaporated onto polyethylene terephthalate (PET) substrate that is adhered to glass substrate for support. Films of $CuInSe_2$ nanocrystals were then deposited on to the gold layer. Oleylamine-capped nanocrystals diluted to 10 mg/ml in toluene were spray deposited at room temperature onto substrates heated to 100 °C using a Sonotek ExactaCoat ultrasonic automated spray system equipped with a 120 kHz ultrasonic nozzle. The spray nozzle was rastered across a rectangular area with 3 mm raster spacing, a speed of 10 mm/sec, an ink injection rate of 0.1 mL/min, an air pressure of 1.6 psi, and a nozzle-

to-substrate separation of 11.5 cm. A CdS buffer layer was deposited by drop casting 0.7 mL of a CdS precursor solution (1.25 ml of 15 mM $CdSO_4$, 2.2 ml of 1.5 M thiourea, and 2.8 ml of 18 M $NH_4OH$ in water) onto the $CuInSe_2$ nanocrystal film heated to 90 °C on a hot plate and covered with an inverted petri dish for 2 min.[8] The substrate was removed from the hot plate, rinsed with DI water, and dried with a stream of compressed air. Top layers of i-ZnO and ITO were deposited by RF sputtering from a ZnO target (Lesker, 99.9%) in a 0.5% $O_2$ in Ar atmosphere (Praxair, 99.95%) and a ITO target (Lesker, 99.99% $In_2O_3$:$SnO_2$ 90:10) in Ar atmosphere (Praxair, research grade). ZnO and ITO are deposited selectively certain regions using 3D printed masks. Silver paint was applied for electrical contact to the devices. The patterning of the device layers is adopted according to the need of the application. Figure 6.1 shows one of the large area devices fabricated. The patterns of different layers shown in figure 6.1 is achieved by shadow masking using 3-D printed masks. 3-D printing the masks allows for rapid prototyping and development of microgrid PVs of various power outputs. We define microgrid system as a network of interconnected small PVs (area of around 0.1 $cm^2$) that are referred to as pixel devices. The prototype shown in figure 6.1 has 60 pixel devices and the layers are deposited in such a way that the 10 pixel solar cells in each column have a connected gold back contact and a separate ITO top contact. The pixel devices in each column can be connected in parallel to have a current addition. Then the six columns of parallelly connected solar cells can in turn be connected in series to achieve a voltage addition. We have used silver paint to connect the devices as

necessary but, once again, a 3-D printed shadow mask can be created and a conductive metal-like silver or copper can be evaporated in the desired locations.

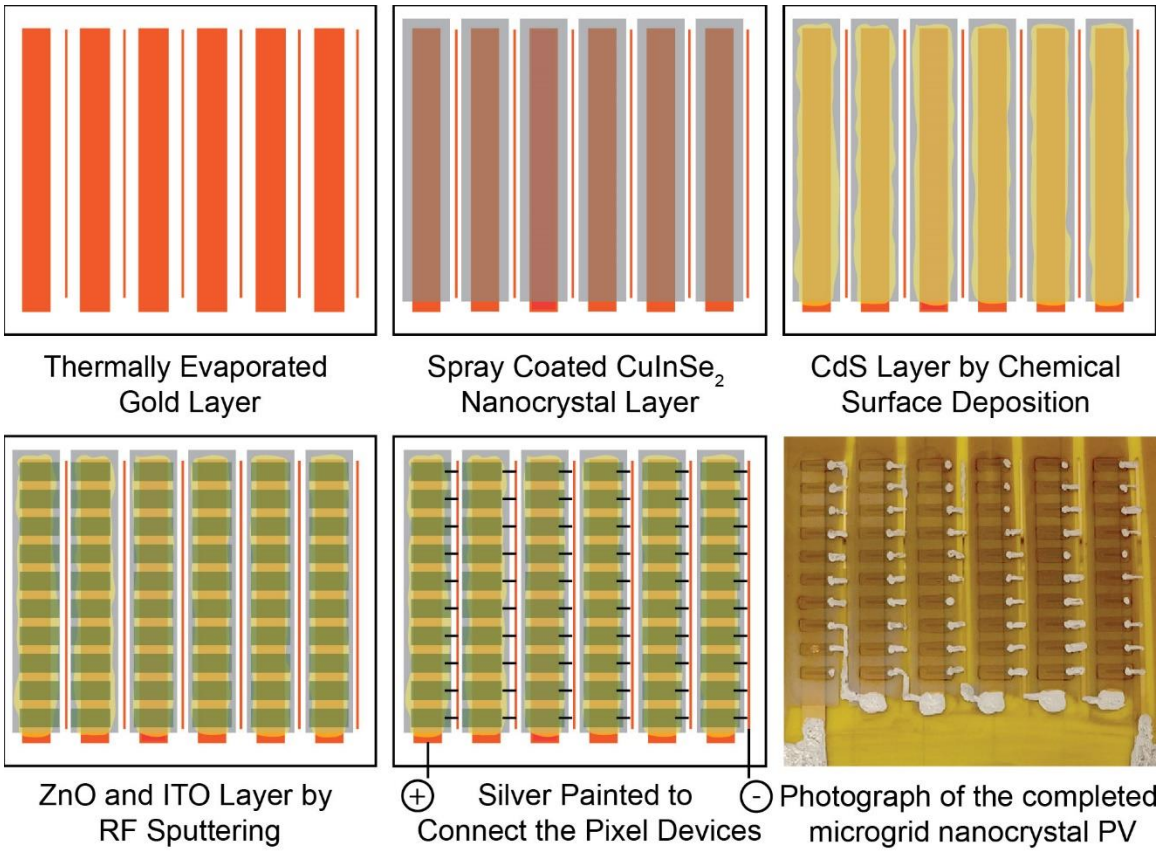


**Figure 6.1:** Illustration showing the patterning of various device layers

PV device response was measured using a Keithley 2400 General Purpose Sourcemeter under solar simulation using a Newport Xenon Lamp Solar Simulator with an AM 1.5 filter. Incident photon conversion efficiency (IPCE) was measured using a home-built device with lock-in amplifier (Stanford Research Systems, model SR830) and monochromator (Newport Cornerstone 260 1/4M), and calibrated with Si and Ge photodiodes (Hamamatsu).

## 6.3 RESULTS AND DISCUSSIONS

### 6.3.1 Device performance

A color coded plot of the maximum power points of each pixel device is shown in figure 6.2. Color coded plots with numerical values overlapped, for the maximum power point, open circuit voltage, fill factor, and power conversion efficiency are shown in figure 6.3. There is a greater chance of device failure when the device area is large, so the area of each pixel device was chosen to be around 0.1 $cm^2$. The pixel devices are connected using silver paint in parallel to have current addition and in series to have voltage addition. As seen in figure 6.2, some devices have very low power output. This is due to the failure of the pixel device. Such devices are omitted from being connected to the other pixel devices to prevent them from affecting the whole microgrid. This ability to disconnect failing devices is one of the most important benefits of a micro grid system. When a single nanocrystal solar cell is fabricated on the whole area instead of building numerous pixel devices, the efficiency will be limited to the lowest efficiency pixel device.

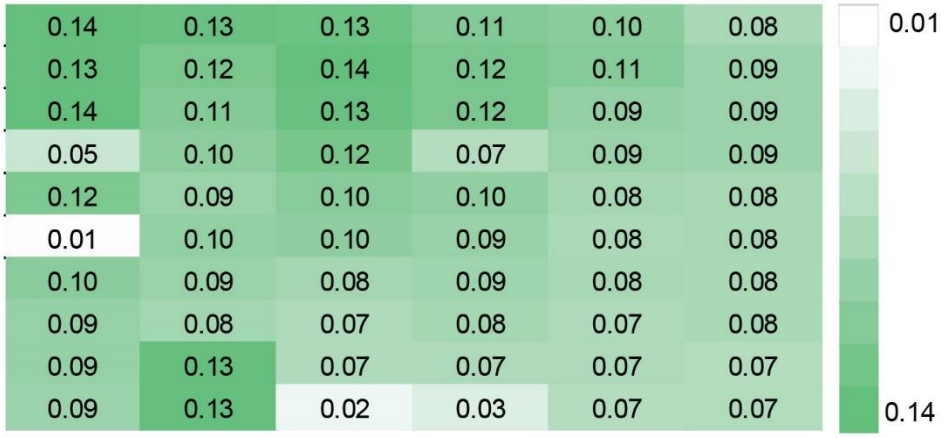


**Figure 6.2:** Color coded plot showing the maximum power output in milliwatts for the prototype device shown in figure 6.1 under AM1.5G illumination (100mW/$cm^2$)


**Figure 6.3:** Color coded plots showing (a) power conversion efficiency, (b) short circuit current density, (c) open circuit voltage, and (d) fill factor of each pixel device of the $CuInSe_2$ nanocrystal prototype solar cell shown in figure 6.1 under AM1.5G illumination (100mW/cm$^2$)

### 6.3.2 Performance on connecting pixel devices

To reduce the number of steps in device fabrication and automate the process of connecting the pixel solar cells, the patterning is designed in such a way that the ITO and Au layers between adjacent devices can be connected without silver paint. Figure 6.4 shows such a prototype device. The IV characteristics of a single row of devices connected in series are shown in figure 6.4c and the IV characteristics after the three rows are connected in parallel are shown in figure 6.4d. It can be seen from the figure that no loss in power conversion efficiency is noted after the rows are connected. Also, the current obtained after

the three rows are connected is roughly thrice the amount of current obtained from a single row of devices, proving that there is no significant loss of current due to connecting them.

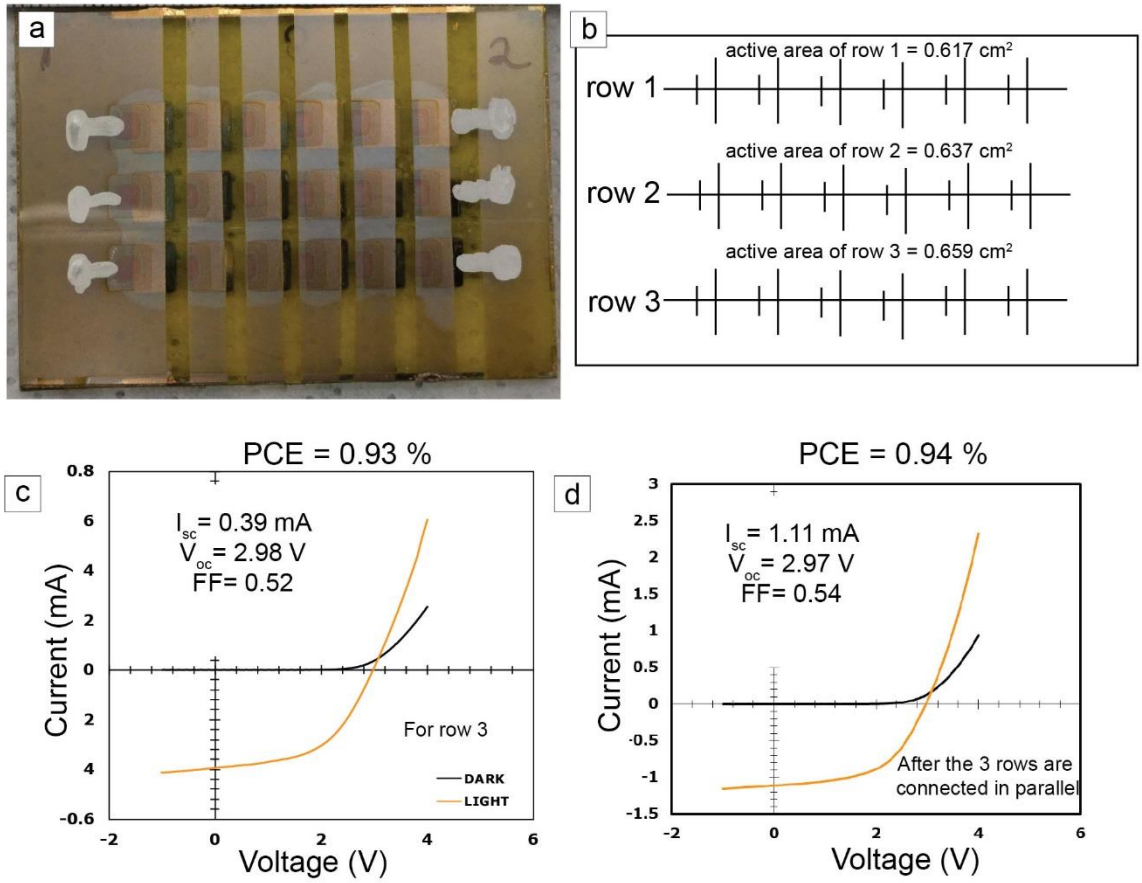


**Figure 6.4:** (a) Photograph of a microgrid $CuInSe_2$ nanocrystal solar cell (b) illustration showing the connections of prototype device shown in (a). (c) IV curve of row 3 of prototype shown in (a). (d) IV curve of the prototype shown in (a) after the three device rows are connected in parallel. IV curves are measured under AM1.5G illumination (100mW/cm$^2$)

## 6.4 CONCLUSIONS

Fabricating a microgrid solar cell system for $CuInSe_2$ nanocrystal solar cells has been discussed. After the pixel devices are connected, no loss in performance has been

observed. Work is required to further improve the design from that shown in figure 6.1 that has an active area of only 20%. These further design improvements will increase the active area and thus increase the power output from the device.

## 6.5 REFERENCES


(1) Gartner Says 8.4 Billion Connected "Things" Will Be in Use in 2017, Up 31 Percent From 2016 http://www.gartner.com/newsroom/id/3598917

(2) Dementyev, A.; Hodges, S.; Taylor, S.; Smith, J. Power Consumption Analysis of Bluetooth Low Energy, ZigBee and ANT Sensor Nodes in a Cyclic Sleep Scenario. In *2013 IEEE International Wireless Symposium (IWS)*; 2013; pp. 1–4.

(3) Gomez, C.; Oller, J.; Paradells, J. Overview and Evaluation of Bluetooth Low Energy: An Emerging Low-Power Wireless Technology. *Sensors* **2012**, *12*, 11734–11753.

(4) Krebs, F. C. Fabrication and Processing of Polymer Solar Cells: A Review of Printing and Coating Techniques. *Sol. Energy Mater. Sol. Cells* **2009**, *93*, 394–412.

(5) Pagliaro, M.; Ciriminna, R.; Palmisano, G. Flexible Solar Cells. *ChemSusChem* **2008**, *1*, 880–891.

(6) Systems, eZ. nRF51822 / Bluetooth low energy / Products / Home - Ultra Low Power Wireless Solutions from NORDIC SEMICONDUCTOR https://www.nordicsemi.com/eng/Products/Bluetooth-low-energy/nRF51822

(7) Voggu, V. R.; Sham, J.; Pfeffer, S.; Pate, J.; Fillip, L.; Harvey, T. B.; Brown, R. M.; Korgel, B. A. Flexible $CuInSe_2$ Nanocrystal Solar Cells on Paper. *ACS Energy Lett.* **2017**, *2*, 574–581.

(8) McCandless, B. E.; Shafarman, W. N. Chemical Surface Deposition of Ultra-Thin Semiconductors. US6537845 B1, March 25, 2003.

# Chapter 7: Conclusions and Future Direction

## 7.1 CONCLUSIONS

The use of semiconductor nanocrystals as an absorbing material in solar cells is a promising route to making cheap photovoltaics. Low-temperature (<200 ºC) spray-coated $CuInSe_2$ nanocrystals have been fabricated with a device efficiency of 3.1 %, in 2010.[1] Since then, no improvement in device efficiency has been achieved for $CuInSe_2$ nanocrystal solar cells. In contrast, a similar nanocrystal solar cell technology, employing PbS nanocrystals instead of $CuInSe_2$ nanocrystals, experienced improvements in device efficiency. With ligand engineering, the efficiency of PbS nanocrystal solar cells has improved to as high as 10.9%.[2] Though only a few similar strategies have been applied to $CuInSe_2$ nanocrystal solar cells, none of the tested ligands resulted in an increase in power conversion efficiency (PCE) greater than 3.1%.[3] In the work reported, a device efficiency improvement through ligand engineering using ammonium sulfide is achieved. Hopefully, future ligand exchange research on $CuInSe_2$ nanocrystals continue and lead to further improvement in device efficiency.

Apart from efficiency improvements, developments were made on other aspects of $CuInSe_2$ nanocrystal solar cells, including development of cheaper fabrication methods, use of cheaper substrates, improvement in $CuInSe_2$ nanocrystal reaction yield, and design of large area nanocrystal solar cells.

### 7.1.1 Ligand Engineering of $CuInSe_2$ Nanocrystals

A solid-state ligand exchange was performed on the CuInSe2 nanocrystals leading to the replacement of long chain organic molecules with shorter sulfide ions. This resulted in an improvement in charge transfer between nanocrystals and an increase in short circuit

current. Overall, this ligand engineering caused an increase in power conversion efficiency to 3.5% from a previous best of 3.1%.

### 7.1.2 Reduction in Manufacturing and Processing Costs

$CuInSe_2$ nanocrystals synthesized by several methods were used in photovoltaics to optimize performance. A crucial observation from these experiments was that diphenylphosphine improves reaction yield and tributylphosphine improves device performance. By using both reagents in a single reaction, a high yield synthesis method with device efficiencies over 3% is achieved. Such improvements in reaction yield results in reduction of material costs as less precursor materials will be needed to produce the desired quantity of $CuInSe_2$ nanocrystals.

To further reduce manufacturing costs, nanocrystals devices were fabricated on paper. This not only reduces the manufacturing costs, as paper is cheap, but also installation and transportation costs, due to the ease of handling and reduced weight. The $CuInSe_2$ nanocrystal paper solar cells demonstrated extreme flexibility, potentially allowing them to adhere on any kind of surface.[4] This will lead to deeper market penetration of solar energy into places where heavy, rigid solar panels cannot be used.

Processing costs have further been reduced by replacing high temperature, vacuum processed layers, with solution processed layers. Solution processed layers can be deposited by techniques such as spray coating, spin coating, screen printing etc. that do not need high temperature or vacuum.[5] This will result in reduced production costs.

### 7.1.3 Scale up of $CuInSe_2$ Nanocrystal Solar Cells

For semiconductor nanocrystal solar cells to enter the market, the devices need to be scaled up in area to provide the required power output. A rapid fabrication process has been developed to build multiple solar cells on a single substrate. This was achieved by using 3D printed masks. 3D printing the custom designed masks enables fabrication of solar cells at a rapid pace. Such easy fabrication of custom designed PVs will promote the use of solar energy in new application areas.

## 7.2 FUTURE DIRECTIONS

Better control of shape and size is needed for $CuInSe_2$ nanocrystals. Control of shape and size is very important because the properties of nanocrystals are highly dependent on their dimensions.[6–9] Better control of the band alignment can be achieved through improved nanocrystal uniformity, achieved by size-selective precipitation[10] or finding the optimal reaction conditions, which may result in better device performance.

Initial improvement of the device efficiency of $CuInSe_2$ nanocrystal solar cells with ligand exchange has been achieved. This was possible with the use of ammonium sulfide. There are numerous other ligands that have improved device efficiency in other nanocrystal systems.[11–15] Exploring these other ligands might lead to improvement in $CuInSe_2$ device efficiency.

Less expensive processes like photonic curing can be used to improve the nanocrystal device performance by sintering.[16] Photonic curing uses a rapid pulse of broad band light. A great deal of work has been done on sintering the $CuInSe_2$ nanocrystal layer in solar cells using photonic curing, but an increase in PCE was not achieved. Melt ball formations caused exposed back contacts and led to low device efficiency. To prevent this,

low pulse energies are used to strip the ligands without melting and sintering the nanocrystals. This led to an increase in short circuit current, but the device efficiency was still low due to the loss in open circuit voltage.[17] If the nanocrystal layer could be passivated with shorter ligands after stripping oleylamine, the loss in open circuit voltage could be curtailed and lead to improvements in efficiency.

The commercialization of $CuInSe_2$ nanocrystal solar cells is also challenged using expensive gold as a back contact. Gold has a very high work function which is best suited for these devices. Other high cheap work function metals like nickel can be explored to replace gold. The use of a thin layer of high work function molybdenum oxide on nickel has been explored in CdTe solar cells which showed promising results.[18] Similar strategies should be applied to replace the gold layer in $CuInSe_2$ nanocrystal solar cells.

## 7.3 REFERENCES


(1) Akhavan, V. A.; Panthani, M. G.; Goodfellow, B. W.; Reid, D. K.; Korgel, B. A. Thickness-Limited Performance of $CuInSe_2$ Nanocrystal Photovoltaic Devices. *Opt. Express* **2010**, *18*, A411.

(2) Jo, J. W.; Kim, Y.; Choi, J.; de Arquer, F. P. G.; Walters, G.; Sun, B.; Ouellette, O.; Kim, J.; Proppe, A. H.; Quintero-Bermudez, R.; *et al.* Enhanced Open-Circuit Voltage in Colloidal Quantum Dot Photovoltaics via Reactivity-Controlled Solution-Phase Ligand Exchange. *Adv. Mater.1703627.*

(3) Stolle, C. J.; Panthani, M. G.; Harvey, T. B.; Akhavan, V. A.; Korgel, B. A. Comparison of the Photovoltaic Response of Oleylamine and Inorganic Ligand-Capped $CuInSe_2$ Nanocrystals. *ACS Appl. Mater. Interfaces* **2012**, *4*, 2757–2761.

(4) Voggu, V. R.; Sham, J.; Pfeffer, S.; Pate, J.; Fillip, L.; Harvey, T. B.; Brown, R. M.; Korgel, B. A. Flexible $CuInSe_2$ Nanocrystal Solar Cells on Paper. *ACS Energy Lett.* **2017**, *2*, 574–581.

(5) Guo, Q.; Kim, S. J.; Kar, M.; Shafarman, W. N.; Birkmire, R. W.; Stach, E. A.; Agrawal, R.; Hillhouse, H. W. Development of $CuInSe_2$ Nanocrystal and Nanoring Inks for Low-Cost Solar Cells. *Nano Lett.* **2008**, *8*, 2982–2987.

(6) Alivisatos, A. P. Semiconductor Clusters, Nanocrystals, and Quantum Dots. *Science* **1996**, *271*, 933–937.

(7) Nirmal, M.; Brus, L. Luminescence Photophysics in Semiconductor Nanocrystals. *Acc. Chem. Res.* **1999**, *32*, 407–414.

(8) Sun, S.; Murray, C. B.; Weller, D.; Folks, L.; Moser, A. Monodisperse FePt Nanoparticles and Ferromagnetic FePt Nanocrystal Superlattices. *Science* **2000**, *287*, 1989–1992.

(9) Speliotis, D. Magnetic Recording beyond the First 100 Years. *J. Magn. Magn. Mater.* **1999**, *193*, 29–35.

(10) Yu, Y.; Bosoy, C. A.; Hessel, C. M.; Smilgies, D.-M.; Korgel, B. A. Silicon Nanocrystal Superlattices. *ChemPhysChem* **2013**, *14*, 84–87.

(11) Tang, J.; Kemp, K. W.; Hoogland, S.; Jeong, K. S.; Liu, H.; Levina, L.; Furukawa, M.; Wang, X.; Debnath, R.; Cha, D.; *et al.* Colloidal-Quantum-Dot Photovoltaics Using Atomic-Ligand Passivation. *Nat. Mater.* **2011**, *10*, 765–771.

(12) Chuang, C.-H. M.; Brown, P. R.; Bulović, V.; Bawendi, M. G. Improved Performance and Stability in Quantum Dot Solar Cells through Band Alignment Engineering. *Nat. Mater.* **2014**, *13*, 796–801.

(13) Barkhouse, D. A. R.; Pattantyus-Abraham, A. G.; Levina, L.; Sargent, E. H. Thiols Passivate Recombination Centers in Colloidal Quantum Dots Leading to Enhanced Photovoltaic Device Efficiency. *ACS Nano* **2008**, *2*, 2356–2362.

(14) Koleilat, G. I.; Levina, L.; Shukla, H.; Myrskog, S. H.; Hinds, S.; Pattantyus-Abraham, A. G.; Sargent, E. H. Efficient, Stable Infrared Photovoltaics Based on Solution-Cast Colloidal Quantum Dots. *ACS Nano* **2008**, *2*, 833–840.

(15) Pattantyus-Abraham, A. G.; Kramer, I. J.; Barkhouse, A. R.; Wang, X.; Konstantatos, G.; Debnath, R.; Levina, L.; Raabe, I.; Nazeeruddin, M. K.; Grätzel, M.; *et al.* Depleted-Heterojunction Colloidal Quantum Dot Solar Cells. *ACS Nano* **2010**, *4*, 3374–3380.

(16) Das, S.; Yang, B.; Gu, G.; Joshi, P. C.; Ivanov, I. N.; Rouleau, C. M.; Aytug, T.; Geohegan, D. B.; Xiao, K. High-Performance Flexible Perovskite Solar Cells by Using a Combination of Ultrasonic Spray-Coating and Low Thermal Budget Photonic Curing. *ACS Photonics* **2015**, *2*, 680–686.

(17) Stolle, C. J.; Harvey, T. B.; Pernik, D. R.; Hibbert, J. I.; Du, J.; Rhee, D. J.; Akhavan, V. A.; Schaller, R. D.; Korgel, B. A. Multiexciton Solar Cells of $CuInSe_2$ Nanocrystals. *J. Phys. Chem. Lett.* **2014**, *5*, 304–309.

(18) Lin, H.; Irfan; Xia, W.; Wu, H. N.; Gao, Y.; Tang, C. W. MoOx Back Contact for CdS/CdTe Thin Film Solar Cells: Preparation, Device Characteristics, and Stability. *Sol. Energy Mater. Sol. Cells* **2012**, *99*, 349–355.

# References


Akhavan, V. A.; Panthani, M. G.; Goodfellow, B. W.; Reid, D. K.; Korgel, B. A. Thickness-Limited Performance of $CuInSe_2$ Nanocrystal Photovoltaic Devices. Opt. Express 2010, 18, A411.

Alivisatos, A. P. Semiconductor Clusters, Nanocrystals, and Quantum Dots. Science 1996, 271, 933–937.

Assadi, M. K.; Bakhoda, S.; Saidur, R.; Hanaei, H. Recent Progress in Perovskite Solar Cells. Renew. Sustain. Energy Rev.

Bae, S.; Kim, H.; Lee, Y.; Xu, X.; Park, J.-S.; Zheng, Y.; Balakrishnan, J.; Lei, T.; Ri Kim, H.; Song, Y. I.; et al. Roll-to-Roll Production of 30-Inch Graphene Films for Transparent Electrodes. Nat. Nanotechnol. 2010, 5, 574–578.

Barkhouse, D. A. R.; Pattantyus-Abraham, A. G.; Levina, L.; Sargent, E. H. Thiols Passivate Recombination Centers in Colloidal Quantum Dots Leading to Enhanced Photovoltaic Device Efficiency. ACS Nano 2008, 2, 2356–2362.

Barr, M. C.; Rowehl, J. A.; Lunt, R. R.; Xu, J.; Wang, A.; Boyce, C. M.; Im, S. G.; Bulović, V.; Gleason, K. K. Direct Monolithic Integration of Organic Photovoltaic Circuits on Unmodified Paper. Adv. Mater. 2011, 23, 3500–3505.

Becerril, H. A.; Mao, J.; Liu, Z.; Stoltenberg, R. M.; Bao, Z.; Chen, Y. Evaluation of Solution-Processed Reduced Graphene Oxide Films as Transparent Conductors. ACS Nano 2008, 2, 463–470.

Brabec, C. J. Organic Photovoltaics: Technology and Market. Sol. Energy Mater. Sol. Cells 2004, 83, 273–292.

Brabec, C. J.; Sariciftci, N. S.; Hummelen, J. C. Plastic Solar Cells. Adv. Funct. Mater. 2001, 11, 15–26.

Brown, R. M.; Willison, J. H.; Richardson, C. L. Cellulose Biosynthesis in Acetobacter Xylinum: Visualization of the Site of Synthesis and Direct Measurement of the in Vivo Process. Proc. Natl. Acad. Sci. U. S. A. 1976, 73, 4565–4569.

Chirilă, A.; Buecheler, S.; Pianezzi, F.; Bloesch, P.; Gretener, C.; Uhl, A. R.; Fella, C.; Kranz, L.; Perrenoud, J.; Seyrling, S.; et al. Highly Efficient Cu (In, Ga) $Se_2$ Solar Cells Grown on Flexible Polymer Films. Nature Mater. 2011, 10, 857–861.

Choi, J. J.; Lim, Y.-F.; Santiago-Berrios, M. B.; Oh, M.; Hyun, B.-R.; Sun, L.; Bartnik, A. C.; Goedhart, A.; Malliaras, G. G.; Abruña, H. D.; et al. PbSe Nanocrystal Excitonic Solar Cells. Nano Lett. 2009, 9, 3749–3755.

Choi, Y.-J.; Ahn, Y.; Kang, M.-S.; Jun, H.-K.; Kim, I. S.; Moon, S.-H. Preparation and Characterization of Acrylic Acid-Treated Bacterial Cellulose Cation-Exchange Membrane. J. Chem. Technol. Biotechnol. 2004, 79, 79–84.

Chuang, C.-H. M.; Brown, P. R.; Bulović, V.; Bawendi, M. G. Improved Performance and Stability in Quantum Dot Solar Cells through Band Alignment Engineering. Nat. Mater. 2014, 13, 796–801.

Comparing the levelized cost of energy technologies http://energyinnovation.org/2015/02/07/levelized-cost-of-energy/

Contreras, M. A.; Romero, M. J.; Noufi, R. Characterization of Cu(In,Ga)$Se_2$ Materials Used in Record Performance Solar Cells. Thin Solid Films 2006, 511, 51–54.

Cui, J.; Wang, A.; Edleman, N. L.; Ni, J.; Lee, P.; Armstrong, N. R.; Marks, T. J. Indium Tin Oxide Alternatives—High Work Function Transparent Conducting Oxides as Anodes for Organic Light-Emitting Diodes. Adv. Mater. 2001, 13, 1476–1480.

Czaja, W.; Krystynowicz, A.; Bielecki, S.; Brown Jr., R. M. Microbial Cellulose—the Natural Power to Heal Wounds. Biomaterials 2006, 27, 145–151.

Das, S.; Yang, B.; Gu, G.; Joshi, P. C.; Ivanov, I. N.; Rouleau, C. M.; Aytug, T.; Geohegan, D. B.; Xiao, K. High-Performance Flexible Perovskite Solar Cells by Using a Combination of Ultrasonic Spray-Coating and Low Thermal Budget Photonic Curing. ACS Photonics 2015, 2, 680–686.

De, S.; Higgins, T. M.; Lyons, P. E.; Doherty, E. M.; Nirmalraj, P. N.; Blau, W. J.; Boland, J. J.; Coleman, J. N. Silver Nanowire Networks as Flexible, Transparent, Conducting Films: Extremely High DC to Optical Conductivity Ratios. ACS Nano 2009, 3, 1767–1774.

Dementyev, A.; Hodges, S.; Taylor, S.; Smith, J. Power Consumption Analysis of Bluetooth Low Energy, ZigBee and ANT Sensor Nodes in a Cyclic Sleep Scenario. In 2013 IEEE International Wireless Symposium (IWS); 2013; pp. 1–4.

Dubey, V.; Pandey, L. K.; Saxena, C. Pervaporative Separation of Ethanol/water Azeotrope Using a Novel Chitosan-Impregnated Bacterial Cellulose Membrane and Chitosan–poly(vinyl Alcohol) Blends. J. Membr. Sci. 2005, 251, 131–136.

Dubey, V.; Saxena, C.; Singh, L.; Ramana, K. V.; Chauhan, R. S. Pervaporation of Binary Water–ethanol Mixtures through Bacterial Cellulose Membrane. Sep. Purif. Technol. 2002, 27, 163–171.

Eder, F.; Klauk, H.; Halik, M.; Zschieschang, U.; Schmid, G.; Dehm, C. Organic Electronics on Paper. Appl. Phys. Lett. 2004, 84, 2673–2675.

Evans, C. M.; Evans, M. E.; Krauss, T. D. Mysteries of TOPSe Revealed: Insights into Quantum Dot Nucleation. J. Am. Chem. Soc. 2010, 132, 10973–10975.

Fafarman, A. T.; Koh, W.; Diroll, B. T.; Kim, D. K.; Ko, D.-K.; Oh, S. J.; Ye, X.; Doan-Nguyen, V.; Crump, M. R.; Reifsnyder, D. C.; et al. Thiocyanate-Capped Nanocrystal Colloids: Vibrational Reporter of Surface Chemistry and Solution-Based Route to Enhanced Coupling in Nanocrystal Solids. J. Am. Chem. Soc. 2011, 133, 15753–15761.

Fatemi, N. S.; Pollard, H. E.; Hou, H. Q.; Sharps, P. R. Solar Array Trades between Very High-Efficiency Multi-Junction and Si Space Solar Cells. In Conference Record of the Twenty-Eighth IEEE Photovoltaic Specialists Conference, 2000; pp. 1083–1086.

Fontana, J. D.; De Souza, A. M.; Fontana, C. K.; Torriani, I. L.; Moreschi, J. C.; Gallotti, B. J.; De Souza, S. J.; Narcisco, G. P.; Bichara, J. A.; Farah, L. F. X. Acetobacter Cellulose Pellicle as a Temporary Skin Substitute. Appl. Biochem. Biotechnol. 1990, 24, 253–264.

Gartner Says 8.4 Billion Connected “Things” Will Be in Use in 2017, Up 31 Percent From 2016 http://www.gartner.com/newsroom/id/3598917

Gaynor, W.; Burkhard, G. F.; McGehee, M. D.; Peumans, P. Smooth Nanowire/Polymer Composite Transparent Electrodes. Adv. Mater. 2011, 23, 2905–2910.

Gomez, C.; Oller, J.; Paradells, J. Overview and Evaluation of Bluetooth Low Energy: An Emerging Low-Power Wireless Technology. Sensors 2012, 12, 11734–11753.

Gonzalez-Pedro, V.; Juarez-Perez, E. J.; Arsyad, W.-S.; Barea, E. M.; Fabregat-Santiago, F.; Mora-Sero, I.; Bisquert, J. General Working Principles of CH3NH3PbX3 Perovskite Solar Cells. Nano Lett. 2014, 14, 888–893.

Grau, G.; Kitsomboonloha, R.; Swisher, S. L.; Kang, H.; Subramanian, V. Printed Transistors on Paper: Towards Smart Consumer Product Packaging. Adv. Funct. Mater. 2014, 24, 5067–5074.

Green, M. A.; Ho-Baillie, A.; Snaith, H. J. The Emergence of Perovskite Solar Cells. Nat. Photonics 2014, 8, 506–514.

Gregg, A.; Blieden, R.; Chang, A.; Ng, H. Performance Analysis of Large Scale, Amorphous Silicon, Photovoltaic Power Systems. In Conference Record of the Thirty-first IEEE Photovoltaic Specialists Conference, 2005.; 2005; pp. 1615–1618.

Guo, Q.; Ford, G. M.; Yang, W.-C.; Walker, B. C.; Stach, E. A.; Hillhouse, H. W.; Agrawal, R. Fabrication of 7.2% Efficient CZTSSe Solar Cells Using CZTS Nanocrystals. J. Am. Chem. Soc. 2010, 132, 17384–17386.

Guo, Q.; Hillhouse, H. W.; Agrawal, R. Synthesis of $Cu_2ZnSnS_4$ Nanocrystal Ink and Its Use for Solar Cells. J. Am. Chem. Soc. 2009, 131, 11672–11673.

Guo, Q.; Kim, S. J.; Kar, M.; Shafarman, W. N.; Birkmire, R. W.; Stach, E. A.; Agrawal, R.; Hillhouse, H. W. Development of $CuInSe_2$ Nanocrystal and Nanoring Inks for Low-Cost Solar Cells. Nano Lett. 2008, 8, 2982–2987.

Gur, I.; Fromer, N. A.; Geier, M. L.; Alivisatos, A. P. Air-Stable All-Inorganic Nanocrystal Solar Cells Processed from Solution. Science 2005, 310, 462–465.

Guyot-Sionnest, P.; Wang, C. Fast Voltammetric and Electrochromic Response of Semiconductor Nanocrystal Thin Films. J. Phys. Chem. B 2003, 107, 7355–7359.

Hagfeldt, A.; Boschloo, G.; Sun, L.; Kloo, L.; Pettersson, H. Dye-Sensitized Solar Cells. Chem. Rev. 2010, 110, 6595–6663.

Haigler, C. H.; White, A. R.; Brown, R. M.; Cooper, K. M. Alteration of in Vivo Cellulose Ribbon Assembly by Carboxymethylcellulose and Other Cellulose Derivatives. J. Cell Biol. 1982, 94, 64–69.

Harvey, T. B.; Mori, I.; Stolle, C. J.; Bogart, T. D.; Ostrowski, D. P.; Glaz, M. S.; Du, J.; Pernik, D. R.; Akhavan, V. A.; Kesrouani, H.; et al. Copper Indium Gallium Selenide (CIGS) Photovoltaic Devices Made Using Multistep Selenization of Nanocrystal Films. ACS Appl. Mater. Interfaces 2013, 5, 9134–9140.

Hau, S. K.; Yip, H.-L.; Zou, J.; Jen, A. K.-Y. Indium Tin Oxide-Free Semi-Transparent Inverted Polymer Solar Cells Using Conducting Polymer as Both Bottom and Top Electrodes. Org. Electron. 2009, 10, 1401–1407.

Haug, F.-J.; Ballif, C. Light Management in Thin Film Silicon Solar Cells. Energy Environ. Sci. 2015, 8, 824–837.

Henry, C. H. Limiting Efficiencies of Ideal Single and Multiple Energy Gap Terrestrial Solar Cells. J. Appl. Phys. 1980, 51, 4494–4500.

Hens, Z.; Martins, J. C. A Solution NMR Toolbox for Characterizing the Surface Chemistry of Colloidal Nanocrystals. Chem. Mater. 2013, 25, 1211–1221.

Hens, Z.; Moreels, I.; Martins, J. C. In Situ 1H NMR Study on the Trioctylphosphine Oxide Capping of Colloidal InP Nanocrystals. ChemPhysChem 2005, 6, 2578–2584.

Herrmann, D.; Kessler, F.; Herz, K.; Powalla, M.; Schulz, A.; Schneider, J.; Schumacher, U. High-Performance Barrier Layers for Flexible CIGS Thin-Film Solar Cells on Metal Foils. MRS Proceedings; Cambridge Univ Press, 2003; Vol. 763, pp. B6–B10.

Hesse, S.; Kondo, T. Behavior of Cellulose Production of Acetobacter Xylinum in 13 C-Enriched Cultivation Media Including Movements on Nematic Ordered Cellulose Templates. Carbohydr. Polym. 2005, 60, 457–465.

Hillhouse, H. W.; Beard, M. C. Solar Cells from Colloidal Nanocrystals: Fundamentals, Materials, Devices, and Economics. Curr. Opin. Colloid Interface Sci. 2009, 14, 245–259.

Hoth, C. N.; Schilinsky, P.; Choulis, S. A.; Brabec, C. J. Printing Highly Efficient Organic Solar Cells. Nano Lett. 2008, 8, 2806–2813.

Hübler, A.; Trnovec, B.; Zillger, T.; Ali, M.; Wetzold, N.; Mingebach, M.; Wagenpfahl, A.; Deibel, C.; Dyakonov, V. Printed Paper Photovoltaic Cells. Adv. Energy Mater. 2011, 1, 1018–1022.

Iguchi, M.; Yamanaka, S.; Budhiono, A. Bacterial Cellulose—a Masterpiece of Nature's Arts. J. Mater. Sci. 2000, 35, 261–270.

Jackson, P.; Hariskos, D.; Lotter, E.; Paetel, S.; Wuerz, R.; Menner, R.; Wischmann, W.; Powalla, M. New World Record Efficiency for Cu(In,Ga)$Se_2$ Thin-Film Solar Cells beyond 20%. Prog. Photovolt. Res. Appl. 2011, 19, 894–897.

Janssen, R. A. J.; Hummelen, J. C.; Sariciftci, N. S. Polymer–Fullerene Bulk Heterojunction Solar Cells. MRS Bull. 2005, 30, 33–36.

Jo, J. W.; Kim, Y.; Choi, J.; de Arquer, F. P. G.; Walters, G.; Sun, B.; Ouellette, O.; Kim, J.; Proppe, A. H.; Quintero-Bermudez, R.; et al. Enhanced Open-Circuit Voltage in Colloidal Quantum Dot Photovoltaics via Reactivity-Controlled Solution-Phase Ligand Exchange. Adv. Mater.1703627.

Kaltenbrunner, M.; White, M. S.; G lowacki, E. D.; Sekitani, T.; Someya, T.; Sariciftci, N. S.; Bauer, S. Ultrathin and Lightweight Organic Solar Cells with High Flexibility. Nat. Commun. 2012, 3, 770.

Kamat, P. V. Quantum Dot Solar Cells. Semiconductor Nanocrystals as Light Harvesters. J. Phys. Chem. C 2008, 112, 18737–18753.

Kan, B.; Zhang, Q.; Li, M.; Wan, X.; Ni, W.; Long, G.; Wang, Y.; Yang, X.; Feng, H.; Chen, Y. Solution-Processed Organic Solar Cells Based on Dialkylthiol-Substituted Benzodithiophene Unit with Efficiency near 10%. J. Am. Chem. Soc. 2014, 136, 15529–15532.

Kapur, V. K.; Bansal, A.; Le, P.; Asensio, O. I. Non-Vacuum Processing of $CuIn_{1-x}Ga_xSe_2$ Solar Cells on Rigid and Flexible Substrates Using Nanoparticle Precursor Inks. Thin Solid Films 2003, 431, 53–57.

Kawano, K.; Pacios, R.; Poplavskyy, D.; Nelson, J.; Bradley, D. D. C.; Durrant, J. R. Degradation of Organic Solar Cells due to Air Exposure. Sol. Energy Mater. Sol. Cells 2006, 90, 3520–3530.

Kazim, S.; Nazeeruddin, M. K.; Grätzel, M.; Ahmad, S. Perovskite as Light Harvester: A Game Changer in Photovoltaics. Angew. Chem. Int. Ed. 2014, 53, 2812–2824.

Kessler, F.; Herz, K.; Powalla, M.; Hartmann, M.; Schmidt, M.; Jasenek, A.; Schock, H. W. Flexible and Monolithically Integrated CIGS-Modules. MRS Proceedings; Cambridge Univ Press, 2001; Vol. 668, pp. H3–H6.

Kessler, F.; Rudmann, D. Technological Aspects of Flexible CIGS Solar Cells and Modules. Sol. Energy 2004, 77, 685–695.

Kim, J. Y.; Lee, K.; Coates, N. E.; Moses, D.; Nguyen, T.-Q.; Dante, M.; Heeger, A. J. Efficient Tandem Polymer Solar Cells Fabricated by All-Solution Processing. Science 2007, 317, 222–225.

Kobayashi, T.; Yamaguchi, H.; Nakada, T. Effects of Combined Heat and Light Soaking on Device Performance of $Cu(In,Ga)Se_2$ Solar Cells with ZnS(O,OH) Buffer Layer. Prog. Photovolt. Res. Appl. 2014, 22, 115–121.

Kojima, A.; Teshima, K.; Shirai, Y.; Miyasaka, T. Organometal Halide Perovskites as Visible-Light Sensitizers for Photovoltaic Cells. J. Am. Chem. Soc. 2009, 131, 6050–6051.

Koleilat, G. I.; Levina, L.; Shukla, H.; Myrskog, S. H.; Hinds, S.; Pattantyus-Abraham, A. G.; Sargent, E. H. Efficient, Stable Infrared Photovoltaics Based on Solution-Cast Colloidal Quantum Dots. ACS Nano 2008, 2, 833–840.

Koo, B.; Patel, R. N.; Korgel, B. A. Synthesis of $CuInSe_2$ Nanocrystals with Trigonal Pyramidal Shape. J. Am. Chem. Soc. 2009, 131, 3134–3135.

Korala, L.; Braun, M. B.; Kephart, J. M.; Tregillus, Z.; Prieto, A. L. Ligand-Exchanged CZTS Nanocrystal Thin Films: Does Nanocrystal Surface Passivation Effectively Improve Photovoltaic Performance? Chem. Mater. 2017, 29, 6621–6629.

Krebs, F. C. All Solution Roll-to-Roll Processed Polymer Solar Cells Free from Indium-Tin-Oxide and Vacuum Coating Steps. Org. Electron. 2009, 10, 761–768.

Krebs, F. C. Fabrication and Processing of Polymer Solar Cells: A Review of Printing and Coating Techniques. Sol. Energy Mater. Sol. Cells 2009, 93, 394–412.

Kumar, A.; Zhou, C. The Race to Replace Tin-Doped Indium Oxide: Which Material Will Win? ACS Nano 2010, 4, 11–14.

Lan, X.; Voznyy, O.; García de Arquer, F. P.; Liu, M.; Xu, J.; Proppe, A. H.; Walters, G.; Fan, F.; Tan, H.; Liu, M.; et al. 10.6% Certified Colloidal Quantum Dot Solar Cells via Solvent-Polarity-Engineered Halide Passivation. Nano Lett. 2016, 16, 4630–4634.

Lee, J.-Y.; Connor, S. T.; Cui, Y.; Peumans, P. Solution-Processed Metal Nanowire Mesh Transparent Electrodes. Nano Lett. 2008, 8, 689–692.

Legnani, C.; Vilani, C.; Calil, V. L.; Barud, H. S.; Quirino, W. G.; Achete, C. A.; Ribeiro, S. J. L.; Cremona, M. Bacterial Cellulose Membrane as Flexible Substrate for Organic Light Emitting Devices. Thin Solid Films 2008, 517, 1016–1020.

Leonat, L.; White, M. S.; Głowacki, E. D.; Scharber, M. C.; Zillger, T.; Rühling, J.; Hübler, A.; Sariciftci, N. S. 4% Efficient Polymer Solar Cells on Paper Substrates. J. Phys. Chem. C 2014, 118, 16813–16817.

Li, X.; Zhu, Y.; Cai, W.; Borysiak, M.; Han, B.; Chen, D.; Piner, R. D.; Colombo, L.; Ruoff, R. S. Transfer of Large-Area Graphene Films for High-Performance Transparent Conductive Electrodes. Nano Lett. 2009, 9, 4359–4363.

Lim, W.; Douglas, E. A.; Kim, S.-H.; Norton, D. P.; Pearton, S. J.; Ren, F.; Shen, H.; Chang, W. H. High Mobility $InGaZnO_4$ Thin-Film Transistors on Paper. Appl. Phys. Lett. 2009, 94, 072103.

Lin, H.; Irfan; Xia, W.; Wu, H. N.; Gao, Y.; Tang, C. W. MoOx Back Contact for CdS/CdTe Thin Film Solar Cells: Preparation, Device Characteristics, and Stability. Sol. Energy Mater. Sol. Cells 2012, 99, 349–355.

Lin, Q.; Huang, H.; Jing, Y.; Fu, H.; Chang, P.; Li, D.; Yao, Y.; Fan, Z. Flexible Photovoltaic Technologies. J. Mater. Chem. C 2014, 2, 1233.

Ma, W.; Luther, J. M.; Zheng, H.; Wu, Y.; Alivisatos, A. P. Photovoltaic Devices Employing Ternary $PbS_xSe_{1-x}$ Nanocrystals. Nano Lett. 2009, 9, 1699–1703.

Manceau, M.; Bundgaard, E.; E. Carlé, J.; Hagemann, O.; Helgesen, M.; Søndergaard, R.; Jørgensen, M.; C. Krebs, F. Photochemical Stability of π- Conjugated Polymers for Polymer Solar Cells: A Rule of Thumb. J. Mater. Chem. 2011, 21, 4132–4141.

Martinez, A. W.; Phillips, S. T.; Whitesides, G. M.; Carrilho, E. Diagnostics for the Developing World: Microfluidic Paper-Based Analytical Devices. Anal. Chem. 2010, 82, 3–10.

Mazzeo, A. D.; Kalb, W. B.; Chan, L.; Killian, M. G.; Bloch, J.-F.; Mazzeo, B. A.; Whitesides, G. M. Paper-Based, Capacitive Touch Pads. Adv. Mater. 2012, 24, 2850–2856.

McCandless, B. E.; Shafarman, W. N. Chemical Surface Deposition of Ultra-Thin Semiconductors. US6537845 B1, March 25, 2003.

McDonald, S. A.; Konstantatos, G.; Zhang, S.; Cyr, P. W.; Klem, E. J. D.; Levina, L.; Sargent, E. H. Solution-Processed PbS Quantum Dot Infrared Photodetectors and Photovoltaics. Nat. Mater. 2005, 4, 138–142.

Miodownik, M. Stuff Matters: Exploring the Marvelous Materials That Shape Our Manmade World; Houghton Mifflin Harcourt, New York, U.S.; 2014.

Nag, A.; Kovalenko, M. V.; Lee, J.-S.; Liu, W.; Spokoyny, B.; Talapin, D. V. Metal-Free Inorganic Ligands for Colloidal Nanocrystals: $S^{2-}$, $HS^-$, $Se^{2-}$, $HSe^-$, $Te^{2-}$, $HTe^-$, $TeS_3^{2-}$, $OH^-$, and $NH_2^-$ as Surface Ligands. J. Am. Chem. Soc. 2011, 133, 10612–10620.

Nakada, T.; Furumi, K.; Kunioka, A. High-Efficiency Cadmium-Free Cu(In,Ga)Se2 Thin-Film Solar Cells with Chemically Deposited ZnS Buffer Layers. IEEE Trans. Electron Devices 1999, 46, 2093–2097.

Nelson, J. The Physics of Solar Cells; World Scientific Publishing Company, 2003.

Niggemann, M.; Glatthaar, M.; Gombert, A.; Hinsch, A.; Wittwer, V. Diffraction Gratings and Buried Nano-Electrodes—architectures for Organic Solar Cells. Thin Solid Films 2004, 451–452, 619–623.

Nirmal, M.; Brus, L. Luminescence Photophysics in Semiconductor Nanocrystals. Acc. Chem. Res. 1999, 32, 407–414.

Nishi, Y.; Uryu, M.; Yamanaka, S.; Watanabe, K.; Kitamura, N.; Iguchi, M.; Mitsuhashi, S. The Structure and Mechanical Properties of Sheets Prepared from Bacterial Cellulose. J. Mater. Sci. 1990, 25, 2997–3001.

Nishi, Y.; Uryu, M.; Yamanaka, S.; Watanabe, K.; Kitamura, N.; Iguchi, M.; Mitsuhashi, S. The Structure and Mechanical Properties of Sheets Prepared from Bacterial Cellulose. J. Mater. Sci. 1990, 25, 2997–3001.

Niu, G.; Guo, X.; Wang, L. Review of Recent Progress in Chemical Stability of Perovskite Solar Cells. J. Mater. Chem. A 2015, 3, 8970–8980.

Pagliaro, M.; Ciriminna, R.; Palmisano, G. Flexible Solar Cells. ChemSusChem 2008, 1, 880–891.

Panthani, M. G.; Akhavan, V.; Goodfellow, B.; Schmidtke, J. P.; Dunn, L.; Dodabalapur, A.; Barbara, P. F.; Korgel, B. A. Synthesis of $CuInS_2$, $CuInSe_2$, and $Cu(In_xGa_{1-x})Se_2$ (CIGS) Nanocrystal "Inks" for Printable Photovoltaics. J. Am. Chem. Soc. 2008, 130, 16770–16777.

Panthani, M. G.; Kurley, J. M.; Crisp, R. W.; Dietz, T. C.; Ezzyat, T.; Luther, J. M.; Talapin, D. V. High Efficiency Solution Processed Sintered CdTe Nanocrystal Solar Cells: The Role of Interfaces. Nano Lett. 2014, 14, 670–675.

Panthani, M. G.; Stolle, C. J.; Reid, D. K.; Rhee, D. J.; Harvey, T. B.; Akhavan, V. A.; Yu, Y.; Korgel, B. A. $CuInSe_2$ Quantum Dot Solar Cells with High Open-Circuit Voltage. J. Phys. Chem. Lett. 2013, 4, 2030–2034.

Pattantyus-Abraham, A. G.; Kramer, I. J.; Barkhouse, A. R.; Wang, X.; Konstantatos, G.; Debnath, R.; Levina, L.; Raabe, I.; Nazeeruddin, M. K.; Grätzel, M.; et al. Depleted-Heterojunction Colloidal Quantum Dot Solar Cells. ACS Nano 2010, 4, 3374–3380.

Pernik, D. R.; Gutierrez, M.; Thomas, C.; Voggu, V. R.; Yu, Y.; van Embden, J.; Topping, A. J.; Jasieniak, J. J.; Vanden Bout, D. A.; Lewandowski, R.; et al. Plastic Microgroove Solar Cells Using $CuInSe_2$ Nanocrystals. ACS Energy Lett. 2016, 1, 1021–1027.

Poplawsky, J. D. Cadmium Telluride Solar Cells: Record-Breaking Voltages. Nat. Energy 2016, 1, nenergy201621.

Rathmell, A. R.; Wiley, B. J. The Synthesis and Coating of Long, Thin Copper Nanowires to Make Flexible, Transparent Conducting Films on Plastic Substrates. Adv. Mater. 2011, 23, 4798–4803.

Rau, U.; Braunger, D.; Herberholz, R; Schock, H. W.; Guillemoles, J. F., Kronik, L., & Cahen, D. Oxygenation and air-annealing effects on the electronic properties of Cu(In,Ga)$Se_2$ films and devices. Journal of Applied Physics, 1999, 86(1), 497-505.

Reinhard, P.; Chirila, A.; Blosch, P.; Pianezzi, F.; Nishiwaki, S.; Buechelers, S.; Tiwari, A. N. Review of Progress toward 20% Efficiency Flexible CIGS Solar Cells and Manufacturing Issues of Solar Modules. Photovolt. IEEE J. 2013, 3, 572–580.

Repins, I.; Contreras, M. A.; Egaas, B.; DeHart, C.; Scharf, J.; Perkins, C. L.; To, B.; Noufi, R. 19·9%-Efficient ZnO/CdS/$CuInGaSe_2$ Solar Cell with 81·2% Fill Factor. Prog. Photovolt. Res. Appl. 2008, 16, 235–239.

Rowell, M. W.; Topinka, M. A.; McGehee, M. D.; Prall, H.-J.; Dennler, G.; Sariciftci, N. S.; Hu, L.; Gruner, G. Organic Solar Cells with Carbon Nanotube Network Electrodes. Appl. Phys. Lett. 2006, 88, 233506.

Sarasqueta, G.; Choudhury, K. R.; So, F. Effect of Solvent Treatment on Solution-Processed Colloidal PbSe Nanocrystal Infrared Photodetectors. Chem. Mater. 2010, 22, 3496–3501.

Sarasqueta, G.; Choudhury, K. R.; So, F. Effect of Solvent Treatment on Solution-Processed Colloidal PbSe Nanocrystal Infrared Photodetectors. Chem. Mater. 2010, 22, 3496–3501.

Schaller, R. D. High Efficiency Carrier Multiplication in PbSe Nanocrystals: Implications for Solar Energy Conversion. Phys. Rev. Lett. 2004, 92.

Seshan, C. Cell Efficiency Dependence on Solar Incidence Angle. In 2010 35th IEEE Photovoltaic Specialists Conference (PVSC); 2010; pp. 002102–002105.

Shah, A. V.; Platz, R.; Keppner, H. Thin-Film Silicon Solar Cells: A Review and Selected Trends. Sol. Energy Mater. Sol. Cells 1995, 38, 501–520.

Shah, J.; Jr, R. M. B. Towards Electronic Paper Displays Made from Microbial Cellulose. Appl. Microbiol. Biotechnol. 2004, 66, 352–355.

Shaheen, S. E.; Brabec, C. J.; Sariciftci, N. S.; Padinger, F.; Fromherz, T.; Hummelen, J. C. 2.5% Efficient Organic Plastic Solar Cells. Appl. Phys. Lett. 2001, 78, 841–843.

Shibazaki, H.; Kuga, S.; Onabe, F.; Usuda, M. Bacterial Cellulose Membrane as Separation Medium. J. Appl. Polym. Sci. 1993, 50, 965–969.

Solar Cell Market Size, Share | Industry Report, 2022 http://www.grandviewresearch.com/industry-analysis/solar-cell-market.

Solar Energy vs Fossil Fuels: How Do They Compare? | EnergySage http://news.energysage.com/solar-energy-vs-fossil-fuels/

Speliotis, D. Magnetic Recording beyond the First 100 Years. J. Magn. Magn. Mater. 1999, 193, 29–35.

Stolle, C. J.; Harvey, T. B.; Pernik, D. R.; Hibbert, J. I.; Du, J.; Rhee, D. J.; Akhavan, V. A.; Schaller, R. D.; Korgel, B. A. Multiexciton Solar Cells of $CuInSe_2$ Nanocrystals. J. Phys. Chem. Lett. 2014, 5, 304–309.

Stolle, C. J.; Panthani, M. G.; Harvey, T. B.; Akhavan, V. A.; Korgel, B. A. Comparison of the Photovoltaic Response of Oleylamine and Inorganic Ligand-Capped $CuInSe_2$ Nanocrystals. ACS Appl. Mater. Interfaces 2012, 4, 2757–2761.

Sun, S.; Murray, C. B.; Weller, D.; Folks, L.; Moser, A. Monodisperse FePt Nanoparticles and Ferromagnetic FePt Nanocrystal Superlattices. Science 2000, 287, 1989–1992.

Sun, S.; Salim, T.; Mathews, N.; Duchamp, M.; Boothroyd, C.; Xing, G.; Chien Sum, T.; Ming Lam, Y. The Origin of High Efficiency in Low-Temperature Solution-Processable Bilayer Organometal Halide Hybrid Solar Cells. Energy Environ. Sci. 2014, 7, 399–407.

Systems, eZ. nRF51822 / Bluetooth low energy / Products / Home - Ultra Low Power Wireless Solutions from NORDIC SEMICONDUCTOR https://www.nordicsemi.com/eng/Products/Bluetooth-low-energy/nRF51822

Talgorn, E.; Moysidou, E.; Abellon, R. D.; Savenije, T. J.; Goossens, A.; Houtepen, A. J.; Siebbeles, L. D. A. Highly Photoconductive CdSe Quantum-Dot Films: Influence of Capping Molecules and Film Preparation Procedure. J. Phys. Chem. C 2010, 114, 3441–3447.

Tang, J.; Hinds, S.; Kelley, S. O.; Sargent, E. H. Synthesis of Colloidal CuGaSe2, CuInSe2, and $Cu(InGa)Se_2$ Nanoparticles. Chem. Mater. 2008, 20, 6906–6910.

Tang, J.; Kemp, K. W.; Hoogland, S.; Jeong, K. S.; Liu, H.; Levina, L.; Furukawa, M.; Wang, X.; Debnath, R.; Cha, D.; et al. Colloidal-Quantum-Dot Photovoltaics Using Atomic-Ligand Passivation. Nat. Mater. 2011, 10, 765–771.

Tang, J.; Kemp, K. W.; Hoogland, S.; Jeong, K. S.; Liu, H.; Levina, L.; Furukawa, M.; Wang, X.; Debnath, R.; Cha, D.; et al. Colloidal-Quantum-Dot Photovoltaics Using Atomic-Ligand Passivation. Nat. Mater. 2011, 10, 765–771.

Tang, R.; Huang, H.; Tu, H.; Liang, H.; Liang, M.; Song, Z.; Xu, Y.; Jiang, H.; Yu, H. Origami-Enabled Deformable Silicon Solar Cells. Appl. Phys. Lett. 2014, 104, 083501.

Tian, Q.; Xu, X.; Han, L.; Tang, M.; Zou, R.; Chen, Z.; Yu, M.; Yang, J.; Hu, J. Hydrophilic $Cu_2ZnSnS_4$ Nanocrystals for Printing Flexible, Low-Cost and Environmentally Friendly Solar Cells. CrystEngComm 2012, 14, 3847–3850.

Tvingstedt, K.; Andersson, V.; Zhang, F.; Inganäs, O. Folded Reflective Tandem Polymer Solar Cell Doubles Efficiency. Appl. Phys. Lett. 2007, 91, 123514.

Ummartyotin, S.; Juntaro, J.; Sain, M.; Manuspiya, H. Development of Transparent Bacterial Cellulose Nanocomposite Film as Substrate for Flexible Organic Light Emitting Diode (OLED) Display. Ind. Crops Prod. 2012, 35, 92–97.

Ververis, C.; Georghiou, K.; Christodoulakis, N.; Santas, P.; Santas, R. Fiber Dimensions, Lignin and Cellulose Content of Various Plant Materials and Their Suitability for Paper Production. Ind. Crops Prod. 2004, 19, 245–254.

Voggu, V. R.; Sham, J.; Pfeffer, S.; Pate, J.; Fillip, L.; Harvey, T. B.; Brown, R. M.; Korgel, B. A. Flexible $CuInSe_2$ Nanocrystal Solar Cells on Paper. ACS Energy Lett. 2017, 2, 574–581.

Vosgueritchian, M.; Lipomi, D. J.; Bao, Z. Highly Conductive and Transparent PEDOT:PSS Films with a Fluorosurfactant for Stretchable and Flexible Transparent Electrodes. Adv. Funct. Mater. 2012, 22, 421–428.

Wang, B.; Kerr, L. L. Dye Sensitized Solar Cells on Paper Substrates. Sol. Energy Mater. Sol. Cells 2011, 95, 2531–2535.

Wu, H.; Hu, L.; Rowell, M. W.; Kong, D.; Cha, J. J.; McDonough, J. R.; Zhu, J.; Yang, Y.; McGehee, M. D.; Cui, Y. Electrospun Metal Nanofiber Webs as High-Performance Transparent Electrode. Nano Lett. 2010, 10, 4242–4248.

Yano, H.; Sugiyama, J.; Nakagaito, A. N.; Nogi, M.; Matsuura, T.; Hikita, M.; Handa, K. Optically Transparent Composites Reinforced with Networks of Bacterial Nanofibers. Adv. Mater. 2005, 17, 153–155.

Yoon, B.; Ham, D.-Y.; Yarimaga, O.; An, H.; Lee, C. W.; Kim, J.-M. Inkjet Printing of Conjugated Polymer Precursors on Paper Substrates for Colorimetric Sensing and Flexible Electrothermochromic Display. Adv. Mater. 2011, 23, 5492–5497.

Yoon, W.; Boercker, J. E.; Lumb, M. P.; Placencia, D.; Foos, E. E.; Tischler, J. G. Enhanced Open-Circuit Voltage of PbS Nanocrystal Quantum Dot Solar Cells. Sci. Rep. 2013, 3, srep02225.

Yoshino, K.; Matsuoka, R.; Nogami, K.; Yamanaka, S.; Watanabe, K.; Takahashi, M.; Honma, M. Graphite Film Prepared by Pyrolysis of Bacterial Cellulose. J. Appl. Phys. 1990, 68, 1720–1725.

Yu, Y.; Bosoy, C. A.; Hessel, C. M.; Smilgies, D.-M.; Korgel, B. A. Silicon Nanocrystal Superlattices. ChemPhysChem 2013, 14, 84–87.

Yu, Y.; Bosoy, C. A.; Smilgies, D.-M.; Korgel, B. A. Self-Assembly and Thermal Stability of Binary Superlattices of Gold and Silicon Nanocrystals. J. Phys. Chem. Lett. 2013, 4, 3677–3682.

Zhang, C.; Song, Y.; Wang, M.; Yin, M.; Zhu, X.; Tian, L.; Wang, H.; Chen, X.; Fan, Z.; Lu, L.; et al. Solar Cells: Efficient and Flexible Thin Film Amorphous Silicon Solar Cells on Nanotextured Polymer Substrate Using Sol–gel Based Nanoimprinting Method (Adv. Funct. Mater. 13/2017). Adv. Funct. Mater. 2017, 27.

Zhang, L.; Xia, Y. Scaling up the Production of Colloidal Nanocrystals: Should We Increase or Decrease the Reaction Volume? Adv. Mater. 2014, 26, 2600–2606.

Zhao, N.; Osedach, T. P.; Chang, L.-Y.; Geyer, S. M.; Wanger, D.; Binda, M. T.; Arango, A. C.; Bawendi, M. G.; Bulovic, V. Colloidal PbS Quantum Dot Solar Cells with High Fill Factor. ACS Nano 2010, 4, 3743–3752.

Zhong, H.; Wang, Z.; Bovero, E.; Lu, Z.; van Veggel, F. C. J. M.; Scholes, G. D. Colloidal CuInSe2 Nanocrystals in the Quantum Confinement Regime: Synthesis, Optical Properties, and Electroluminescence. J. Phys. Chem. C 2011, 115, 12396–12402.

Zhou, Y.; Zhang, F.; Tvingstedt, K.; Tian, W.; Inganäs, O. Multifolded Polymer Solar Cells on Flexible Substrates. Appl. Phys. Lett. 2008, 93, 033302.

# Vita

Vikas Reddy Voggu was born in Andhra Pradesh, India to Prabhakar Reddy Voggu and Malleswari Voggu. He earned a Bachelor of Technology in Chemical Engineering from Indian Institute of Technology, Roorkee in 2013. He then went on to attend The University of Texas at Austin in the fall of 2013. He earned a Master of Science in Engineering in spring of 2017 and completed his Ph.D. in Chemical Engineering in the fall of 2017 from UT Austin. He performed his graduate studies developing inexpensive solar cells under the supervision of Dr. Brian Korgel. Vikas will work as a process engineer at Intel Corporation, starting from the spring of 2018.

The author can be reached at vikasreddy@utexas.edu

This dissertation was typed by the author.